



universität
wien

MASTERARBEIT

Titel

**Setup of an optical time-domain matter wave interferometer
for heavy particles**

von

BSc Jonas Rodewald

angestrebter akademischer Grad

Master of Science (MSc)

Wien, September 2011

Studienkennzahl lt. Studienblatt:	A 066 876
Matrikelnummer:	0946081
Studienrichtung lt. Studienblatt:	Masterstudium Physik UG2002
Betreuer:	Prof. Dr. Markus Arndt

Contents

1	Abstract	2
2	Zusammenfassung	4
3	Introduction	6
4	Review of Talbot-Lau Interferometry	7
4.1	History of the Talbot-Lau effect	7
4.2	The Talbot-Lau Interferometer as a tool for matter wave optics	8
4.3	OTIMA-interference scheme	12
5	Theoretical treatment	15
5.1	Physics of metal clusters	15
5.1.1	Photon absorption cross sections of small metal clusters	16
5.1.2	Polarizability of small metal clusters	19
5.2	Evolution of quantum states in the OTIMA-TLI	20
5.3	Aligning requirements	26
5.4	Theory of the laser gratings	28
5.5	Interference contrast	30
5.6	Classical contrast	31
5.7	Expected visibilities for an OTIMA-interference experiment . .	32
5.8	Comparison to the conventional TLI	39
6	Experimental setup	40
6.1	Setup overview	40
6.2	Source setup	46
6.2.1	Source settings	48
6.2.2	Particle beam characteristics	49
6.3	Velocity selection	53
6.4	TOF mass spectrometer	57
6.5	VUV-Laser System	58
6.6	Beam guiding	61
6.7	Interferometer mirror	62

CONTENTS

6.8	Measurement of the longitudinal coherence length	66
6.9	Interferometer alignment	69
6.10	Jitter monitoring	71
6.11	Relevance of vibrations	73
6.12	Relevance of inertial forces	77
6.13	Particle considerations	81
6.14	Mass spectra	82
7	Outlook	86
7.1	Selection criteria for an alternative laser system	86
7.2	Towards interferometry	88
7.3	Buffer gas cooling stage	89
7.4	The Even-Lavie valve as a source for the OTIMA-TLI	94
8	Acknowledgments	109
9	Curriculum Vitae	110

1 Abstract

In this thesis the setup of an optical time-domain ionizing matter wave Talbot-Lau interferometer (OTIMA-TLI) is discussed. The experiment aims at demonstrating the quantum wave nature of increasingly heavy particles. The mass limit of the current version lies around 25.000 amu which is more than three times higher than the present-day mass record for matter wave interferometry. In order to be especially suited for this purpose the OTIMA-TLI is equipped, for the first time, with pulsed ionizing absorptive laser gratings with a grating period of 78,6 nm. Such gratings are perfectly periodic and come without dispersive grating-particle interactions thus promising high contrast interference even for massive and slow particles. Working with pulsed gratings additionally allows for greater velocity spread within the particle beam which promises higher count rates at high particle masses. The techniques and methods we have developed will in future enable the implementation of matter wave interferometers with a mass limit exceeding 10^6 amu.

The experiment is currently in the build-up phase and this work documents the design and experimental realization both in theory and in practice.

2 Zusammenfassung

In dieser Arbeit werden Planung und Aufbau eines neuen Materiewellen Talbot-Lau Interferometers dokumentiert. Das Experiment soll in Zukunft den quantenmechanischen Wellencharakter von zunehmend schwereren Teilchen nachweisen, wobei die Massengrenze für den Aufbau bei ca. 25.000 amu liegt. Dies übersteigt den derzeitigen Massenrekord für Materiewellen Interferometrie um mehr als das Dreifache. Um dieser Herausforderung gerecht zu werden ist das Interferometer erstmals mit gepulsten absorptiven Ionisationslasergittern ausgerüstet, welche gegenüber materiellen Gittern den Vorteil nahezu perfekter Periodizität aufweisen bei einer bisher bei Molekülinterferometern unerreicht kleinen Gitterkonstante von 78,6 nm. Außerdem treten bei Lasergittern keine dispersiven Wechselwirkungen zwischen Teilchen und Gittern auf, von denen bekannt ist, daß sie den maximal möglichen Interferenzkontrast in Talbot-Lau Interferometern für große Massen drastisch reduzieren. Das neue Interferometer verspricht somit hohen Interferenzkontrast auch für schwere und langsame Teilchen, wobei Pulsen des Experiments breite Geschwindigkeitsverteilungen im Teilchenstrahl zuläßt und damit hohe Zählraten für große Teilchenmassen verspricht.

Es ist hervorzuheben, daß die Technik, welche für die Lasergitter entwickelt wurde, in Zukunft den Aufbau von Interferometern ermöglicht mit Massengrenzen sogar jenseits von 10^6 amu.

3 Introduction

In the past century quantum mechanics has developed from a revolutionary concept to one of the most precisely studied theories in physics. This might imply that a majority of questions has been answered over the years. Yet, exactly the opposite is the case: it seems that many questions that once puzzled the founders of quantum mechanics are still open for dispute today. An example is the famous paradox formulated by Erwin Schrödinger in 1935 [1]. In this *gedanken experiment* a cat's life is entangled with the decay process of a radioactive atom. In analogy to the atom being in a superposition of decayed and not-decayed the animal is thus in a superposition state of death and life. Schrödinger used this to express his discomfort with accepting the fundamental imprecision which Heisenberg's uncertainty relation assigns to every measurement as a true picture of reality. The most common notion today is that the state of the cat is constantly probed by interaction with the environment since a macroscopic system, such as a cat, is never sufficiently isolated from its surrounding. This, however, implies that every object, regardless of its mass or complexity, would exhibit quantum mechanical behavior if it were only decoupled from external influences. Whether this is true has remained an unanswered question to date. Yet, today the question whether quantum mechanics is valid on a macroscopic scale is no longer limited to philosophical discussions but in the reach of experimental physics [2]. We are actually able to experiment with increasingly large quantum objects [3] [4] [5]. Typically such experiments exploit in some way the wave nature inherent in a quantum system [6], a feature that can be revealed by means of diffraction or interferometry. This has first been demonstrated with electrons [7] [8] and small molecules [9], later for neutrons [10] [11] and atoms [12] [13]. In the later 1990's advanced nano fabrication methods allowed to create finer and finer diffraction elements so that matter-wave interferometry became feasible with massive particles such as the C₆₀-fullerene [14]. Ever since experiments have demonstrated the wave-nature of increasingly large particles [15] [16]. The current record is held by an organic particle with

a mass of 7000 amu [5]. A possible mass limit to the validity of quantum mechanics has yet to be found.

In this thesis the setup of a novel matter wave interference experiment is discussed. While the current experiment is limited to a particle mass of around 25.000 amu, the developed techniques may be used to design a de Broglie-wave interferometer for particles with a mass even exceeding 10^6 amu.

4 Review of Talbot-Lau Interferometry

4.1 History of the Talbot-Lau effect

In 1836 Henry Fox Talbot published an article on the following experiment [17]: sunlight passes through a small orifice into a dark chamber and illuminates a periodic grating. The light transmitted by the grating is magnified by a lens. On a screen behind the lens Talbot observed a periodic structure of green and red lines resembling the geometry of the grating. If the distance between the lens and the grating was increased the red and green lines changed their color to yellow and blue, but at certain distances the lines regained their original colors. Talbot remarks: “it was very curious to observe that though the grating was greatly out of focus of the lens, yet the appearance of the bands was perfectly distinct and well defined” ([17], page 404). Interestingly Talbot notes that this phenomenon can only be observed if the orifice through which the light passes is sufficiently small. Today we know that the observation of interference effects, such as the one described by Talbot, require a certain amount of transversal coherence and that the coherence length is inversely proportional to the pinhole diameter. In 1836, however, the concept of coherence had yet to be introduced.

The interference phenomenon Talbot describes is today referred to as the *Talbot effect*: the diffraction pattern behind a coherently illuminated grating will show the same periodicity as the grating at integer multiples of

the so called Talbot length

$$L_T = \frac{d^2}{\lambda}, \quad (1)$$

where d denotes the grating period and λ the wavelength of the light¹. In classical interferometry the Talbot effect has found application in the imaging of phase objects [18] [19].

In 1948 Ernst Lau discovered a way to observe the Talbot effect with a spatially incoherent light source [20]. He used the same setup as Talbot but rather than using sunlight and a small pinhole he used mercury and sodium-vapor lamps. Additionally he placed a second grating before the existing one. Although the light sources were spatially incoherent he observed images of the second grating at positions consistent with the prediction of the Talbot effect. This can be explained by interpreting the first grating as an array of single slits. Incoherent light passing through this mask will give a coherence function that equals the diffraction pattern one would observe while illuminating the grating with coherent light. In optics this is known as the van Cittert-Zernike theorem (see e.g. [21]). Today we refer to the Talbot effect which is observable without a spatially coherent light source as the Talbot-Lau effect.

4.2 The Talbot-Lau Interferometer as a tool for matter wave optics

Since the Talbot-Lau effect opens up to the possibility of observing interference effects with rays emitted from an incoherent source it is predestinated for the use in de Broglie-wave optics. Also, due to the favorable mass-scaling behavior, the Talbot-Lau interference scheme is of particular interest for experiments with high mass particles. This is one of the benefits of operating in the near field regime and becomes evident when considering equation (1): if the grating distance and wavelength spread remain unaltered, the observation of de Broglie interference with 16-times heavier particles

¹A pattern with the same phase reappears at twice L_T .

requires the grating period d to decrease only by a factor of 4. This applies equivalently to the length of the interferometer, so that the flight distance of the particles may be kept short. Together with the relaxed beam collimation requirements this is of great importance, since it allows for higher count rates with respect to comparable far-field schemes [14] [22]. Keeping the signal loss as small as possible is a central aspect of high-mass interferometry especially since the implementation of sufficiently bright sources and efficient detectors becomes more and more challenging when the particle mass increases [23] [24].

A conventional Talbot-Lau Interferometer (TLI) for matter waves consists of three material gratings, spaced by integer multiples of the Talbot length: the first prepares spatial coherence in an initially incoherent beam, the second one projects a diffraction pattern onto the third which is scanned perpendicular to the propagation direction of the beam. The interferogram is then obtained by measuring the transmission through the interferometer as function of the position of the third grating.

The capabilities of a Talbot-Lau matter wave interferometer have first been demonstrated in 1994 by Clauser et al. [25] who managed to obtain up to 80% interference contrast in a beam of slow potassium atoms. In 2002 the Vienna Group reported for the first time on a successful Talbot-Lau interference experiment with C_{70} -fullerenes [15]. Three free standing gold gratings with a grating period of $1\ \mu\text{m}$ and apart from one another by 22 cm formed the interferometer while the beam of C_{70} -molecules was emitted from a sublimation oven. Wavelength selection of the particle beam was done by means of a gravitational velocity selector. The third grating was mounted on a piezo driven translation stage so that it could be scanned over the interference pattern while measuring the three-grating transmission with an ion counter. With this setup the group achieved an interference visibility of 40% and was able to assign this effect unambiguously to the quantum wave nature of the particles by demonstrating a distinct velocity dependence of the contrast. Only a year later high contrast interferometry succeeded with essentially the same setup and beams of tetraphenylporphyrin (TPP) and fluorofullerenes ($C_{60}F_{48}$) respectively, which were not only the heaviest

particles ($m_{TPP}=614$ amu and $m_{C_{60}F_{48}}=1632$ amu) but also the first organic molecules to exhibit de Broglie wave nature to that date [26]. It became clear, however, that the van der Waals interaction between the particles and the grating material considerably reduced the interference contrast due to imposing a velocity and position dependent phase shift onto the passing de Broglie waves. Therefore the mass for a material grating experiment is ultimately limited by interactions between the particles and the grating material: not only does the van der Waals potential scale with $1/r^3$ and thus become more influential as the grating slit period becomes narrower, but it also tightens the requirements for the velocity selection [15]. These difficulties motivated the idea of using structures made of light instead of material gratings. The proposal of this idea dates back to 1933, when Kapitza and Dirac (KD) suggested the diffraction of a beam of electrons on a standing light wave [27]. They interpreted the effect as a result of electrons fictionally absorbing a photon from one mode of the standing wave and experiencing a recoil due to the subsequent stimulated re-emission of the photon into the opposite mode of the standing wave. The experimental challenge inherent in this proposal is manifest in the fact that its full verification took until 2001, when finally Freimund et al. reported on the successful diffraction of electrons from a standing light wave [28]². In 1966 Altshuler et al. highlighted that the KD effect needn't be restricted to electrons but in fact applies to arbitrary scatterers as well [30]. This conjecture was verified in the 1980's when the diffraction of sodium atoms by a standing light wave was demonstrated [31] [32]. The authors however were able to trace the effect back to a light-atom interaction (rather than a resonant photon-absorption and re-emission effect), namely the coupling of the induced atomic dipole moment to the standing wave light field. Later such *phase gratings* were used to realize a Mach-Zender type atom interferometer [33].

While the technique worked particularly fine for atoms, phase grating diffraction of larger molecules seemed somewhat complicated by the higher

²Deflection of electrons in a Kapitza-Dirac type experiment was accomplished already in 1988 [29], however the 2001 experiment was the first to exhibit purely quantum mechanical diffraction peaks and thus provide evidence for an effective separation of the electronic de Broglie waves at the light grating.

photon absorption cross section. The reason for this is that absorption of a photon in the light grating transfers a random recoil momentum onto the particles and thus adds incoherently to the phase grating diffraction. It was shown, however, in 2001 that phase gratings are just as beneficial for macro molecule interferometry as they are for atom optics: far-field diffraction of C_{60} and C_{70} -fullerenes in a phase grating interferometer succeeded in Vienna [34]. Nevertheless the experiment showed that the contribution of photon absorption could not be neglected and did in fact have a visibility reducing effect on the experiment.

A phase grating molecular TLI was first realized in 2007 with the successful implementation of the Kapitza-Dirac Talbot-Lau interferometer (KD-TLI), which utilizes a phase grating as the diffraction element (middle grating) [16]. Apart from this the interferometer resembles a conventional TLI with material gratings and ion-counting detection. Again photon absorption is recognized as a visibility reducing effect which makes the interferometer particularly suited for molecules with high polarizability and small photon absorption cross section. The latter is rarely a feature of large molecules which can be partially compensated by keeping the interaction time of the molecules with the light grating as short as possible (i.e. small waist of the laser grating and, if possible, high particle velocities). In first experiments a visibility of 23% and 18% was obtained for C_{70} and $C_{30}H_{12}F_{30}N_2O_4$ respectively. The fact that these experiments were done with a particle velocity spread of roundabout 20% clearly demonstrates the benefits of the phase gratings: for a C_{70} experiment in a similar setup with three material gratings only a much narrower velocity distribution is acceptable ($\approx 0,7\%$). It is estimated that in the presence of dispersive van der Waals forces at the material center grating the contrast would decrease by an order of magnitude at 20% velocity spread [16].

In the past four years the KD-TLI has been platform to many interesting experiments. Not only does the setup hold the current record for the heaviest quantum object to reveal its wave nature, namely $C_{60}[C_{12}F_{25}]_{10}$ with a mass of nearly 7000 amu [5], but it has also given insight in molecular dynamics during the flight through the interferometer [35] [36] and has allowed to

measure molecular properties with high precision [37] [38].

Although the mass limit for the KD-TLI is not yet reached, it is clear that interference experiments with increasingly heavy particles will become more and more challenging, this being mainly due to the lack of sufficiently bright organic-particle sources and the influence of incoherent photon absorption. At this point the motivation for the *Optical time-domain ionizing matter wave* TLI (OTIMA-TLI) emerges: this interferometer, as it is described in this thesis, utilizes the novelty of three ionizing absorptive laser gratings. It aims at revealing the quantum wave nature of particles up to 10^6 amu. While it is to date unclear whether the current setup or a modified future version will achieve this goal, the ionising laser gratings seem to be the ideal tool for this challenge: they render the indestructibility and perfect periodicity of a phase grating without suffering from detrimental photon absorption. They function with a wide range of particles and leave the option open to be operated as a phase grating after all. Additionally the novel scheme works in the time-domain [39] [40] [41] [42], which in principle makes a velocity selection in the particle beam dispensable and thus removes a significant source of signal loss.

4.3 OTIMA-interference scheme

Figure 1 shows the setup of the OTIMA-interferometer. A cloud of particles is emitted from a pulsed source and flies in the close proximity of a mirror. While passing by the mirror the particles are subjected to three VUV-laser (*Vacuum Ultra Violet*) pulses with a wavelength of $\lambda_{VUV} = 157$ nm, delayed with respect to each other by integer multiples of the *Talbot time* [39]:

$$T_t = \frac{md^2}{h}, \quad (2)$$

where m is the particle mass, $d = \lambda_{VUV}/2$ and h the Planck constant. The laser pulses are focused and timed in such a way that ideally all particles within the cloud are illuminated by the laser. Since this is difficult to achieve due to the inherent longitudinal spread of the particle cloud one at least has to ensure that no particles “see” less than all three laser pulses.

4.3 OTIMA-interference scheme

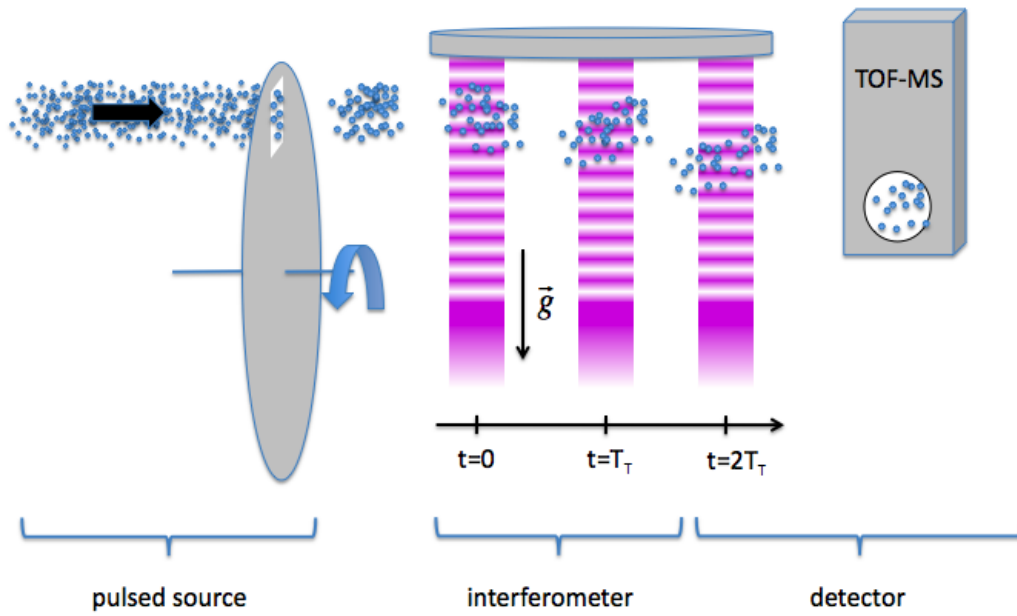


Figure 1: Schematic view of the OTIMA-TLI: a cw particle beam is chopped into short packets by a rotating disk chopper. The particles then enter the interferometer, which consists of three pulsed 157 nm gratings spaced in time by T_t . After leaving the interferometer the particles are detected with a time-of-flight mass spectrometer.

Within the standing wave two processes are possible: first, the particles may be photo-ionized, where the probability for this to happen depends periodically on their distance to the mirror. An external electric field will then remove the ions from the beam. In this case the laser pulse acts similar to an absorptive grating with the periodicity of half the laser wavelength. The second possible process is a phase shift of the de-Broglie waves due to a coupling of the light field to the particle's polarizability. If the photon energy exceeds the particles ionisation potential, the pulse is likely to act as a absorptive grating. If, however, the laser power is not sufficient to photo-ionize the particles the pulses will act purely as phase gratings. As it will be shown in detail in section 5.2, the first and third grating necessarily have to be absorptive gratings, while the middle one might as well be a phase grating. Apart from utilizing laser gratings and operating in the time-domain, the OTIMA-interferometer works similar to a conventional TLI: the first grating prepares the transversal coherence of the particle cloud, which is then diffracted by the second grating. The diffraction pattern is subsequently recorded by measuring the intensity of the particle beam behind the third grating with a *time-of-flight* mass spectrometer (TOF-MS). Since the respective phases of the gratings are fixed by the mirror surface, the possibility of scanning the third grating in order to obtain the diffraction pattern is not given. Instead, one can measure the transmission through the interferometer as a function of the particle deflection in the presence of a constant force field perpendicular to the particle beam. For large masses the earths gravitational field is well suited for this purpose. For small masses, on the other hand, twice T_t might be too short in order for the particles to be gravitationally deflected in this time by more than half a grating period. In this case an electric field can be applied as a deflection field. Using a cluster source in the current OTIMA setup, however, opens up to the implementation of a particularly simple detection scheme: the diffraction pattern can be obtained by measuring the transmission as a function of the cluster mass. Clusters for which the Talbot-Lau resonance condition is fulfilled will show enhanced or reduced transmission, visible in a modulation of the classical transmission function.

5 Theoretical treatment

5.1 Physics of metal clusters

One advantage of the OTIMA-interference scheme is that it works with a large range of particles. Their suitability for the experiment is merely limited by availability of a sufficiently bright source and their ionisation potential which should lie beneath the energy of a 157 nm-photon (7.8 eV). Candidates for the OTIMA-TLI are thus clusters of many atomic species (Alkali metals, rare earth metals among many others) as well as some organic complexes (e.g. anthracene, perylene, porphyrine). Since the current setup aims at probing the wave nature of metal clusters this section will in brief review the optical and electrical properties of metal clusters.

Metal clusters are ensembles consisting of up to thousands of atoms. The so called *jellium model* has proven to be capable of explaining the properties of the electronic band structure of alkali [43] [44] and noble metal clusters [45] [46] of up to hundreds of atoms. It assumes that the valence electrons of the constituent atoms are delocalized over the entire ionic core of the cluster. One can therefore approximate the cluster by a structureless spherical distribution of positive charges which trap the electrons in a spherically symmetric potential well. By solving the Schrödinger equation of this system one arrives at a discrete level system of eigenenergies like this is known from atoms [47]. Clusters with the exact amount of free electrons to close a shell ("*magic clusters*") will exhibit a larger stability and thus appear more often in abundance spectra [48]. Besides enhancing the stability of a cluster, shell closing effects also have an impact the ionisation potential. This is relevant since on the one hand their ionization potential qualifies particles for the use in the OTIMA-TLI. On the other hand ionization potentials may be measured in the interferometer with high precision [49].

The ionisation potential (IP) is defined as the energy difference between the

neutral and the ionized ground state cluster³. A simple approximation is to treat the cluster as a small conducting sphere [50]. This model assumes that the IP consists of the bulk work function W_∞ and the electrostatic energy binding the electron to the positive core of the cluster body. If the latter contribution is assumed to be simply $e^2/2R$, with R being the cluster radius and e the elementary charge, the IP reads [50]:

$$IP = W_\infty + \frac{e^2}{2R}, \quad (3)$$

which approaches the value for $R \rightarrow \infty$.

Experimentally it is found that the general decrease of the IP with increase of the cluster number exhibits larger steps. This can be seen in the measurement results shown in figure 2. The steps are associated with shell closing numbers, while the overall decrease of the IP is due to electrostatic effects according to equation (3).

For our experiments particles are chosen such that their IP lies well beneath ($> 0,5 \text{ eV}$) the energy of a VUV-photon. For the simulation of interference contrast we make the assumption that every absorption of a photon instantaneously leads to ionisation of the cluster.

It might be possible to observe shell closing effects, like the ones visible in figure 2, in an OTIMA-experiment. They however do not affect an interference measurement since they occur in the classical transmission as well as in the quantum mechanically modulated transmission and thus cancel out after subtraction of the former from the latter.

5.1.1 Photon absorption cross sections of small metal clusters

Since the OTIMA-TLI works with laser gratings, photon absorption cross section as well as dipole polarizabilities of the particles have to be at least known approximately. For this we employ a scattering model in the frame

³Strictly speaking this is the definition of the *adiabatic* ionisation potential. It differs from the *vertical* ionisation potential by an amount of energy that may be lost to a deformation of the cluster during the ionisation process. For large clusters the difference between the two is negligibly small and since the OTIMA-TLI aims at experiments with high mass clusters we shall not make the distinction here.

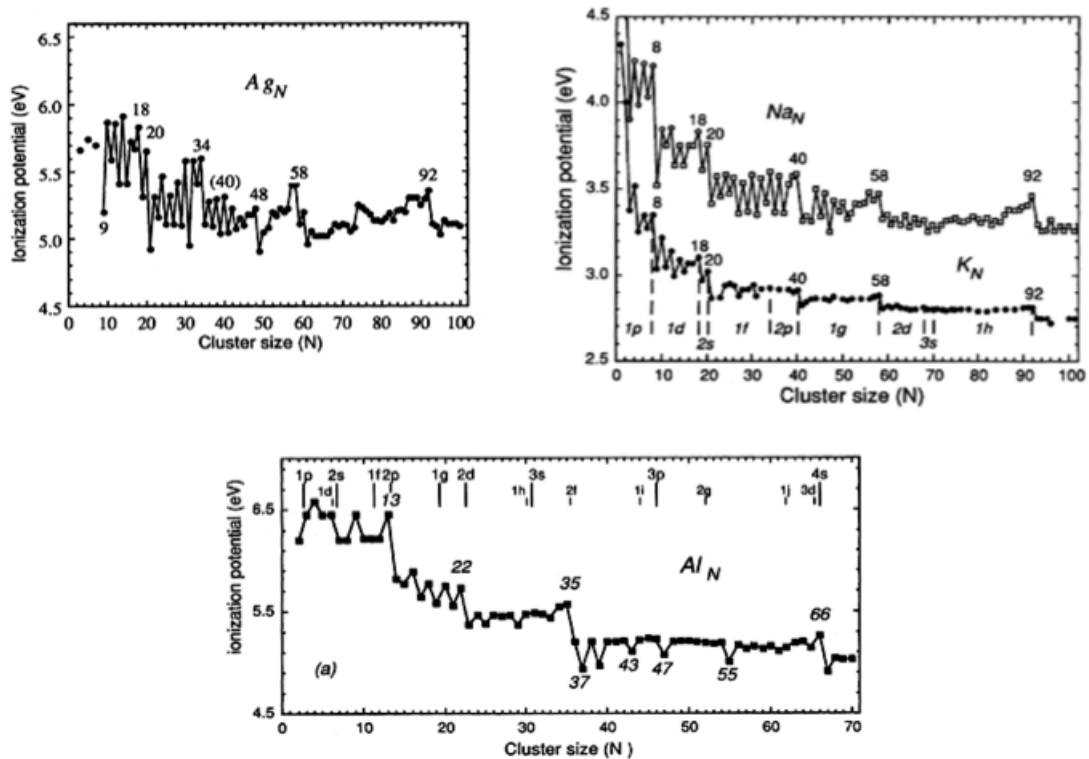


Figure 2: Measured Ionisation potentials as function of the cluster number N , for silver (top left), potassium and sodium (top right) and aluminum (bottom center). Figures taken from [50])

of the Mie theory [51]. The model is expected to be accurate for particles much smaller (or larger) than the laser wavelength and yet large enough to be approximated by a sphere. Hence it should be applicable for the 10 to few thousand-fold metal clusters probed in the OTIMA-interferometer.

In Mie theory the Maxwell equations are solved for the scattering of plane waves of light at a spherical dielectric particle. The Maxwell equations describing the propagation of light (with frequency ω) through a homogeneous linear and isotropic medium reduce to the wave equations

$$\nabla^2 \mathbf{E} + \omega^2 \epsilon \mu \mathbf{E} = 0 \quad (4)$$

$$\nabla^2 \mathbf{H} + \omega^2 \epsilon \mu \mathbf{H} = 0, \quad (5)$$

where \mathbf{E} and \mathbf{H} denote the electric and magnetic field respectively, $\epsilon = \epsilon_0 \epsilon$ stands for the permittivity (equals the vacuum permittivity times the dielectric function) and μ is the permeability [47]. Additionally the following relations hold:

$$\nabla \times \mathbf{E} = i\omega \mu \mathbf{H}, \quad \nabla \cdot \mathbf{E} = 0 \quad (6)$$

$$\nabla \times \mathbf{H} = -i\omega \epsilon \mathbf{E}, \quad \nabla \cdot \mathbf{H} = 0. \quad (7)$$

It is convenient to introduce the vector functions $\mathbf{N} = 1/k(\nabla \times \mathbf{M})$ and $\mathbf{M} = \nabla \times \mathbf{r}\psi$ where \mathbf{r} is the position vector and ψ a scalar function satisfying

$$\nabla^2 \psi + \omega^2 \epsilon \mu \psi = 0. \quad (8)$$

This equation originates from the condition that the tangential components of \mathbf{E} and \mathbf{H} should be continuous at the surface of the sphere. Due to the spherical symmetry of the boundary condition it makes sense to express solutions of (8) in spherical coordinates (ϕ, θ, r) . These solutions depend on the associated Legendre polynomials P_n^ℓ and the spherical Bessel functions z_n . They read [47]:

$$\psi_{\ell n}^e = \cos(\ell\phi) P_n^\ell[\cos(\theta)] z_n(kr) \quad (9)$$

$$\psi_{\ell n}^o = \sin(\ell\phi) P_n^\ell[\cos(\theta)] z_n(kr), \quad (10)$$

where we have made the distinction between ordinary (superscript “e”) and extraordinary solution (superscript “o”). We may now first express the functions \mathbf{N} and \mathbf{M} by means of (9) and denote them $\mathbf{N}_{\ell n}^{e/o}$ and $\mathbf{M}_{\ell n}^{e/o}$ respectively. This enables us to expand the incident field \mathbf{E}_i (polarized along

the z-direction) and the scattered field \mathbf{E}_s into partial waves:

$$\mathbf{E}_i = E_0 e^{i k r \cos(\theta)} \mathbf{e}_x = E_0 \sum_{n=1}^{\infty} i^n \frac{2n+1}{n(n+1)} (\mathbf{M}_{\ell n}^o - i \mathbf{N}_{\ell n}^e) \quad (11)$$

$$\mathbf{E}_s = E_0 \sum_{n=1}^{\infty} i^n \frac{2n+1}{n(n+1)} (i a_n \mathbf{N}_{\ell n}^e - b_n \mathbf{M}_{\ell n}^o). \quad (12)$$

The coefficients a_n and b_n are fixed by the boundary conditions at the sphere's surface. They fully determine the absorption cross section, which is defined as a ratio between incoming and outgoing flux in forwards direction [52]:

$$\sigma_{ext} = \frac{2\pi}{|\mathbf{k}^2|} \sum_{n=1}^{\infty} (2n+1) \text{Re}[a_n + b_n]. \quad (13)$$

The index n is the order of the multipole excitation in the particle. In the *sub-wavelength* approximation ($R \ll \lambda_{laser}$), however, it is found that $a_n \propto (kR)^{(2n+1)}$ and $b_n \propto (kR)^{(2n+3)}$. Higher order multipoles thus do not contribute notably to σ_{ext} and we find the absorption cross section for sub-wavelength clusters surrounded by vacuum to be:

$$\sigma_{ext}(\omega) = \frac{18\pi m}{\rho \lambda_{laser}} \frac{\varepsilon_2(\omega)}{[\varepsilon_1(\omega) + 2]^2 + \varepsilon_2(\omega)^2}, \quad (14)$$

where $\rho = 3m/4\pi R^3$ is the mass density of the cluster and $\varepsilon(\omega) = \varepsilon_1(\omega) + i\varepsilon_2(\omega)$ is the dielectric function [52].

Within the frame of the OTIMA-experiment equation (14) is used for the simulations of interference contrast for clusters with a mass up to 10^6 amu. For larger clusters this becomes inaccurate [53], and one might have to take into account higher-order terms of σ_{ext} .

5.1.2 Polarizability of small metal clusters

For nearly spherical sub-wavelength particles (with a radius of around 1% of the wavelength) one may treat the response to an external electric field by means of electro-statics. Technically this is done by solving the Maxwell

equations in the zero frequency limit $\omega \rightarrow 0$ which effectively reduces equations (4) and (5) to the Laplace equation. The frequency dependence is then introduced by inserting the frequency dependent (bulk) value for the dielectric function [47]. This is known as the *quasi-static* approximation, where one assumes that the ionic core of a cluster (as it has been introduced with the Jellium model above) is immobile and merely the free-electron gas surrounding the core reacts to an external electric field. The field inside a small sphere with dielectric constant ε and embedded in vacuum reads:

$$E_i = \frac{3E_0}{\varepsilon + 2}. \quad (15)$$

The corresponding induced polarisation of a metal sphere of radius R is defined as $P = \alpha(\lambda_{laser})E_0$ with

$$\alpha(\lambda_{laser}) = R^3 \cdot \text{Re} \left[\frac{\varepsilon(\lambda_{laser}) - 1}{\varepsilon(\lambda_{laser}) + 2} \right] = \frac{3m}{4\pi\rho} \frac{\varepsilon_1(\omega)^2 + \varepsilon_2(\omega)^2 + \varepsilon_1(\omega) - 2}{(\varepsilon_1(\omega) + 2)^2 + \varepsilon_2(\omega)^2}, \quad (16)$$

where $\varepsilon(\lambda_{laser})$ is the dielectric function of the cluster material at the laser wavelength [52].

5.2 Evolution of quantum states in the OTIMA-TLI

In this section we present a phase space model that describes the propagation of a particle beam through the OTIMA-interferometer, closely following [54] [55] [56] [57] [53]. For a first approach the calculations will be simplified by several approximations: the beam will be assumed to be perfectly monochromatic in the y-direction and remain so during the flight, which means that longitudinal states of the beam will be disregarded during the passage through the interferometer. This is known as the *eikonal approximation* [54]. We may apply this simplification since, on the one hand, the particles interact too shortly and too weakly with the light field in order for their trajectories to be altered by the laser gratings⁴ and, on the other hand, in the time-domain treatment the y-direction velocities

⁴i.e. if they are not ionized.

5.2 Evolution of quantum states in the OTIMA-TLI

do not enter the calculations at all. It is also a good approximation to neglect any motion in the z -direction (see figure 3) since the transmission through a TLI is unaffected by translation parallel to the grating slits. This leaves us with an effectively one dimensional treatment of the translational beam state [55]. It is most generally described by its density matrix ρ .

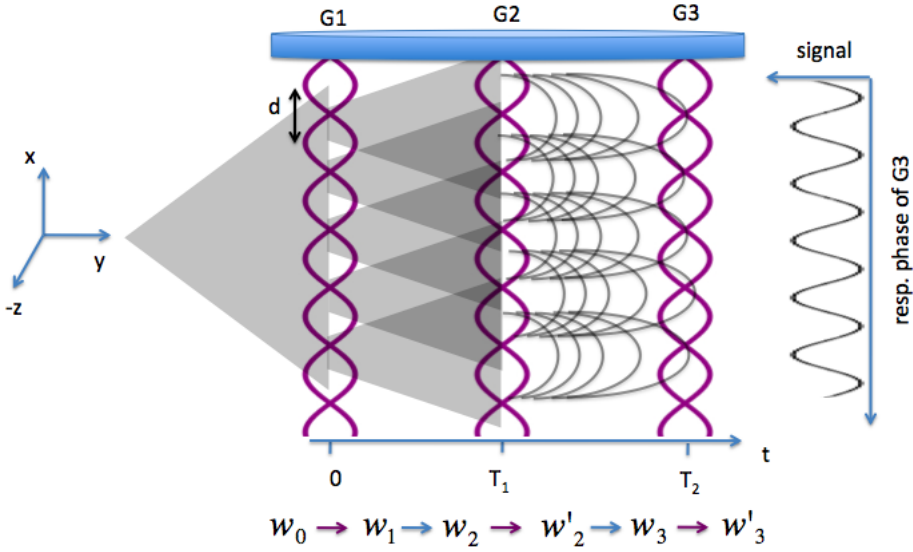


Figure 3: Propagation of the transverse beam state from left to right: the initial Wigner function $w_0(x, p)$ is convolved with the grating G1 and subsequently by a free space propagation for the time T_t . The beam is now in a state $w_1(x, p)$ and coherently illuminates G2. Diffraction takes place and after another free space propagation lasting again for the time T_t , the position dependent density distribution is recorded. d denotes the grating period which is the same for all three gratings (*figure adapted from* [54]).

A convenient representation in terms of phase space variables is given by the Wigner function, which can be interpreted as the quantum mechanical equivalent of a classical phase space distribution. Proceeding in the Wigner representation offers the advantage of resulting in phase space distributions and thus allowing direct comparison to the classical description of the OTIMA-TLI [55]. This is of great importance since in a TLI classical shadow effects will produce fringe patterns similar to those due to quantum

interference (see section 5.6).

The Wigner function for the transversal beam state reads:

$$w(x, p) = \frac{1}{2\pi\hbar} \int ds \quad e^{ips/\hbar} \langle x - \frac{s}{2} | \rho | x + \frac{s}{2} \rangle, \quad (17)$$

and depends on the phase space coordinates (x, p) [53]⁵. During propagation through a TLI the Wigner function undergoes two types of transformations: free propagation and passage through a grating. Before and in between the gratings the particles propagate freely in the y-direction, while being deflected by a constant force $F_{def} = ma$ in z-direction⁶. This corresponds to a shearing transformation of the Wigner function:

$$w(x, p) \rightarrow w \left(x - \frac{t}{m}p + \frac{a}{2}t^2, p - mat \right) \quad (18)$$

where t the propagation time. This is equivalent to the transformation of a classical phase space density during the flight in a homogenous force field. Deviations from the classical descriptions arise as soon as the particles pass a grating. Transmission through the i -th grating is described by a grating function $t_j(x)$ which is defined in section 5.4. The grating transformation is represented by a convolution of the Wigner function in phase space [54]

$$w(x, p) \rightarrow w'(x, p) = \int dp_0 K_j(x, p - p_0) w(x, p_0), \quad (19)$$

where $K_j(x, p)$ is defined as a function of $t^{(j)}(x)$:

$$K_j(x, p) = \frac{1}{2\pi\hbar} \int ds e^{\frac{i}{\hbar}ps} t^{(j)} \left(x - \frac{s}{2} \right) (t^{(j)})^* \left(x + \frac{s}{2} \right) \quad (20)$$

Initially we assume the beam to be spatially incoherent. This means that on the scale of the grating period the momentum distribution is close to constant. In order to arrive at an expression for the transversal coherence, we consider the 3-dimensinal momentum distribution of the beam and obtain the transversal momentum distribution $D(p)$. The Fourier transformation of

⁵We set $p = p_x$ throughout the calculations

⁶ F_{def} could e.g. be caused by the earth's gravitational field or a suitably applied electrostatic field

$D(p)$ is a measure for the transversal coherence length. It reads:

$$\tilde{D}(s) = C \int dp D(p) e^{-ips/\hbar}, \quad (21)$$

where the normalization factor C is defined by $\tilde{D}(0) = 1$. Before the particles pass through the first grating $\tilde{D}(s)$ can be approximated by a function sharply peaked at $s = 0$. This describes the situation of the beam initially being incoherent on the scale of the grating period. The transversal momentum distribution Δp of the beam prior to entering the interferometer is thus much broader than the momentum kick \hbar/d which the particles experience during the passage through the grating. For this reason diffraction does not take place at the first grating and we can describe the first grating as a purely classical mask [53], which means that the Wigner function undergoes the transformation

$$w(x, p)_0 \rightarrow |t^{(1)}(x)|^2 w(x, p)_0 \quad (22)$$

at the first grating. If the state of the beam is initially described by $D(p)$ we thus find the state after the first grating to read:

$$w(x, p)_1 = |t^{(1)}(x)|^2 D(p) \frac{1}{\Delta x}. \quad (23)$$

This state is subjected to a free space propagation of duration T_1 acting like the transformation (18), diffracted according to equation (19) and detected after freely propagating for the time T_2 . In the experiment the position distribution in the particle beam is recorded rather than the phase space density. It is therefore convenient to express the result in terms of the position integrated Wigner function [53]:

$$\begin{aligned}
 w_3(x) &= \int dp \quad w_3(x, p) & (24) \\
 &= \frac{1}{\Delta x} \int dp_0 K_2 \left(x - \frac{pT_2}{m} + \frac{a}{2}T_2^2, p - p_0 - maT_2 \right) D(p_0 - maT_1) \\
 &\quad \cdot \left| t^{(1)1} \left(x - \frac{pT_2 + p_0T_1}{m} + \frac{a}{2}(T_1^2 + T_2^2) \right) \right|^2,
 \end{aligned}$$

Since the grating functions $t^{(j)}(x)$ are periodic in d we can Fourier expand them so that

$$t^{(j)}(x) = \sum_n b_n^{(j)} \exp\left(\frac{2\pi i n x}{d}\right), \quad (25)$$

where we have introduced the Fourier coefficients $b_n^{(j)}$. If we insert this into the equations (20) and (24) we arrive at

$$w_3(x) = \frac{1}{\Delta x} \sum_{n, \ell=-\infty}^{\infty} \exp\left(\frac{2\pi i \ell (x - a(T_1 + T_2)^2)}{d}\right) \quad (26)$$

$$\tilde{D}\left(\frac{d(nT_1 + \ell T_2)}{T_t}\right) B_n^{(1)}(0) B_{\ell-n}^{(2)}\left(\frac{\ell T_2}{T_t}\right), \quad (27)$$

which is evidently periodic in d as well. Here it was convenient to introduce the *Talbot-Lau coefficients*

$$B_n^{(j)}(\xi) = \sum_n b_j b_{j-n}^* \exp(i\pi \xi (n - 2j)). \quad (28)$$

In the case of the first grating this reduces to $B_n^{(1)}(0)$ which is exactly the Fourier coefficient of the transmission probability at the first grating.

We can now further simplify (26) by assuming a nearly symmetric TLI, where

$$T_1 \approx T_2 + \tau \quad \text{with} \quad \tau \ll T_t. \quad (29)$$

Together with the fact that $\tilde{D}(s)$ is sharply peaked for arguments $s \ll d$, condition (30) narrows the number of summation indices (n, ℓ) contributing notably to $w_3(x)$. Under the assumption of a completely incoherent illumination of the first grating we arrive at the strict *resonance approximation*:

$$\tilde{D}\left(\frac{d}{T_t}(nT_1 + \ell T_2)\right) \approx \delta_{n, -\ell}. \quad (30)$$

Inserting (29) and (30) into (26) gives us the position dependent density distribution at the time of the third grating pulse:

$$w_3(x) = \quad (31)$$

$$\frac{1}{\Delta x} \sum_{\ell=-\infty}^{\infty} \exp\left(\frac{2\pi i \ell (x - a(T_1 + T_2)^2)}{d}\right) B_{-\ell}^{(1)}(0) B_{2\ell}^{(2)}\left(\frac{T_2}{T_t}\right). \quad (32)$$

The third grating pulse now acts as a classical mask, which modulates the fringe pattern by the same Fourier components (52) as G1. We obtain the signal

$$S = \int dx w_{2T_t}(x) |t^{(3)}(x)|^2, \quad (33)$$

where $t^{(3)}(x)$ is the transmission function of G3 and $|t^{(3)}(x)|^2$ gives the probability for a particle at position x to be transmitted by the grating⁷. The signal eventually transmitted into the detector thus reads:

$$S(x) = \quad (34)$$

$$\sum_{\ell=-\infty}^{\infty} \exp\left(\frac{2\pi i \ell (x - a(T_1 + T_2)^2)}{d}\right) \tilde{D}\left(\frac{d\tau}{T_t}\right) B_{-\ell}^{(1)}(0) B_{2\ell}^{(2)}\left(\frac{T_2}{T_t}\right) B_{-l}^{(3)}(0). \quad (35)$$

⁷The design of the OTIMA-TLI in principle also allows for the operation with *inverse* gratings, where the ions are not removed but transmitted and subsequently detected. In this case the signal would read $S(x) = \int dx w_{2T_t}(x) (1 - |t^{(3)}(x)|^2)$ [53].

The results of section 5.4 will provide a more detailed specification of the gratings transmission functions. This will allow us to calculate the fringe visibility of the signal (34) and thus permit to simulate measurement outcomes for different experimental parameters.

5.3 Aligning requirements

If the illumination of G1 is transversally incoherent there is no fixed phase relation between the elementary de Broglie waves emitted by the G1-slits. If now the grating delays are equal, a fixed phase relation arises between the de Broglie waves to the time of second grating pulse and interference becomes observable. This is however only the case if the interferometer is perfectly aligned, i.e. the gratings are parallel, all three grating periods and the delays between the gratings are equal. In the situation of an initially incoherent beam the slightest misalignment would destroy the interference pattern. Since a perfect alignment is experimentally not feasible we have to reduce the number of slits N illuminated by the particle beam, in other words we have to collimate the beam. This leads to an easing of equation (30) which reads

$$\tilde{D}\left(\frac{d(nT_1 + \ell T_2)}{T_t}\right) \approx \delta_{n,-\ell} \tilde{D}\left(d\frac{\delta\tau}{T_t}\right). \quad (36)$$

where we allow for a pulse timing imprecision of $\delta\tau$. To find an upper bound for the argument of \tilde{D} in (36) we consider figure 4. If the G3-pulse (or G1-pulse) is early by $\delta\tau$, partial waves diffracted by G2 will not recombine exactly at a slit opening of G3 but instead stay separated by a distance l . This reduces the fringe visibility which tends to zero as l approaches $d/2$. Due to the intercept theorem, $\delta\tau/T$ may therefore not exceed $1/N$, where N is the number of G2-slits illuminated by the particle beam. We find that in the paraxial approximation N is connected to the divergence of the beam α via

$$\tan \alpha \approx \alpha = \frac{Nd}{L}, \quad (37)$$

5.3 Aligning requirements

where L is the spatial distance between the gratings⁸. We arrive at

$$\frac{\delta\tau}{T_t} < \frac{d}{\alpha L}. \quad (38)$$

This shows that taking advantage of a broad beam and thus more signal leads to stricter pulse jitter requirements.

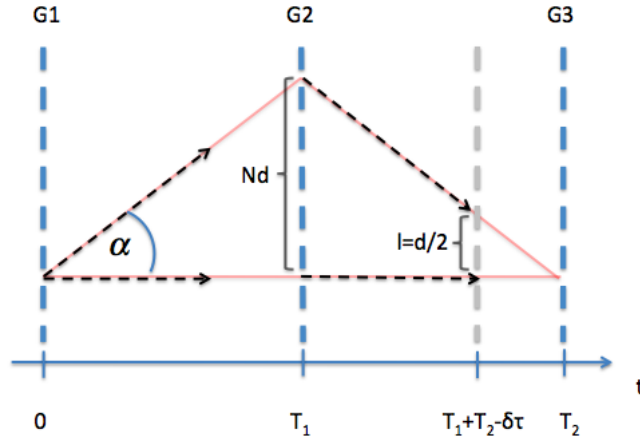


Figure 4: Semiclassical particle trajectories in the OTIMA-TLI are shown in red. The mistiming of G3 by $\delta\tau$ gives rise to a reduction of visibility. The contrast washes out entirely if $l = d/2$, where l is the separation of the beam paths in the plane of G3. α denotes the divergence of the particle beam and N is the number of G2-slits that are illuminated by the beam. (*figure adapted from [56]*)

⁸The divergence of the particle beam is here defined as $\alpha = \Delta p/p_x$, where the momentum distribution as well as the mean particle momentum in x-direction enter. We can further assign a spatial position to the gratings and define a spatial separation of the pulses via $L = T \cdot p_x/m$. Usually neither L nor α appear in the time-domain treatment. These definitions, however, are handy since they allow to formulate criteria for the alignment precision by means of experimental parameters rather than abstract variables such as the momentum distribution.

5.4 Theory of the laser gratings

A particle's wave function undergoes a transformation

$$\psi(x)' \rightarrow t^{(j)}(x)\psi(x) \quad (39)$$

while passing a grating, where $t^{(j)}(x)$ is the complex valued grating transmission function associated with the j -th grating as introduced in section 5.2. We are allowed to treat the grating transformation as such an instantaneous change of the wavefunction since the pulse length is short compared to the time it takes the particles to cross of the beam. We can thus assume the particles to be at rest during the laser pulse.⁹ In the following the function $t^{(j)}(x)$ is derived for our laser gratings.

We consider the case of a Gaussian laser beam with the intensity profile

$$g(y, z) = \frac{2}{\pi w_y w_z} \exp\left(-\frac{2y^2}{w_y^2} - \frac{2z^2}{w_z^2}\right), \quad (40)$$

with w_y and w_z being the waist diameters along the y respectively z direction. The time dependant three dimensional intensity distribution of the standing wave with periodicity $\lambda_{UV}/2$ and power $P_L(t)$ is then:

$$I(x, y, z, t) = 4P_L(t)g(y, z) \cos^2\left(\frac{\pi x}{d}\right). \quad (41)$$

We neglect the y -dependence in a sufficiently broad laser beam. The photon flux is given by $\phi(x, z) = 2I(x, z)d/(hc)$ and leads to the photon absorption rate

$$R(x, z) = \sigma_{abs}\phi(x, z), \quad (42)$$

with the photon absorption cross section σ_{abs} . Under the assumption that every photon absorption leads to ionization of the particle, σ_{abs} is equal to the ionization cross section [58]. The mean number $n^{(j)}(x)$ of absorbed photons per cluster subjected to the j -th grating pulse for the time Δt is obtained by

⁹If the average beam velocity in the OTIMA-TLI is $300m/s$, the particles fly a distance of 300 nm in a 10 ns pulse. The collimation of the particle beam allows us to assume the particles to be at rest during a pulse also along the x -direction.

integrating over $R(x, z)$ along the z -coordinate:

$$n^{(j)}(x) = \frac{8\sigma_{abs}\bar{P}_L\Delta t\lambda_{VUV}}{\pi w_y w_z h c} \cos^2\left(\frac{2\pi x}{d}\right) \equiv n_0^{(j)} \cos^2\left(\frac{\pi x}{d}\right), \quad (43)$$

where $n_0^{(j)}$ is the maximum average number of absorbed photons in the j -th grating which is equal to the average number of photons absorbed in an antinode and \bar{P}_L stands for the time-averaged pulse power. The particles that are not ionized in the laser pulse will be transmitted. Since the probability for a particle to randomly absorb a photon is independent of the number of previous ionization processes the probability distribution is Poissonian. The ionization probability can thus be calculated directly from (43) via

$$|t^{(j)}(x)|^2 = e^{-n^{(j)}(x)}, \quad (44)$$

or may likewise be expressed as a Fourier series:

$$|t^{(j)}(x)|^2 = \sum_{\ell=-\infty}^{\infty} B_{\ell}^j(0) \exp\left(\frac{2\pi i \ell x}{d}\right). \quad (45)$$

The quality of an absorptive laser grating depends on its visibility. In terms of (44) this means that at an antinode $\exp(-n^{(j)}(x))$ should be as small as possible. It is found that for $n_0^{(j)} = 8$ the ionization probability in an antinode is 99.96%. Laser gratings, however, do not only work as absorptive masks but they additionally imprint a position dependent phase onto the particle beam [56]. The phase shift $\phi^{(j)}(x)$ a particle experiences at a certain position is proportional to its dipole polarizability $\alpha(\lambda)$ at the laser wavelength:

$$\phi^{(j)}(x) = \frac{n_0^{(j)}}{\beta} \cos^2\left(\frac{\pi x}{d}\right) \equiv \phi_0^{(j)} \cos^2\left(\frac{\pi x}{d}\right). \quad (46)$$

Here all material characteristics are combined in

$$\beta = \frac{\lambda_{VUV}\sigma_{abs}\epsilon_0}{\pi\alpha} \quad (47)$$

and $\phi_0^{(j)}$ is the phase shift at an antinode. The complex grating

transmission function of the j -th grating therefore reads

$$t^{(j)}(x) = \exp\left(\left(-\frac{n_0^{(j)}}{2} + i\phi_0^{(j)}\right) \cos^2\left(\frac{\pi x}{d}\right)\right). \quad (48)$$

We now introduce the expressions

$$\zeta_{ion} = n_0^{(j)} \cos(\pi\xi)/2 \quad (49)$$

$$\zeta_{phase} = \phi_0^{(j)} \sin(\pi\xi) \quad (50)$$

so that we can write down the Talbot-Lau coefficients for G2 [56]:

$$B_m^{(2)}(\xi) = \exp(-n_0^2/2) \left[\frac{\zeta_{phase} - \zeta_{ion}}{\zeta_{phase} + \zeta_{ion}} \right]^{\frac{m}{2}} J_m\left(\text{sign}(\zeta_{phase} + \zeta_{ion}) \sqrt{\zeta_{phase}^2 - \zeta_{ion}^2}\right), \quad (51)$$

where J_m is a Bessel function of first kind and $\xi = \ell T/T_t$ relates the pulse timing to the Talbot time (2). The Fourier coefficients characterizing the classical masking at G1 and G3 are

$$B_m^{(1,3)}(0) = \exp\left(\frac{-n_0^{(1,3)}}{2}\right) I_m\left(\frac{-n_0^{(1,3)}}{2}\right), \quad (52)$$

with I_m being a modified Bessel function of the first kind. If no ionisation takes place in the first grating, $B_m^{(1)}(0)$ is nonzero only for $m = 0$. A key feature of the OTIMA-setup becomes evident here: while the middle grating acts as a phase grating and simultaneously as an absorptive grating, the first and last grating necessarily need to be absorptive masks [53]. Otherwise the density distribution (26) will not be modulated by the interferometer.

5.5 Interference contrast

The quality of an interference pattern is measured in terms of the fringe contrast or *visibility*, which is defined as a ratio between maximal and

minimal signal intensity in the interferogram:

$$V = \frac{I_{max} - I_{min}}{I_{max} + I_{min}}. \quad (53)$$

Sometimes the signal (34) is suitably well approximated by a sine curve with period d , so that it is sufficient to consider the *sinusoidal* visibility $V_{sin} = |2S_1/S_0|$, where S_m is the m -th Fourier component of the signal. It reads

$$V_{sin} = \left| \frac{2S_1}{S_0} \right| = 2 \frac{I_1(n_0^{(1)}/2) I_1(n_0^{(3)}/2)}{I_0(n_0^{(1)}/2) I_0(n_0^{(2)}/2) I_0(n_0^{(3)}/2)} \times \frac{\left| (\zeta_{phase} - \zeta_{ion}) J_2 \left(\sqrt{\zeta_{phase}^2 - \zeta_{ion}^2} \right) \right|}{|\zeta_{phase} - \zeta_{ion}|}, \quad (54)$$

where ζ_{ion} and ζ_{phase} are defined as in equation (49). Equation (54) now enables us to simulate measurement results for different experimental parameters and particle properties. This will be done in section 5.7.

The next section will provide classical equivalents to ζ_{phase} and ζ_{ion} and thus permit to compare classical and quantum contrast.

5.6 Classical contrast

A fringe pattern in the density distribution of particles transmitted by the TLI does not alone suffice as a proof for the wave nature of the particles: the classical Moiré effect may give rise to a density pattern with the same periodicity as the quantum pattern (e.g. [26]).

Since we have worked in the Wigner formalism so far, computing a classical expression for the density distribution before the third grating pulse requires only to replace the Wigner function (17) by the classical phase space density. This is done in [56]. As it turns out, the classical result differs from the quantum mechanical result only in the definition of ζ_{ion} and ζ_{phase} :

$$\zeta_{ion}^{classic} = \frac{n_0^{(j)}}{2} \quad \text{and} \quad \zeta_{phase}^{classic} = \phi_0^{(j)} \pi \xi. \quad (55)$$

While the phase contribution of the gratings still depends on ξ (and hence on T_t) both parameters no longer exhibit an oscillation in ξ . In the experiment one can thus distinguish between classical patterns and quantum interference, since the former will vanish for large pulse delays $T > T_t$, while the latter will periodically reoccur at integer multiples of T_t .

5.7 Expected visibilities for an OTIMA-interference experiment

With the tools obtained in the past sections we can simulate measurement outcomes as functions of different experimental and material parameters. The first and third grating are fully described by the mean absorption number of photons at an antinode of the standing wave n_0^j , while the center grating additionally has the characteristic of a phase grating in which the particles experience a maximal phase shift of $\phi_0^{(2)}$.

Fitted to the experimental setup of the OTIMA-TLI setup the laser wavelength throughout the calculations is $\lambda_{VUV} = 157,63$ nm. Cluster parameters enter the simulations in form of the material constant β , as defined in (47). It has to be emphasized that β does not depend on the particle mass. This is due to the fact that α and σ_{ext} (defined in (16) and (14) respectively) do not include Mie calculations higher than to zeroth order and thus both depend linearly on the mass. This means that the clusters are assumed to be conducting metal spheres when it comes to the absorption cross section and point dipoles as far as the polarizability is concerned. The permissibility of this assumption is demonstrated in figure 5 which shows the interference contrast of three very large gold clusters in zeroth and 10th order Mie theory. The fact that the results coincide even for masses beyond 10^6 amu shows that higher order Mie theory can safely be neglected in an OTIMA-interference experiment with sub-wavelength clusters. The quantum phenomena observable in the OTIMA-TLI are thus in good approximation

5.7 Expected visibilities for an OTIMA-interference experiment

mass-scale invariant for constant T/T_t and n_0 .

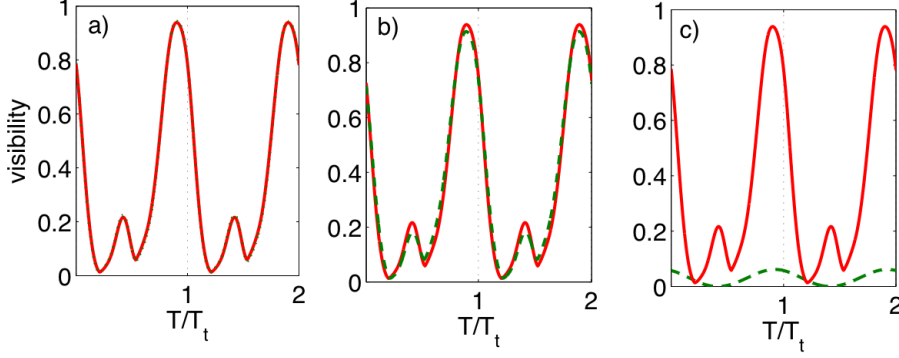


Figure 5: The plots show the interference contrast vs. pulse delay in units of the Talbot time for gold clusters with a mass of *a*) 10^6 amu, *b*) 10^8 amu and *c*) 10^9 amu. The red line results from calculations including Mie theory to zeroth order and the dashed green line results from calculations including Mie theory to 10th order. The validity of the point-particle approximation breaks down beyond 10^8 amu, where the cluster diameter approaches the grating period.

The fringe visibility as a function of T/T_t is shown in figure 6, where material characteristics of large gold clusters are assumed (i.e. $\beta = 24, 31\epsilon_0$). The laser power in this simulation is set for all three gratings so that $n_0^{(j)} = 8$, which corresponds to an average ionization probability at an antinode of 99.96%. The graph allows to compare the classical visibility (green line) with the full quantum mechanical contrast (red line) and the sinusoidal visibility (blue line).

The fringe pattern can unambiguously be assigned to the quantum wave nature of the particles if maximum visibility reappears periodically after integer multiples of T_t . The classical contrast does not show this behavior: it decays rapidly as the pulse delay increases and does not rise again to values comparable to the quantum visibility.

Comparing the sinusoidal interference visibility and the full quantum

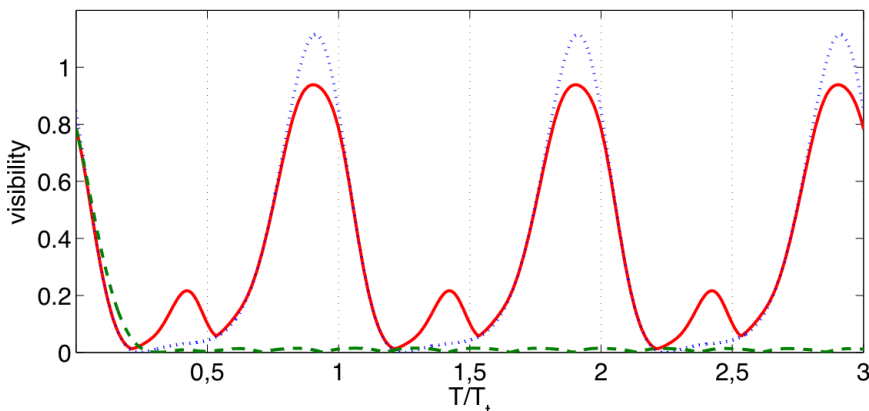


Figure 6: The plot shows the classical fringe visibility (dashed green line), the sinusoidal quantum visibility (solid red line) and the full quantum visibility (dotted blue line). The simulation was done for large gold clusters.

visibility in figure 6 may suggest that the difference between the two is negligibly small. This, however, is not always the case: as the laser power is increased (and thus simultaneously the mean photon absorption number) higher Talbot orders give rise to visibility peaks at fractions of the integer Talbot times. This is demonstrated in figure 7 which simulates the interference contrast of a gold cluster OTIMA-experiment with the power of all three gratings set so that $n_0^{(j)} = 21$. It is in fact feasible to achieve such high photon absorption numbers in the OTIMA-TLI with the lasers running at full power and a sufficiently large photon absorption cross section of the clusters¹⁰.

For this reason only the full quantum mechanical visibility is taken into account¹¹ in the following.

The phase grating contribution of G2 gives rise to the fact that in figure 6 the highest interference contrast is not obtained at pulse delays equal to integer multiples of T_t but rather somewhat earlier. This shift depends on the polarizability of the probed particle. Different cluster materials are compared

¹⁰In this case the value $n_0^{(j)} = 21$ was obtained under the assumption of cluster mass of 50.000 amu and a pulse power of 4 mJ.

¹¹*Full* refers to the calculation of up to the 10th Fourier component of the signal. Calculating higher order Fourier components does not change the signal notably.

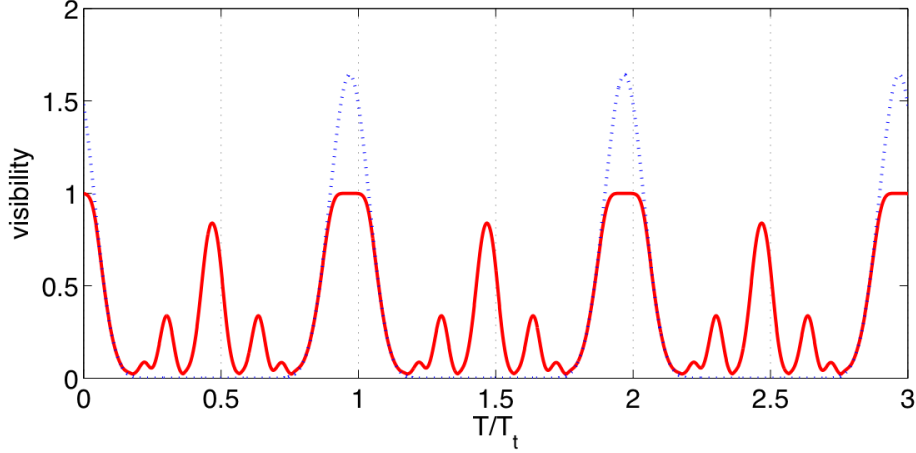


Figure 7: Visibility simulation of a gold cluster experiment with high laser power ($n_0^{(j)} = 21$). The plot shows the full quantum contrast (solid red line) as well as the sinusoidal quantum visibility (dashed blue line). The full quantum calculation exhibits visibility peaks due to higher Talbot orders which are absent in the sinusoidal visibility.

in figure 8 which shows the contrast for gold ($\beta = 24, 31 \varepsilon_0$), silver ($\beta = 231, 12 \varepsilon_0$) and cesium ($\beta = -33, 75 \varepsilon_0$). On silver clusters G2 acts almost as a pure absorptive mask since it has a dielectric function with a large imaginary part. Gold and cesium on the contrary have comparatively small imaginary dielectric functions and thus experience a larger phase shift in G2. The fact that cesium has a negative β identifies it as a low field seeker at 157 nm.

So far we have assumed equal laser power in all three standing waves. Experimentally we, however, have the freedom of adjusting the laser power of each grating individually. The effect of such a scaling on the interference contrast is shown in figure 9 and compared to the classical fringe visibility. The simulations were done for gold clusters and the pulse delay was set to T_t . Figure 9 a) shows the expected visibilities if the power of G1 is scaled and G2 and G3 are operated at constant power so that $n_0^{(j)} = 8$. For symmetry reasons we obtain the same result when the power of G3 is scaled.

Figure 9 b) shows results of the same calculation where the power of G2 is scaled and G1 and G3 are operated at $n_0^{(j)} = 8$. The simulation shows that the first and third grating act as classical masks, while at the center

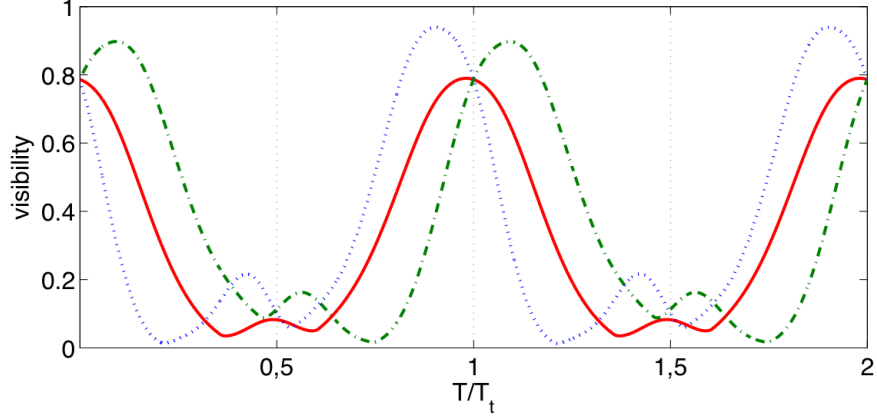


Figure 8: Simulated interference visibility as function of the pulse timing for gold with $\beta = 24,31 \varepsilon_0$ (solid red line), silver with $\beta = 231,12 \varepsilon_0$ (dashed blue line) and cesium with $\beta = -33,75 \varepsilon_0$ (dashed-dotted green line). The shift from the integer Talbot times arises from the phase contribution in G2 and depends on the particle's polarizabilities.

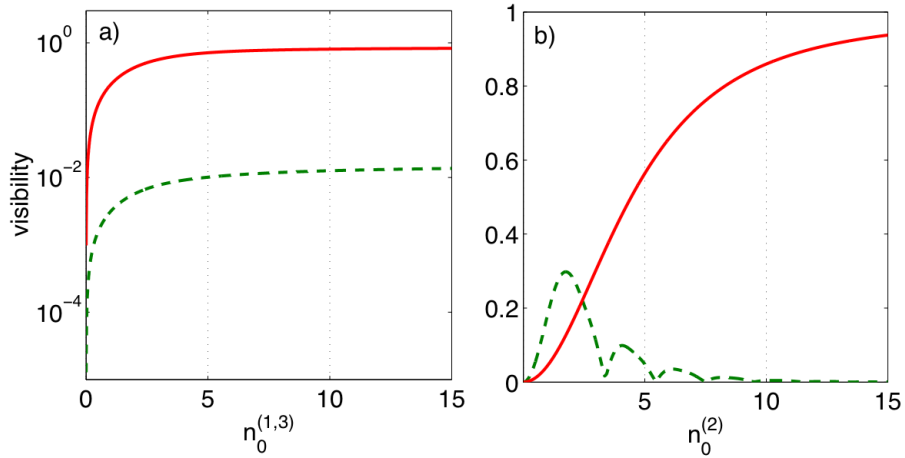


Figure 9: Simulated classic (green dashed line) and quantum visibility (red solid line) as a function of the mean number of photons absorbed at an antinode of grating 1 and 3 (panel a) and at grating 2 (panel b). In both cases the remaining gratings are operated constantly at $n_0^{(j)} = 8$.

grating matter wave diffraction takes place. This can be seen in the fact that the expected classical and quantum visibilities differ in plot *a*) only by a normalizing factor. In plot *b*) however the green and red lines differ also qualitatively. Evidence for the wave nature of the probed clusters is thus found as soon as the visibility approaches its maximum value for high laser powers and does not vanish like the classical visibility in figure 9 *b*).

This result may suggest to increase the laser power in favor of higher visibility. Yet, increasing the laser power also decreases the effective grating slit width and thus results in lower signal intensity. Whether this can be accepted depends on the brilliance of the particle source but either way a compromise between visibility and transmission is necessary.

Figure 10 shows the quantum visibility and the transmission as function of laser power in G1/G3 (plot *a*) and G2 (plot *b*) where the assumptions are the same as in the previous simulation.

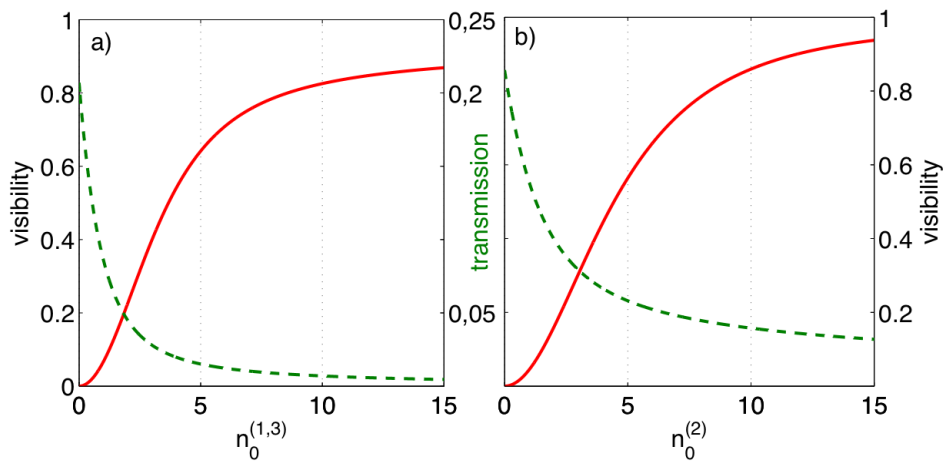


Figure 10: Simulated transmission (green dashed line) and quantum visibility (red solid line) as a function of the mean number of photons absorbed at an antinode of grating 1 and 3 (panel *a*) and at grating 2 (panel *b*). In both cases the remaining gratings are operated constantly at $n_0^{(j)} = 8$.

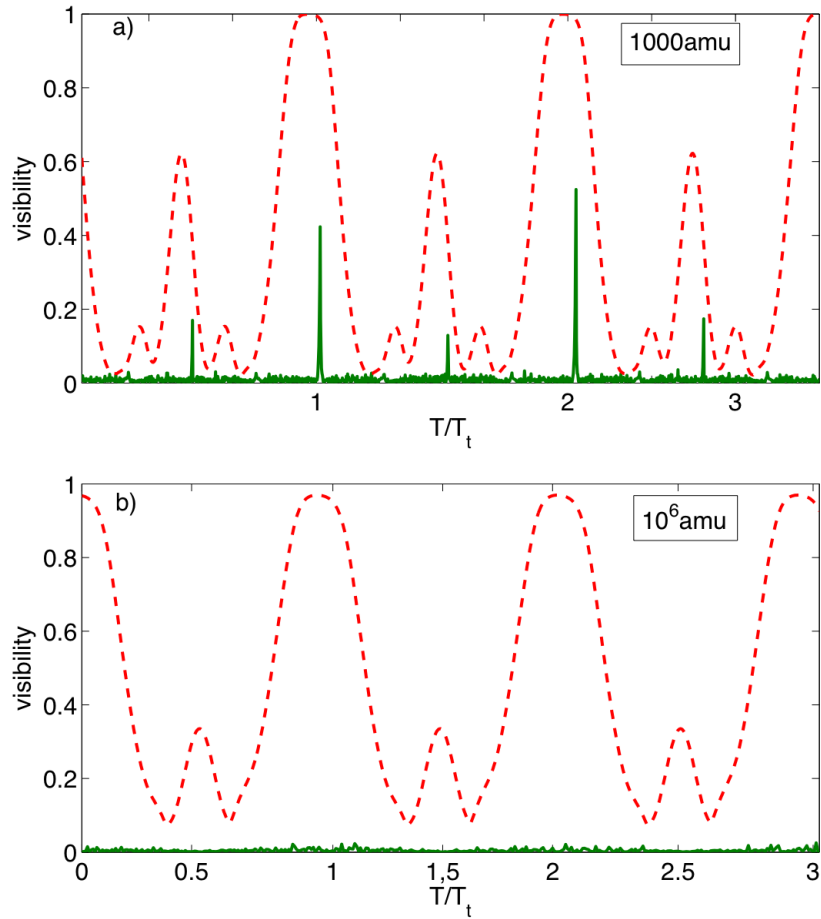


Figure 11: Comparison of the expected visibility of an OTIMA-interference experiment (red dashed line) and a conventional TLI experiment with material gratings (green solid line). The simulations assume the characteristics of gold clusters with a mass of 1000 amu (panel *a*) and 10^6 amu (panel *b*) and demonstrate the advantages of a time-domain laser grating setup when it comes to high mass interferometry.

5.8 Comparison to the conventional TLI

Molecular interferometers with material gratings have existed for several years by now [15] [26] [59]. When it comes to revealing the de Broglie wave nature of increasingly large particles they suffer from a fundamental disadvantage: the finite grating thickness gives rise to interactions between the particles and the grating material [55]. For short distances between the particles and the grating surface this is mainly described by van der Waals forces while for larger distances retardation effects due to e.g. the Casimir-Polder potential have to be taken into account. Either case results in a phase shift depending on size, velocity and position of the particles passing through the grating which, in turn, requires stricter velocity selections and thus necessitates longer averaging times. This leads to a reduction of interference contrast, the extent of which can be seen in figures 11 *a)* and *b)*: here the expected interference contrast for gold clusters in an OTIMA-interference experiment (red solid line) and in a material grating interference experiment (green dashed line) with a mass of 1000 amu and 10^6 amu are compared. Already for particles of 1000 amu the contrast in the conventional setup is reduced by 50% with respect to the expected OTIMA-visibility (see panel *a)*). At 10^6 amu however interference is not observable in a material grating interferometer, whereas the OTIMA-TLI is in principle still capable of producing high contrast interferograms (see panel *b)*).

6 Experimental setup

6.1 Setup overview

This section gives an overview of the OTIMA-TLI setup. Figures 12, 13 and 14 show the CAD layout and recent photographs of the experiment.

Foundation of the setup is an optical table, which floats on air pressurized pillars¹². On this table the vacuum chamber system is fixed on aluminum legs. There are essentially two large vacuum chambers, namely the source chamber and the chamber accommodating the actual interferometer (main chamber). The two are connected with a two-step differential pumping stage. An independent vacuum box system houses the VUV-laser optics.

The legs supporting the source chamber are placed on tracks so that the source can be rolled back. The table has cut-outs directly under the optics box as well as sidewise and behind the source. They serve the purpose of giving easy and quick access to the experiment. The large sidewise cut-out is additionally handy since it fits the liquid nitrogen dewar and thus allows to keep the coolant supply pipes to the source as short as possible.

The vacuum pump system includes 9 turbo molecular pumps. Two are mounted on the source chamber¹³ and one on each pumping stage¹⁴. The sealing ring between the source chamber and the first pumping stage as well as the feedthrough for adjustment of the aggregation tube length are differentially pumped by a single turbo pump¹⁵. The main chamber is evacuated by two pumps¹⁶ mounted closely to the interferometer mirror. The drift tube of the mass spectrometer is pumped by an individual turbopump¹⁷. The use of VUV-light for the laser gratings necessitates evacuation and/or nitrogen purging of the beam paths. For this reason the optics box is evacuated¹⁸ and nitrogen purged at the same time, such that a pressure

¹²*Thorlabs Inc. UltraPlus* optical table

¹³*Edwards* STP-1003

¹⁴*Pfeiffer Vacuum* HiPace 300 on stage nr.1 and *Pfeiffer Vacuum* HiPace700 on stage number two

¹⁵*Pfeiffer Vacuum* HiPace 10

¹⁶*Pfeiffer Vacuum* HiPace 700

¹⁷*Pfeiffer Vacuum* HiPace 300

¹⁸*Pfeiffer Vacuum* HiPace 300

6.1 Setup overview

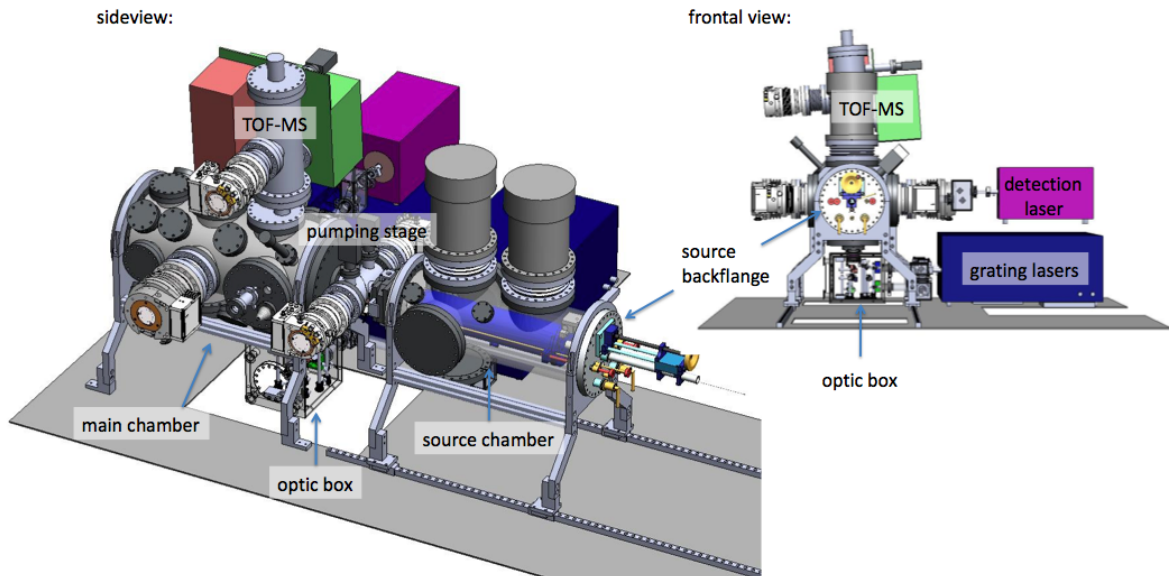


Figure 12: CAD drawing of the experimental setup in side-view perspective (left) and from the back (upper right).

of 1 mbar is maintained (see section 6.6). This is achieved by running the optics box vacuum pump at a reduced speed of 260 Hz. The source pumps run at 580 Hz and all remaining pumps at 1000 Hz. Additionally a liquid nitrogen filled container is mounted inside the main chamber which acts as a cryo pump. With this setup the pressure in the main chamber reaches about 10^{-9} mbar after a week of pumping. Additional heating of the chamber is therefore at the moment not necessary. The pressure in the source chamber during operation of the source (i.e. high gas load) lies around 10^{-3} mbar. The pressure along the particle beam path is then gradually decreased with the first ($\approx 10^{-5}$ mbar) and the second pumping stage ($\approx 10^{-7}$ mbar).

In order to keep mechanical vibrations from the interferometer mirror all pumps are mounted on vibration damping bellows. For the same reason all pre-vacuum pumps and the laser water cooling system are situated in a room next door. The interferometer mirror is mounted inside the main chamber in an aluminum holder. This part is depicted in figure 15. The VUV-mirror rests on an aluminum rim which is attached to a motorized translational

stage¹⁹. This allows to adjust the position of the mirror over a range of 1 cm and thus to set the gap between the mirror surface and the particle beam. Above the VUV-mirror an aluminum coated mirror is mounted in a 45°-angle. It reflects the fluorescent laser spots from the backside of the VUV-mirror through a window in the chamber wall. This setup allows to monitor the positions of the laser spots on the mirror which is important during alignment of the lasers. Deflection electrodes can be mounted under the mirror along the particle beam (in the current setup they are not implemented yet). The operation of absorptive laser gratings however necessitates a strong electric field to remove the ions produced in the of the standing waves. For this reason a single electrode is placed aside of the cluster beam²⁰. Usually a voltage of 300 V is applied while the experiment is running.

The particle beam is pulsed by a rotating disk chopper with a diameter of 15 cm and a thickness of 100 μm . The disk has 1 mm-long slits on orthogonal axes, distanced from the circumference by 2 mm. The particle beam is transmitted into the interferometer when a slit overlaps with the particle beam. Since there are four slits in the disk the frequency at which the particle beam is pulsed equals 4 times the rotational frequency of the disk. The disk chopper is mounted on a magneto-fluidic rotational feedthrough²¹ driven by an electric motor²² which is attached to the axis of the feedthrough with a bellow connector. This aims at reducing the impact of motor vibrations. The chopper opening provides a possibility to implement a master trigger for the experiment. This is realized by chopping not only the particle beam but simultaneously a laser beam. The light pulses are then directed onto a fast photodetector and the photodiode signal is used as a master trigger pulse for the OTIMA-experiment. The beam of the laser diode aims at a position of the disk chopper which is located about 10% less than a quarter circumference away from the highest point. This ensures that there is a delay between the master trigger pulse and the moment when the particles

¹⁹*Micos* ES-8213 VSS-VGPL VLS UHV

²⁰The generation of a well defined deflection field requires specific electrode surfaces. For the mere removal of ions, in contrast, simple copper wires are sufficient.

²¹Custom made by *Beam tech Inc.*

²²*Maxon* motor 325408

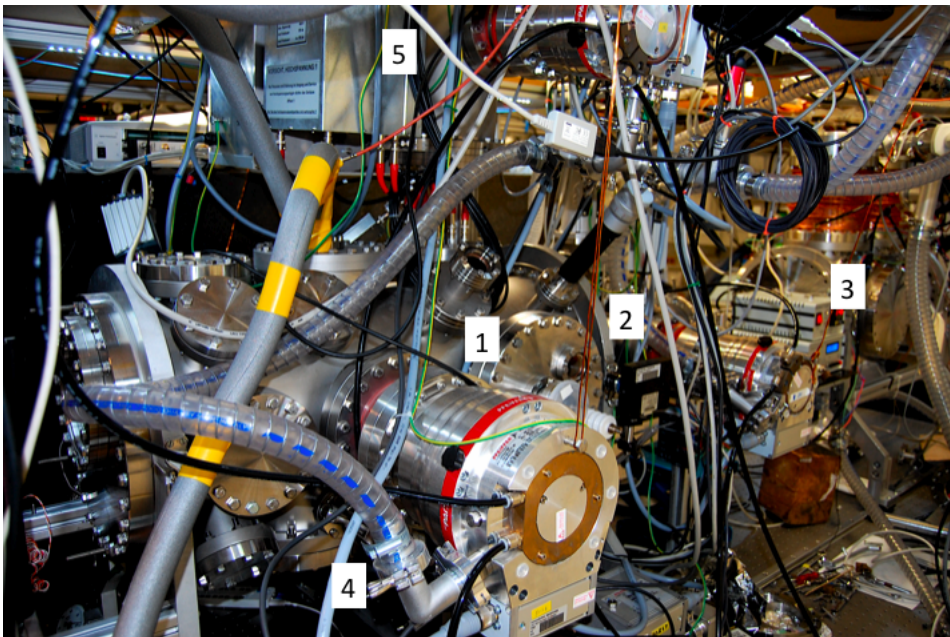


Figure 13: Photograph of the OTIMA-TLI setup. 1) main chamber, 2) differential pumping stage, 3) source chamber, 4) optics box 5) TOF mass spectrometer.

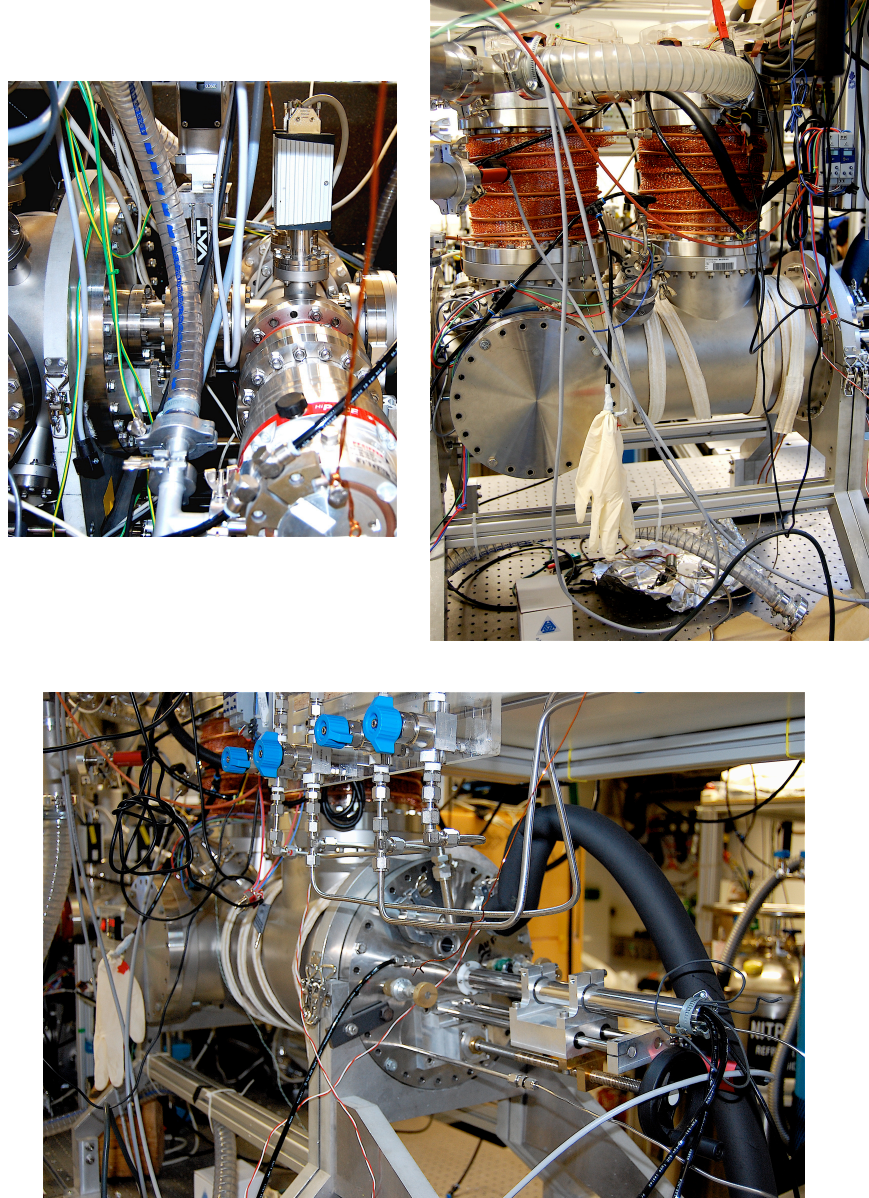


Figure 14: *upper left*: detail picture of the differential pumping stage. The main chamber flange is visible on the left side of the picture. *upper right*: sideview of the source chamber. The two turbo pumps on the top of the chamber are equipped with an external water cooling system. *center bottom*: back flange of the source chamber with several feedtroughs. The gas supply control board is shown in the top of the picture.

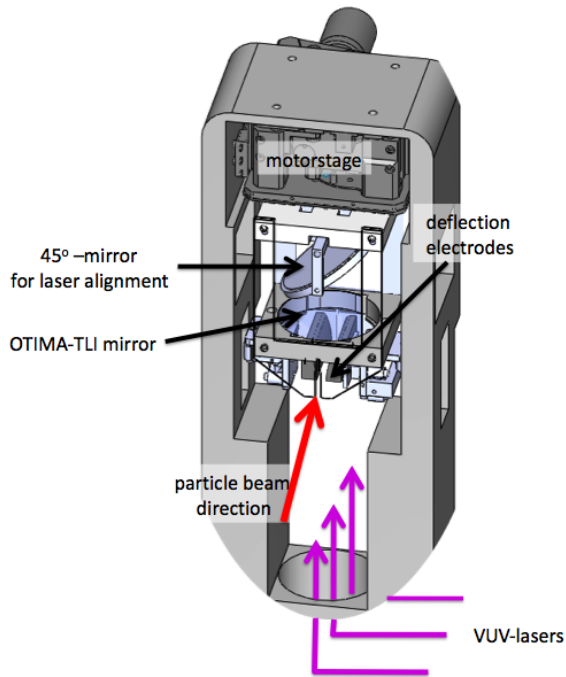


Figure 15: Drawing of the interferometer mirror assembly which is located inside the main chamber. The mirror rests on a aluminum rim attached to a motorized translational stage. In such way the gap between the particle beam and the mirror surface can be adjusted. A second mirror is attached in an 45° -angle so that the position of the laser spots can be monitored through a window in the main chamber.

are transmitted by the chopper opening. In other words: particles will be transmitted from the very same opening of the chopper that has given the master trigger pulse. The triggering is thus independent of imbalances of the disk and the influence of a possible jitter in the rotation frequency reduced. This would not be the case if the trigger laser was aimed at a point exactly 90° from the highest point of the chopper.

For the delay management two BNC delay generators²³ are employed. The first of these handles the delays for the grating lasers and the over all delay for the detection process. The delays within the detection process are set by the second pulse generator. This includes the delay for the ionization laser, the mass spectrometer opening delay and the delay for the digitizer card which processes the data from the mass spectrometer. The card²⁴ has a maximum time resolution of $8 \cdot 10^9$ samples/s. We usually operate at a reduced resolution of $1 \cdot 10^9$ samples/s because we have found this to be the best compromise between fast data acquisition and a small amount of noise. The time resolution is thus 1 ns. In the internal memory of the card $1 \cdot 10^9$

²³ BNC Model 575 Pulse/Delay generator

²⁴ Agilent technologies Acqiris CC103

samples can be stored. This memory can either be distributed over the four existing input ports or used for a single one. We have chosen the latter option, since a large input buffer speeds up the data acquisition. In practice this means that the data is saved for 1 ms and transferred to a computer in 4 ms.

6.2 Source setup

The source of the current OTIMA-TLI setup is a magnetron sputter source²⁵ which consists of a sputtering head inside a LN₂-cooled cluster aggregation tube (see figure 16). It is fixed inside a vacuum chamber and is during operation evacuated to a pressure of about 10⁻³ mbar. Since the pumps are not adapted to a high gas load, the prevention of overheating requires an external water cooling system in addition to the implemented one. Gas, high voltage and coolants are supplied via several feedthroughs in the back flange. The gas flow into the source is controlled by a system of flow controllers and valves which allows to direct Ar, He and Ne and arbitrary mixtures hereof to different outlets inside the source. Outlets are positioned behind and inside the sputtering head. The flow of LN₂ into the double walled aggregation tube is controlled by a system consisting of a temperature sensor and an electric valve. This allows to maintain a constant temperature of the drift tube walls. Inside the drift tube the position of the sputtering head can be adjusted in-situ as well as the angle of the cluster beam with respect to the beamline.

Heart of the apparatus is the sputtering head schematically depicted in figure 17. It consists of a set of water cooled permanent magnets to which the sputtering target is fixed. The magnets are situated such that their field constrains the motion of electrons to a toroidal volume close to the target surface [60]. Argon gas is then blown over the target while a high voltage is applied between the target (cathode) and the housing (ground). Since in the torus there is a high electron density, many Ar-atoms are

²⁵The source has been developed in the Haberland/Issendorff group at the University of Freiburg

6.2 Source setup

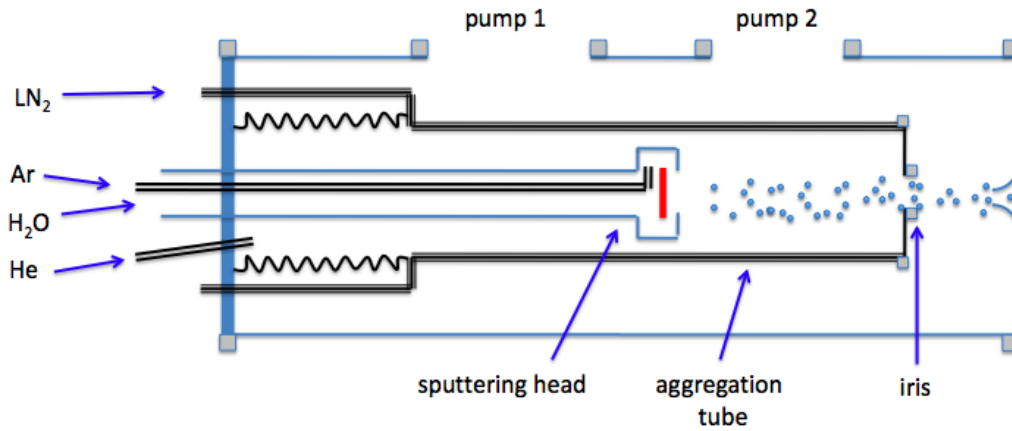


Figure 16: Schematic view of the source setup. Aggregation tube and sputtering head are situated inside a vacuum chamber. The source is supplied with coolants and gas via feedthroughs on the backside chamber flange. Iris diameter as well as the angle of the aggregation tube are adjustable in-situ. (figure adapted from [60])

ionized by electron-impact and a plasma is ignited. The high voltage now accelerates the Ar-ions towards the target surface where atoms and small clusters are ejected as the ions impinge. During this sputtering process secondary electrons emerge which are then again trapped in the field of the permanent magnet and help to maintain the plasma. In order to keep the temperature of the sputtering target and the magnets below the damage threshold, the sputtering head is water cooled from the backside. The atoms that are ejected from the sputtering head enter into the aggregation tube and are picked up by a stream of gas. This may be helium, neon or argon, depending on the desired mean velocity and size of the clusters²⁶. During the aggregation process the excess energy is picked up by the surrounding noble gas [61]. Translational cooling of the clusters is achieved by constantly keeping the walls of the aggregation tube at LN₂-temperature. Finally the clusters exit the source through a diameter-adjustable diaphragm. Due to spray charges being present during the sputtering process many

²⁶We have found that the yield of slow and small clusters is best when helium is used.

clusters are ionized and carry different amounts of positive or negative charge. Positively and negatively charged cluster are expected to represent around 2/3 of all produced clusters depending on the cluster material. Since the skimmer through which the clusters leave the source chamber is electrically grounded, a majority of the ions does not leave the source chamber. The 30% neutrals thus constitute the final cluster beam.

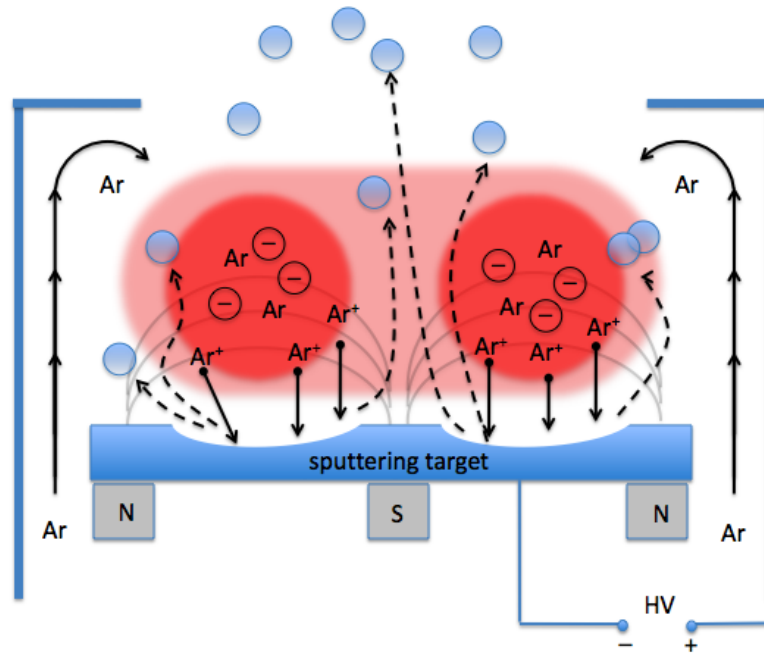


Figure 17: Schematic picture of the sputtering head. Permanent magnets (represented by the grey squares with N and S denoting the respective pole) induce a magnetic field which constrains the motion of electrons to a torus-shaped volume (red area in the picture) close to the target surface. Argon gas is introduced to the head via inlet jets and ionized by the electrons. The ions are then accelerated by a high voltage applied to the target and while impinging onto the surface remove atoms from the target. These atoms are released into the drift tube where they aggregate to clusters.

6.2.1 Source settings

The magnetron sputter source offers a wealth of parameters which can be adjusted in order to obtain the desired cluster beam characteristics.

Parameters are: position of gas-inlet, gas flow, gas mixture, length of the drift tube, sputter power and the pressure inside the aggregation tube, which can be adjusted by changing the diameter of the outlet aperture.

At this stage of the experiment we aim at a sufficiently small cluster velocity around 300 m/s, which is the most common velocity for clusters in a mass range of 4000-5000 amu (see section 6.3). We have found that these requirements are best met when helium and argon are injected both at the sputtering head. A suitable helium-to-argon flux ratio has proven to lie around 3-to-1 and the argon-flux is usually set to around 100 sccm per minute. The iris at the source exit is then adjusted such that the pressure inside the aggregation tube reaches approximately 1 mbar. Higher pressure inside the drift tube is achieved by higher He-flux or a smaller iris opening and leads to an increase in the cluster mass. Adjusting the length of the aggregation tube equally effects the mass range of produced clusters. The sputter power, which can be set at the source power supply, also has a great influence on the intensity of the beam. Since an increased sputter power shortens the lifetime of the target and increases the cluster size, it is usually set to around 40 Watts and is increased up to 150 Watts only when high brilliance of the source is needed for a short period of time.

The pressure of the source chamber also has a significant effect on the cluster velocity: reducing the pump rotation frequency from 580 Hz to 510 Hz causes a slowing of the clusters by almost 10%. Further reduction of the frequency however has the unwanted effect of less signal and larger clusters.

6.2.2 Particle beam characteristics

The particle beam is guided into the interferometer chamber via two differential pumping stages. This is necessary since a pressure gradient of 10^{-6} mbar lies between the main chamber and the source chamber. The beam line is schematically depicted in figure 19: the clusters leaving the aggregation tube pass through about 3 cm of 10^{-3} mbar vacuum. They are then fed through a beam skimmer which collimates the beam to 1 mm in diameter. The skimmer is mounted on a translation stage and can be

adjusted to the center of the beam without breaking the vacuum. Behind the skimmer the particles enter the first pumping stage where a pressure of 10^{-5} mbar is maintained. This stage is 8 cm long and it is connected to the subsequent pumping stage via a pinhole orifice with a diameter of 5 mm. For achieving higher vacuum in pumping stage 2 and in the following main chamber, additionally a vertical slit of 2 mm width is pressed against the pinhole with two springs. It is mounted on a transversally adjustable vacuum feedthrough, so that its position with respect to the orifice can be changed. After a distance of 10 cm the clusters enter the main chamber through a circular aperture. Initially both pumping stages were evacuated with two identical 300 liter/s pumps. Increasing the pumping power of the second pump to 700 liter/s has lowered the pressure in the affected stage by approximately an order of magnitude. This gave rise to a signal increase by a factor of two or three.

From all the apertures in the beam line, the skimmer and the collimation

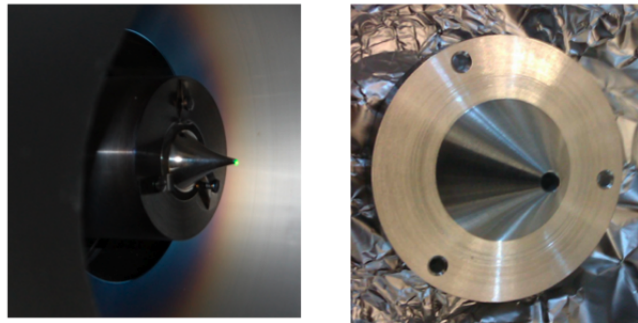


Figure 18: Left side: The commercial beam skimmer is shown mounted in the particle beam path. Right side: self-made conical skimmer.

slits in the main chamber have the most influence on the beam characteristics²⁷. Since these are the first and last elements in the beam line they define the diameter of the beam as well as its divergence. In the current setup a parabolic skimmer is used²⁸ with a base plate diameter of 2,22 cm, a

²⁷i.e. is if the chopper disk is fixed at an 'open' position which is usually done when experimenting with the source settings.

²⁸manufactured by *beam dynamics Inc.*

height of 1,90 cm and an orifice diameter of 1 mm (figure 18, left side). The parabolic shape of the skimmer serves the purpose of avoiding perturbation of the molecular stream. We have experimented with a self made skimmer which had a conus shape rather than a parabolic shape (figure 18, right side). Additionally it had a larger orifice diameter of 2 mm. The test has shown that the signal with this skimmer was higher by a factor three to four. This however came at the expense of more frequent skimmer clogging, most likely due to the capillary-formed opening. Since this makes long measurements impossible we have switched back to the beam dynamics skimmer. Unfortunately the two skimmers are lacking in similarity, and thus the test did not entitle us to say if the parabolic skimmer shape is strictly necessary.

It is, however, not only the shape of the skimmer one has to consider but also the position with respect to the source orifice. This is due to the fact that the molecular jet emitted by the source experiences a pressure decrease of several orders of magnitude when leaving the aggregation tube. This leads to a supersonic expansion of the particle cloud which is free of perturbations only in the so-called *zone of silence* [62]. This is a volume that is enclosed by supersonic shock waves. Its length x_{zos} is determined by the pressure gradient P_0/P_1 and the orifice diameter D via

$$x_{zos} = 0.67D\sqrt{\frac{P_0}{P_1}}, \quad (56)$$

where P_0 is the pressure in the chamber left by the particles and P_1 is the pressure in the chamber entered by the particles [62]. This means that for an iris-opening of $D = 2$ mm, a drift tube pressure of $P_0 = 1$ mbar and a source chamber pressure of $P_1 = 1 \cdot 10^{-3}$ mbar the zone of silence has a length of $x_{zos} = 42$ mm. In order to ensure a perturbation free propagation of the particle beam it is thus necessary to place the skimmer opening not further away than 42 mm.

As already pointed out in section 5.3 the required alignment precision increases with the divergence of the particle beam. This attaches special importance to the vertical collimation of the beam which is defined by

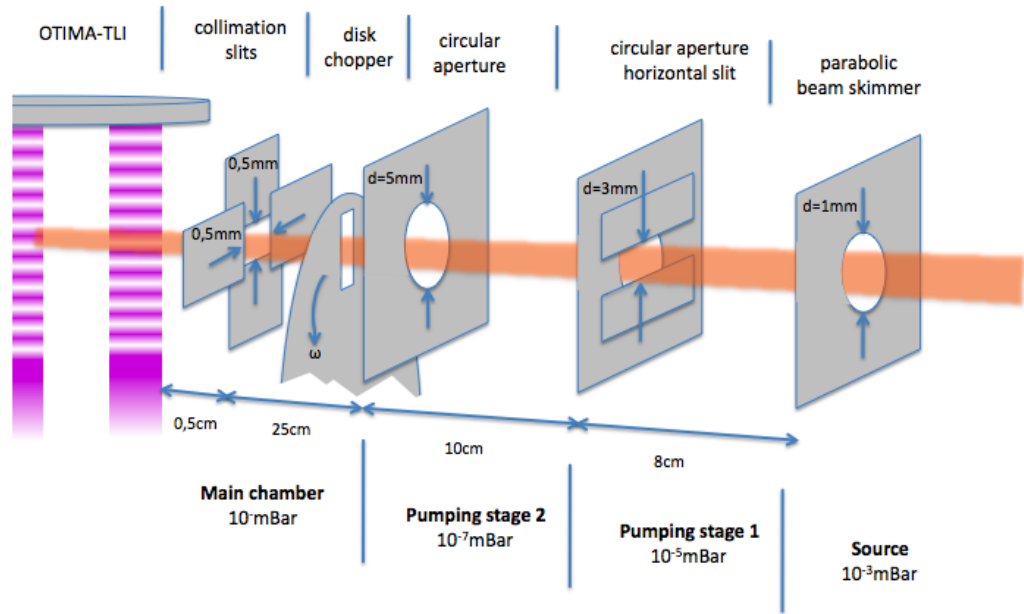


Figure 19: Collimation and guiding of the cluster beam.

the skimmer orifice diameter and the vertical collimation slit in the main chamber. For the current beam line setup with a vertical collimation slit width of $500\ \mu\text{m}$ in the main chamber, a skimmer opening of $1\ \text{mm}$ and a total length of $43\ \text{cm}$ we arrive at a beam divergence²⁹ of $1,74\ \text{mrad}$. This value has to be seen as the largest divergence angle geometrically possible in the above specified two aperture system. The true divergence is smaller if the iris diameter is set to equal the skimmer orifice diameter. Usually however the opening diameter of the iris is larger than the opening diameter of the skimmer. In this case the above given value for the divergence is correct. For an estimate how many grating slits are illuminated by the beam one has to know the distance from the point P where the two most diverging rays cross the beam axis to the position where the first grating pulse appears. From geometric considerations and the intercept theorem it follows that P is

²⁹The divergence angel throughout this work is defined as the largest possible angle between a particle trajectory and the beam axis in contrast to twice this angle which can be found in the literature.

14,33 cm behind the collimation slits (see figure 19). If the collimation slits are placed 0,5 cm behind the first grating the beam illuminates a maximum of 6500 grating slits.

6.3 Velocity selection

All particles need to interact with all three lasers. This could be ensured by preparing a continuous particle beam in which particles are travelling at a fixed velocity. Realistic cluster beams, however, can have a large velocity spread and slow particles interacting with all three lasers could be overtaken by fast clusters which missed the first pulse. For this reason the particle beam in our current setup is pulsed. This allows to influence the width of the velocity distribution in the particle clouds by adjusting both the chopper parameters and the delay of the detection laser accordingly. It has to be emphasized though that this velocity selection serves a different purpose than in a material grating TLI, where the visibility is reduced if particles with a different velocity and thus different de Broglie wavelengths contribute to the interference pattern. In the time-domain TLI this does not alter the visibility because all particles with the same mass produce the same interference pattern at a certain time. The velocity selection effects the visibility only in the sense that it has to be sufficiently strict in order to prevent particles from overtaking one another and avoiding a grating in this way. It thus needs to sort out particles with a velocity larger than

$$v_{max} = \frac{d_{12} + b + d_{23}}{2T_t} \quad (57)$$

and smaller than

$$v_{min} = \frac{d_{12} - b + d_{23}}{2T_t}, \quad (58)$$

where d_{12} and d_{23} are the distances between lasers 1 and 2 and lasers 2 and 3 respectively and referring to the beam centers. The width of the laser gratings along the particle flight direction is denoted with b . For $d_{12} = d_{23} = z_l$ we arrive at $\Delta v/v = (v_{max} - v_{min})/v = b/z_l$, where v is

the mean velocity in the particle beam. The required velocity selection is thus independent of the particle mass and depends only on the laser beam width and spacing between the gratings. These parameters are usually kept constant at $z = 1,6$ cm and $b = 1$ cm. They are roughly predetermined by the diameter of the interferometer mirror, the positions of the mirror mounts in the laser beam lines and of course the characteristics of the VUV-laser beams.

This provides a loose upper bound for the necessary velocity selection of $\Delta v/v = 60\%$ and illustrates that the velocity selection in the OTIMA-TLI needn't be particularly strict. Yet, if the velocity spread in the particle cloud is wider, the particle density in the cloud is smaller and less clusters are exposed to the lasers. Narrowing the velocity distribution beyond the requirements for interferometry is thus also a step towards higher signal intensity.

The parameters that determine the width of the velocity distribution are, on the one hand, the chopper characteristics including the chopper slit width, the width of the horizontal collimation slit at the entrance to the interferometer, the chopper disk diameter and the rotation frequency. On the other hand, the velocity distribution is shaped by the ionization volume in the ion source of the TOF-MS since the length of this volume is the distance over which the velocities are averaged prior to detection of the particles.

Let now the disk chopper have radius of r_{ch} and four slits with a width of W_{ch} located in 90° steps along the circumference. The horizontal collimation slit³⁰ at the entrance of the interferometer has a width of W_H and is required to be wider than W_{ch} . The period of time t_{ch} in which particles are transmitted by the chopper is thus

$$t_{ch} = \frac{W_H + W_{ch}}{2\pi r_{ch} \nu_{ch}}, \quad (59)$$

where ν_{ch} is the rotation frequency of the chopper disk.

If it is now further assumed that the ionization laser in the ion source

³⁰Since this notation often gives rise to confusion: *horizontal* refers to the fact that it constrains the beam in the *horizontal* plane. The slit edges are thus vertically oriented in space.

6.3 Velocity selection

of the TOF-MS has a width of b_{ion} along the particle beam direction the particle velocities in the beam range over $\Delta v = v_{max} - v_{min}$ with

$$\Delta v = \frac{s + b_{ion}}{t - t_{ch}} - \frac{s - b_{ion}}{t}, \quad (60)$$

where t is the delay of the ionization pulse after the chopper opening and s the distance from chopper to the center of the ionization beam. It is usually convenient to express the width of the velocity distribution in terms of the velocity spread $\Delta v/v$:

$$\frac{\Delta v}{v} = \frac{2bt + t_{ch}(s - b)}{s(t - t_{ch})}. \quad (61)$$

The velocity spread thus depends on a ratio between the time-of-flight and the opening time of the chopper and therefore scales with the mean particle velocity. Since the mean particle velocity is chosen such that the particles reach from one grating to another in the Talbot time and the gratings are at fixed positions regardless of the particle mass, the time-of-flight t is proportional to the mass:

$$t = \frac{s}{z_l} \frac{\lambda_{VUV}^2}{4h} \cdot m, \quad (62)$$

where h is the Planck's constant and z_l the distance between two laser gratings. For larger masses $\Delta v/v$ thus becomes smaller if the chopping parameters remain unaltered. We can now insert the characteristics of the current setup ($r_{ch} = 7,5$ cm, $\nu_{ch} = 50$ Hz, $s = 0,111$ m, $s_{ion} = 0,5$ cm, $W_H = 500$ μ m) and a realistic ionization delay of $t = 0,412$ ms. These values are taken from an experiment with 50-atom niobium clusters propagating at a mean velocity of $v = 270$ m/s. In this case equation (60) yields $\Delta v = 36,65$ m/s corresponding to a velocity spread of $\Delta v/v = 13,6\%$. This is well below the limits imposed by (57) and (58). With the experiment set up for a particle mass of 40.000 amu and the same chopper parameters we arrive at $\Delta v/v = 5,3\%$. Nevertheless one has the freedom to make the velocity distribution less or more stringent, by either adjusting the collimation of the ionization laser beam or the opening time of the disk chopper.

It has to be emphasized that the above calculated results do not refer to the width of a velocity distribution in the sense of the full width at half maximum (which would be smaller), since neither the initial velocity distribution nor a realistic chopper opening function enter the calculation. The results merely intend to give a rough estimate of the velocity spread in the particle clouds. A more realistic experimental situation is simulated in figure 20. The simulation was carried out under the assumption that the velocity distribution prior to passing the chopper equals the Boltzmann velocity distribution of an ideal gas, where the most probable velocity is the mean cluster velocity that we have measured. The plot shows this velocity

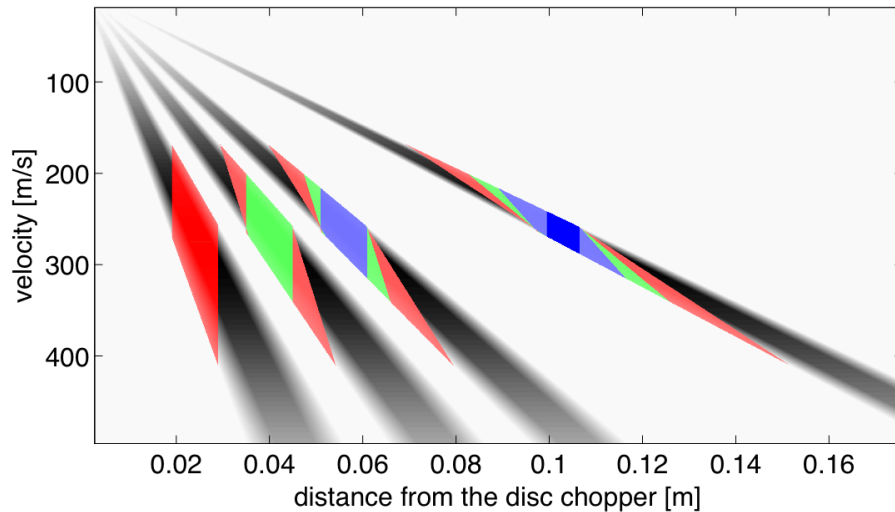


Figure 20: The velocity distribution (gray shaded areas) is shown at four different points behind the beam chopper, where the initial velocity distribution is assumed to be the Boltzmann distribution of an ideal gas. The figure shows in red, green, light blue and dark blue the areas of the particle cloud that are hit by the first, second, third and ionization laser respectively.

distribution at the positions of the three grating lasers and the ionization laser (in this order from left to right) as shaded gray areas. The fraction of particles illuminated by the first, second and third grating are visualized as red, green and light blue areas respectively. The part of the velocity distribution which

is eventually detected is shown as the darker blue square. Such simulations allow to tune the different delays with respect to one another and thus to optimize the efficiency of the experiment. The times that are finally set in the experiment may, however, differ from the results of these calculations since the shape of the initial velocity distribution also strongly depends on the source parameters.

Figure 21 shows the velocity distribution within a beam of niobium clusters versus the time of detection. In the plot the intensity is visualized by colors where red is the highest and blue the lowest (zero) intensity. Experimentally this measurement was realized by increasing the ionization delay in steps of $5\ \mu\text{s}$ from 2,258 ms to 2,433 ms. The time-axis was then transformed into a velocity-axis with the knowledge of the distance between chopper disk and ion source of the TOF-MS. Similar to how this is done for the mass spectra in section 6.14, multiply charged ions have been removed from the spectra. Figure 21 thus displays solely the velocity distribution of the singly charged ions. We neglect the multiply charged ions due to the fact that they are too heavy to be interesting for the OTIMA-experiment at the moment.

6.4 TOF mass spectrometer

The detection and data acquisition system consists of a single photon laser ionization stage (F_2 , 157 nm), a reflectron time-of-flight mass spectrometer and an analog-to-digital converter card. The data is then recorded and processed by the *MOPS* software, developed in our group to meet the requirements of the experiment. The mass spectrometer is a UHV compatible *Kaesdorf* RFT50 reflectron time-of-flight mass spectrometer which is optimized for high mass particles ($m > 100.000\ \text{amu}$). It features a two-stage Wiley-McLaren ion source [63]. It is advantageous to utilize a detection laser similar to the grating lasers since high single photon ionization efficiency at 157 nm is required for particles probed in the OTIMA-TLI anyway. The drift tube of the RFT50 has a length of 1 m and is folded with a two-stage ion mirror. At the end of the drift tube the particles are post-accelerated in a 20 kV electric field towards a three layer multi channel

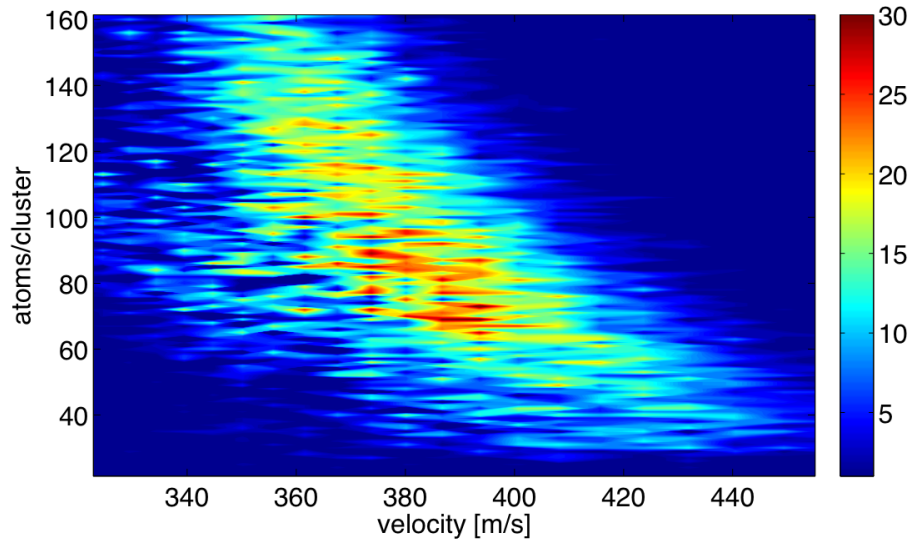


Figure 21: Velocity distribution in a beam of vanadium clusters, where the intensity of the signal is visualized by the colors. The plot shows only the singly charged ions. In this experiment the source settings resulted in a mean particle velocity of around 390 m/s for the vanadium-70 cluster.

plate detector disk (MCP) of 40 mm diameter. The detector assembly in the RFT50 offers high detection efficiency of heavy particles, even for small signal intensities. The RFT50 is specified by the manufacturer to have a time resolution $T/\Delta T = 10.000$.

6.5 VUV-Laser System

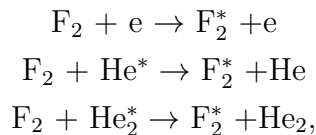
VUV-lasers have received a lot of attention in past years: On the one hand, industrial applications such as photolithography and micro-machining benefit from short wavelength, allowing to form structures with sub-100 nm resolution [64]. On the other hand, the capability of reaching high pulse powers up to a few MW makes VUV-lasers potential tools of material processing [65] as well as surgical applications [66]. However, the strong absorption of VUV-photons in most materials makes the handling of

VUV-light challenging³¹, which means that beam guiding of VUV-light requires either nitrogen purging and/or evacuation of the beam path.

In the current OTIMA-TLI setup four 157 nm molecular fluorine lasers³² are used. They generate pulses with a maximum power of 4 mJ at a repetition rate of up to 200 Hz. The active medium in the lasers is a 1000 to 1 mixture of helium and fluorine reacting to a meta stable excited state F_2^* . This state decays to less energetic bound states³³.

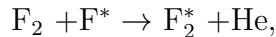
There are three possible processes which lead to excitation of the $F_2^*(D')$ state [68]:

a) Excitation by electron impact and direct energy transfer:



where an asterisk denotes excited states.

b) Excitation by neutral collisions:



where F^* stands for an excited atomic state lying energetically below F_2^* .

c) Excitation by three body collisions:



Details on the kinetics of these reactions are depicted in figure 22 a). Alongside of the $F_2^*(D')$ state-population there are several other excited states which fluorine atoms can populate. These states however rapidly decay to lower energetic excited states, giving rise to the weakly coherent emission at 600 to 800 nm accompanying the VUV-emission [67].

The laser transition responsible for the VUV-emission has a lifetime of a

³¹The absorption coefficient of 157 nm photons in oxygen is around $200 \text{ cm}^{-1}/\text{atm}$ [67]. VUV-light does therefore not penetrate air deeper than a few μm .

³²For each of the gratings a *GAM EX50* is employed and for the detection a *Coherent ExciStar XS*

³³By convention lasers with such an active medium are called *excimer* lasers (from *excited* and *dimer*) although this expression in principle only refers to light sources where lasing occurs due to relaxation from a bound dimer state to an unbound atomic state [67].

few nanoseconds which in combination of a large bandwidth and a short wavelength results in a small stimulated emission cross section. Additionally the population of the desired excited state has to compete with other fast processes (collisions, spontaneous decay) necessitating pump power densities in the order of MW/cm^3 . This is the reason why excimer lasers nearly always operate in a pulsed mode [65].

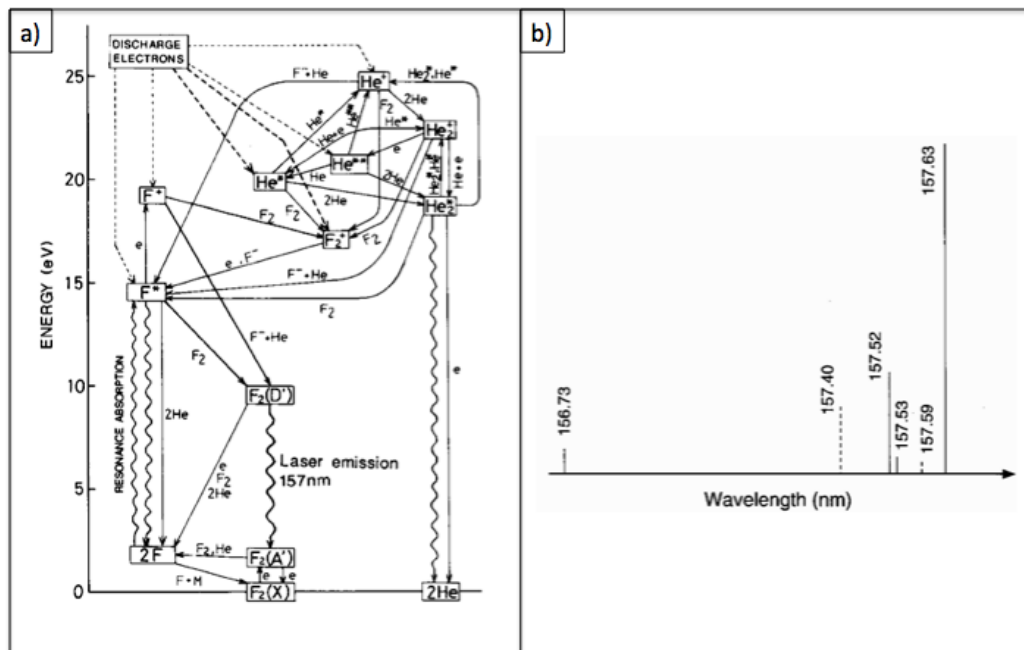


Figure 22: a) Level scheme of a discharge pumped molecular $\text{F}_2\text{-He}$ VUV-laser (figure taken from [68]). b) Spectrum of a gas discharge pumped molecular fluorine laser. Solid lines were measured with a 1000 to 1 mixture of helium and fluorine. Dashed lines occur in the spectrum when Neon is added to the gas (figure taken from [69]).

The output spectrum of a gas discharge pumped fluorine laser (as shown in figure 22 b)) exhibits two main lasing lines at 157.63 nm and 157.52 nm, where the intensity of the latter is around four times lower [69]. The linewidth of the 157.63 nm-line is estimated to lie between 0.62 pm [69] and 0.92 pm [70] full width at half maximum corresponding to a longitudinal

6.6 Beam guiding

coherence length between 2,195 cm and 1,431 cm.

6.6 Beam guiding

The optics used to guide the lasers into the interferometer chamber are dielectric calcium fluoride multilayer mirrors specified to reflect 96% intensity of a 157 nm-beam incident at 45° . They are polished on one side only. Each beam path consists of four mirrors, two of which are mounted on piezo driven kinematic mounts³⁴. The beams are focussed by plano-convex calcium fluoride lenses to a point approximately 10 cm behind the interferometer mirror. In order to monitor the laser power without venting the beam lines,

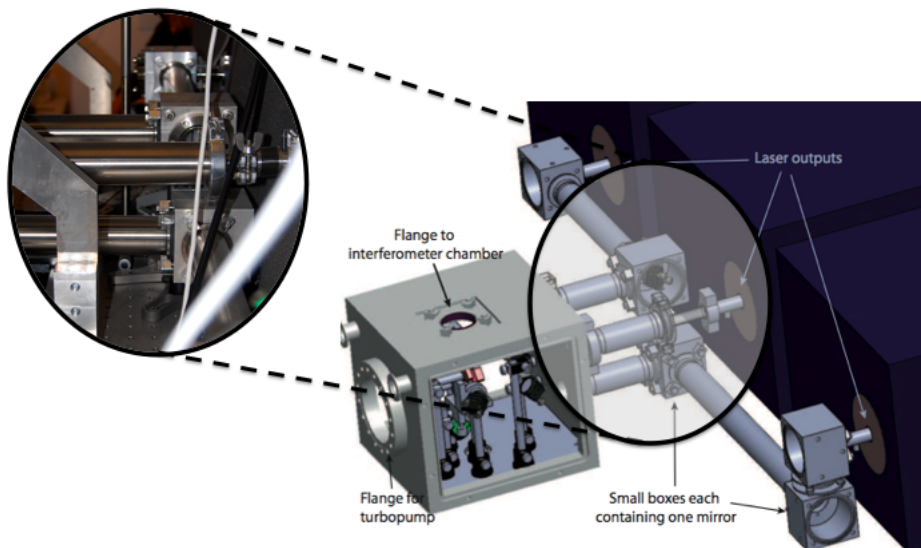


Figure 23: Picture of the laser beam lines and the optics box (*parts of the picture taken from [71]*)

the sensor chip of a piezo electric laser power meter³⁵ was freed from its housing and mounted on a mechanical vacuum feedthrough. Its position can be changed so that the chip can measure the power of either one of the three

³⁴ *Newport* Agilis series M050M

³⁵ *Ophir* Chip PN-25

grating lasers. The chip produces a voltage proportional to the laser energy and it has been calibrated to the reference of an unmodified power meter before being mounted inside the optics box.

All components of the optics box have to be VUV-compatible, which requires no material or coating inside the beam path to contain or evaporate substances that absorb 157 nm radiation. Otherwise the evaporated particles will settle on surfaces and eventually leave burn marks on the optics which effects the efficiency of the mirrors and lenses. We have found that one can clear the optics from burned deposits by running the lasers while having the beam line purged with nitrogen. This supposedly desorbs the deposited layer of burned particles. It is reported in the literature that adding oxygen in small amounts to the purge gas both reduces the buildup speed and increases the desorption of deposited layers [72] [73]. The VUV-beam paths are therefore evacuated to 10^{-6} mbar when the experiment is idling and during operation purged with nitrogen at 1 mbar during laser operation. This combination of purging and evacuation strongly lengthens the lifetime of the optical elements. We have further reduced the contamination of the vacuum by only allowing blank metal surfaces inside the chamber. This required to strip the black anodized covering off the optical mounts³⁶ and to ensure that no lubricants or other organic compounds are present in the chamber. We expect the kinematic mounts to be VUV-compatible since they are specified to be vacuum compatible up to 10^{-6} mbar.

Although these measures have reduced the contamination rate of the optics in the optics box as well as in the main chamber they do not prevent contamination entirely. For this reason oxygen cleaning of the surfaces will be tried in the near future.

6.7 Interferometer mirror

The interferometer mirror is a dielectrically coated CaF_2 disk with 5 cm diameter, 1 cm thickness and an opaque backside³⁷. It is specified to have

³⁶We have used sodium hydroxide solution for this purpose.

³⁷Custom made by *Jenoptik AG*

a reflectivity of 98% for 157 nm radiation (incident at a right angle) and a surface flatness of 0,2 nm RMS. In order to avoid any tension or stress on the surface, the mirror rests in an aluminum holder without being clamped or bolted to its base.

Sufficient mirror flatness is important since bumps or plateaus in the surface cause a shifting of the standing waves. Yet, a perfectly flat mirror is not required: firstly, surface roughness can be accepted if the height changes of the surface appear on a scale smaller than the transversal coherence length of the grating laser. This is due to the fact that the photons in the laser beam are delocalized over this distance and therefore average over possible surface irregularities. Secondly, we can neglect roughness that appears on a scale much larger than the length of the ionization volume in the TOF-MS, because this is the upper bound to the distance particles fly during a grating pulse. We find an absolute value for this criterion by assuming that the transversal coherence length of the grating lasers is around $200 \mu\text{m}$ (see chapter 6.9) and the detection laser is horizontally collimated to 0,5 cm.

In order to estimate the amount of contrast reduction caused by a certain mirror roughness we consider equation (72) (see section 6.11) and assume that half of G2 is shifted by $\Phi_2 = \Delta s$ while G1 and G3 are unshifted ($\Phi_0 = 0$). If particles are subjected to the unshifted part of G2, the interference pattern will be in-phase with G3. If the particles are subjected to the shifted part of G2 the interference fringes will be shifted by $\Phi_{\Delta s} = 2\pi(-2\Delta s)/d$. This means that the fringe pattern f is the superposition

$$f(x) = 1 + \frac{1}{2}[\sin(x) + \sin(x + \Phi_{\Delta s})], \quad (63)$$

where for sake of simplicity the signal is assumed to be sinusoidal. Inserting a shift of $\Phi_{\Delta s} = d/10$ in (63) already reduces the visibility by 20%. Even if this effect is weaker for a shift of G1 and G3, the example demonstrates the importance of a flat interferometer mirror and the relevance of surface irregularities even smaller than 10 nm. We have thus taken a closer look at the mirror surface with an atomic force microscope (AFM). Results of this measurement are shown in figure 24.

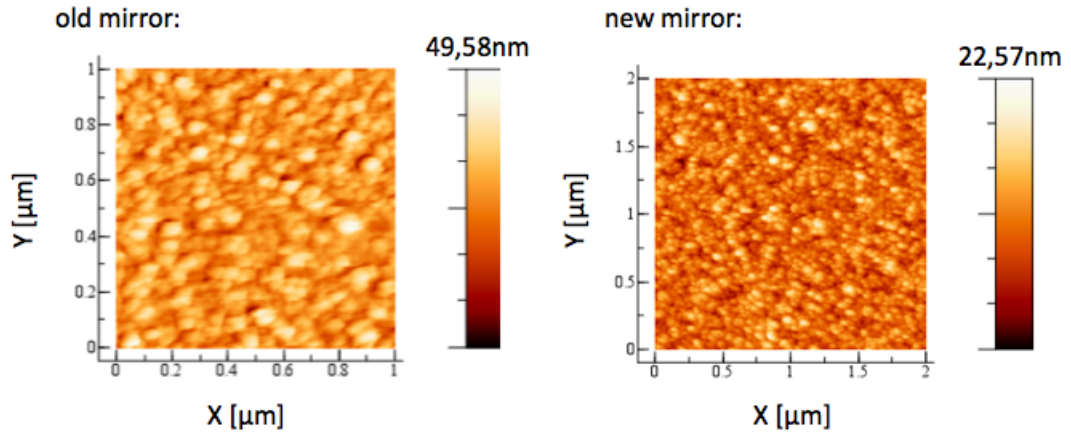


Figure 24: Air AFM images of the interferometer mirror surface. Left side shows the image of a mirror that was used for several weeks in the OTIMA-TLI. Right side shows the surface on a freshly unpacked mirror.

The measurement has shown that the surface of the mirror becomes more irregular during operation and being exposed to the background gas in the main chamber. This is likewise due to adsorption of organic-molecules on the surface. Since the AFM can only scan over an area of few μm^2 this result is not necessarily representative for the entire surface.

The AFM investigation however, albeit giving an impression of the surface quality, does not give any insight in the optical properties of the mirror since at a dielectric mirror the reflection does not only take place at the surface but at every subsequent layer. For this reason the mirror has been sent to *Laseroptik GmbH Germany* to be investigated in a white light interferometer (WLI). The recorded surface map is shown in figure 25.

The WLI-measurement shows that the mirror surface is mostly homogenous, but exhibits two or three longish plateaus (red areas in figure 25) with a height of up to 10 nm. We do not attach to much importance to these plateaus concerning visibility reducing shifts within the standing wave, since they seem to have a rather shallow slope. The investigation however has taught us that the gratings may be shifted to one another *in toto* and that the interference pattern may exhibit a certain shift. In terms of a mass

6.7 Interferometer mirror

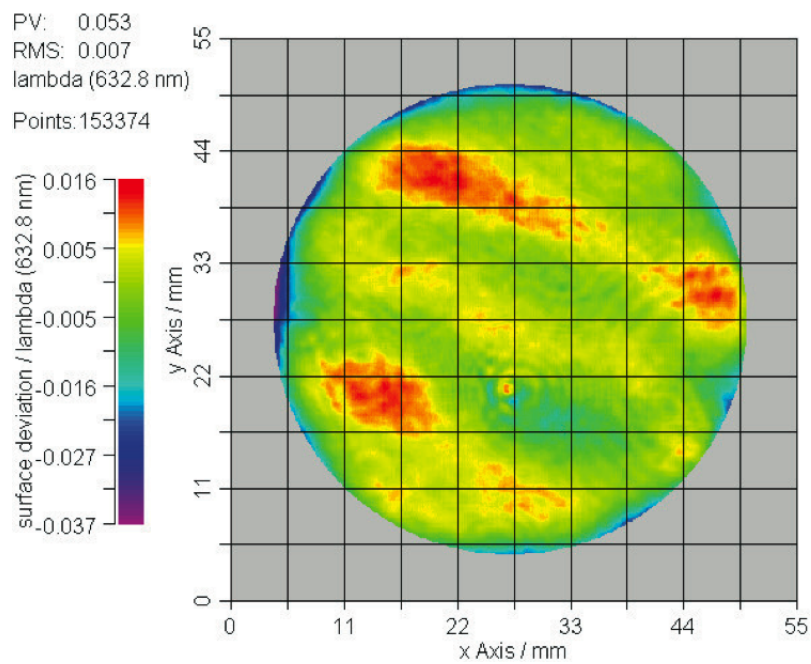


Figure 25: Surface map of the interferometer mirror recorded with a white light interferometer (image courtesy of *Laseroptik GmbH Germany*).

scan this means that the modulation in the transmission curve may appear at a slightly different position than expected.

6.8 Measurement of the longitudinal coherence length

The longitudinal coherence length of the VUV-lasers determines the distance from the mirror in which the standing-wave laser gratings have a high visibility. The distance which particles fall down in the earth's gravitational field within twice the Talbot time depends quadratically on the mass of the particles. Therefore the coherence length of the laser puts a strong mass limit to the observation of OTIMA-interference.

It is thus important to measure the coherence length of the VUV-lasers and compare the result with the literature [70] [69]. A common way to measure the coherence length of a light source is by the use of an interferometer [74] [75] [76]. The interference contrast will decay exponentially with increasing path length difference between two longitudinally separated partial waves. The coherence length is then defined as the path length difference at which the contrast has reduced to $1/e$ times the highest value.

Our measurement was done in a Fabry-Perot interferometer: two mirrors were mounted in the beamline, one of which was fixed on a linear translation stage for adjustability of the cavity length. A digital caliper mounted to the mirror posts allowed to measure the mirror distance with approximately $10\ \mu\text{m}$ precision. The first mirror (1" diameter, flat surface as used in the Coherent *ExciStar* resonator) was polished from both sides and specified to have a reflectivity of 96%. The second mirror, a 45° mirror similar to the ones from the OTIMA-TLI beamline was fixed on the translation stage. The interference pattern was visible as fluorescent pattern on the unpolished side of the mirror. For better visibility of this pattern additionally a fluorescent plate was attached closely to the backside of the mirror. A plastic foil tube was fixed around the interferometer and the laser aperture. The interference pattern was then recorded with a beam profiler³⁸ through a window at the

³⁸*Spiricon* Sp-620U

end of the plastic tube.

Mechanical vibrations became manifest in fluctuations of the interference fringe width, spacing and contrast. Averaging over sufficiently many images was therefore necessary. It was furthermore essential to subtract a reference image recorded with a strongly misaligned cavity from the interference pattern, since the input mirror itself produced fringes.

Aim of the measurement was to record the interference pattern at increasing mirror distance and to determine the fringe visibility. The longitudinal coherence length is *twice* the mirror distance at which the visibility has decayed to $1/e$ times the maximum value.

We started at a minimum distance of 1 mm³⁹. The distance was increased in steps of 10 μm and at every position 250 images of the pattern were taken. The camera software did not allow to export images in ASCII format. To overcome this limitation a C-routine was implemented which, at the click of a button, saves 250 screenshots of the camera display. Also, since the camera software solely displays RGB-colormaps, the images were processed in a MATLAB-script and converted from RGB-maps to HSV-maps (*hue*, *saturation* and *value*, where *value* stands for the intensity). Mapping the third column of the *.hsv* files resulted in the desired intensity maps. In each of the images the contrast along 3 lines (typically crossing 5-10 fringes) was computed. With this scheme at each mirror position a contrast averaged over 750 data points was obtained. The statistical error of this measurement was around 10% and similar to a preceding measurement with 200 pictures per position.

Figure 26 shows the result of this experiment. The data is best fitted by

$$y_{fit} = e^{-Ax}, \quad \text{with } A = 0.16(30). \quad (64)$$

The highest visibility is conservatively approximated by 90%, thus resulting in a coherence length of

³⁹This was limited by the rims of the mirror mounts.

$$\lambda_{coh} = -\frac{2}{A} \ln\left(\frac{0.9}{e}\right) = 13,56 \text{ mm.} \quad (65)$$

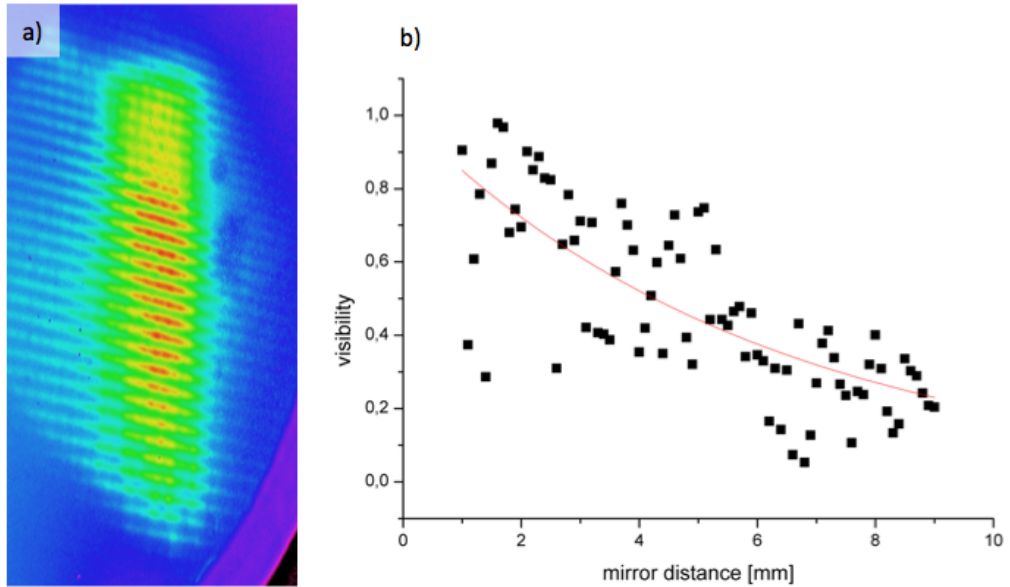


Figure 26: *a)* Typical RGB-image of an interference pattern. *b)* Black dots: visibility of the interference fringes versus mirror distance. Red line: exponential fit to the data

This value is comparable to the literature value (14,3 mm [70]). The strong deviation of the experimental curve from an exponential decay can be attributed to several systematic errors in the setup. Firstly, the cavity mirrors are not mounted very stable. This leads to fluctuations of the fringe pattern. We also can't exclude the possibility that the translation stage may tilt the mirror as well. This would lead to an error, since the fringe visibility depends on the finesse of the cavity which, in turn, also depends on the angle between the mirrors. Secondly, the mirrors used in the interferometer do not have matching reflectivity. Equally high reflectivity of the mirrors would increase the finesse and thus make the measurement more accurate. Thirdly, the recording of the interference pattern lacks sufficient precision. An alternative to the ccd-camera imaging could be a photodiode with a small

active area. Since a single photodetector does *per se* not have any spatial resolution one could e.g. mount one of the mirrors on a piezo-ring and have the cavity length oscillate with a small frequency and amplitude, so that the fringes would scan over the active area of the photodetector. With an oscilloscope one could then very easily measure the visibility.

6.9 Interferometer alignment

Aligning of the OTIMA-TLI includes positioning of the laser beams on the interferometer mirror, overlapping the back-reflections with the incoming laser spots and tuning of the time delays. All these alignments are adapted to the particle beam. As derived in section 5.3 a timing imprecision $\delta\tau$ of the grating pulses can be tolerated as long as

$$\frac{\delta\tau}{T_t} < \frac{1}{N} \quad (66)$$

holds, where N is the number of slits illuminated by the particle beam. As explained in section 6.2.2, the specifications of the current setup leads to approximately $N = 6500$. This sets an upper bound to $\delta\tau < T_t/6500$ which corresponds to a deviation from the required pulse timing precision of 0.015%. This means that an experiment with 5000 amu clusters requires the pulse timing to be accurate up to 12 ns. Since the upper bound for $\delta\tau$ depends linearly on the particle mass, the pulse timing requirements relax with increasing mass. These calculations show that already a nanosecond jitter of the grating pulses can be problematic for the experiment. This necessitates the jitter monitoring system described in section 6.10.

Compared to a material grating setup, light gratings are favorable since they have a fixed phase relation, defined by the mirror surface. Nevertheless the lasers have to be aligned to be orthogonal on the mirror surface. This is in practice done by overlapping the back-reflection with the incident laser spot on one of the beamline mirrors, typically the last before the interferometer mirror. The laser spots are diffusely visible as blue fluorescence on the mirrors and matching the back-reflection with the spot of the incoming beam can be done with an accuracy of approximately 1 mm. The distance between the

interferometer mirror and the last beamline mirror is around 0,6 m which means that the orthogonality of the lasers on the interferometer mirror can be aligned with an accuracy of about $\beta = 1,5$ mrad.

This angle is important for two reasons: First, since standing waves are an interference phenomenon, the visibility can only be 100% if the incident and reflected photons pass each other in a distance shorter than the transversal coherence length. The transversal coherence length is defined as

$$\lambda_{coh}^t = \frac{\lambda_{laser}}{\alpha}, \quad (67)$$

where α is the divergence angle of the beam and λ_{laser} its wavelength [21]. The visibility of the standing wave thus reaches $100\% \cdot 1/e$ at a distance of

$$x = \frac{\lambda_{coh}^t}{\tan \beta} = \frac{\lambda_{laser}}{\alpha \tan \beta} \quad (68)$$

from the interferometer mirror surface. Our VUV-lasers are specified to have a divergence angle of 0,8 mrad [77]. This divergence angle together with $\beta = 1,5$ mrad and $\lambda_{laser} = 157,63$ nm gives $x = 13,08$ cm which is well above the limit set by the longitudinal coherence length of around 1 cm (see section 6.8). The transverse coherence length can thus be neglected as a reason for a visibility reduced standing wave. The angle β is also important because a misalignment effectively changes the grating period. This is depicted in figure 27. The orthogonal component \vec{k}_o^i of the incident wave vector \vec{k}^i is related to the misalignment angle β via

$$|\vec{k}_o^i| = |\vec{k}^i| \cdot \cos \beta. \quad (69)$$

The effective periodicity of the standing wave is then

$$d_\beta = \frac{\pi}{|\vec{k}_o^i|} = \frac{\pi}{|\vec{k}^i| \cos \beta} = \frac{\lambda_{VUV}}{2 \cos \beta}. \quad (70)$$

If we insert $\beta = 1,5$ mrad into this equation we arrive at a d_β which deviates from d by $\Delta d = 0,09$ pm. This is small enough to be neglected.

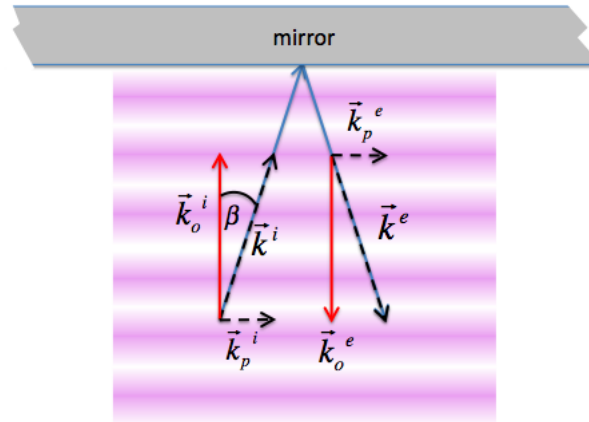


Figure 27: The orthogonal component \vec{k}_o^i of the incident wave vector \vec{k}^i decreases in length if the misalignment α increases. This gives rise to a change of the grating period.

The results of this section show that while the laser gratings are relatively simple to align in space, accomplishing the needed accuracy in time can be challenging

6.10 Jitter monitoring

We found that the jitter of the laser emission during normal operation at a repetition rate of 200 Hz ranges from a few nanoseconds to occasional jumps up to $50 \mu\text{s}$. The nanosecond-jittering is inherent to all discharge pumped gas lasers. We suspect the $50 \mu\text{s}$ jitters to be due to a technical defect of the electronic circuit to be fixed at the next service.

In the mean time we have overcome these complications by implementing a jitter monitoring system, which allows us to record the shooting times of the lasers while the experiment is running. The actual pulse timing is then compared to the trigger signal and *MOPS* will collect counts with the same $\Delta_{tot} = |\Delta_{G1-G2} - \Delta_{G2-G3}|$, where Δ_{G1-G2} and Δ_{G2-G3} are the delays between G1 and G2 and G2 and G3 respectively (see figure 28). During processing of the data one can choose up to which Δ_{tot} to sum the data. Experiments with

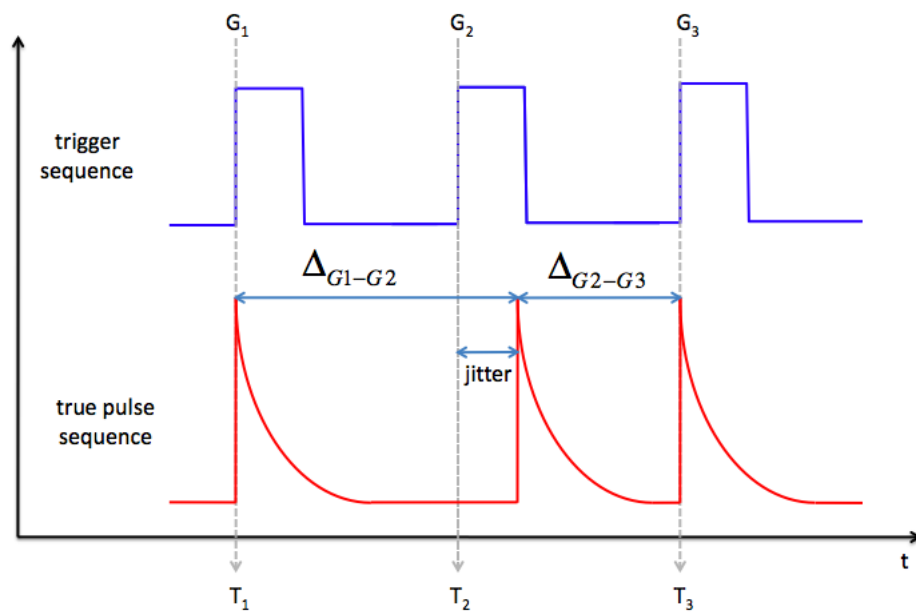


Figure 28: Schematic visualization of the jitter between the laser trigger sequence and the true pulse sequence. The gratings are denoted by G_1 , G_2 and G_3 which appear at times T_1 , T_2 and T_3 . A jitter in the pulse time of the center grating causes the respective jitters Δ_{G1-G2} and Δ_{G2-G3} .

a μs -jitter are discarded. *MOPS* then adapts the timing for the subsequent pulses so that the shift is compensated.

Initially the jitter monitoring system was experimentally realized with three amplified photodiodes⁴⁰ at the rear cavity mirrors of each grating laser. These photodiodes measured the timing of the red F_2 -emission. This had the advantage of not necessitating nitrogen purging. However, it has turned out that there is a random jitter not only from VUV-pulse to VUV-pulse but also between the red fraction and the VUV-emission. Further problems of the setup arose due to the combining of the three photodiode signals⁴¹. Insufficiently matched load impedances led to reflections which modulated the signal and created additional noise. An improved setup circumvents the problem of unmatched impedances by using only one photodiode⁴² which is mounted directly inside the optics box. The position is chosen so that the detector collects stray light from all three lasers. With $50\ \Omega$ termination and 12 V bias of the diode the signal is several 100 mV high.

6.11 Relevance of vibrations

In general near-field interferometers for molecules are extremely sensitive to vibrations [78]. The OTIMA-TLI is no exception in this respect: mechanical vibrations can be detrimental to the visibility and thus need to be carefully analyzed and eliminated.

Interferometer oscillations have to be separated in those with a period on the scale of the Talbot time and below and those that appear on a scale much larger than the Talbot time. In the latter case the relative phase of the gratings with respect to a common reference is approximatively constant during one experiment. In the former case however a random offset is inherent in the interference pattern and the visibility washes out when averaging over many shots. This is the case as soon as the vibrations appear on a frequency

⁴⁰Thorlabs

⁴¹The combining of the detector signals was necessary due to a lack of input ports on the ADC-card

⁴²*Thorlabs* DET10A 1ns risetime. Housing, electrics and sapphire window have been removed for VUV-and vacuum compatibility.

scale exceeding the inverse Talbot time. As the size of the investigated clusters increases, slower frequencies become relevant: particles exceeding a mass of 60.000 amu already have an inverse Talbot time in the order of 1000 Hz. At higher masses acoustic noise thus becomes influential which is known to dominate the noise spectrum of experimental setups similar to the OTIMA-TLI due to the presence of turbo pumps, cooling systems and other machinery [78].

The OTIMA-TLI now differs from a conventional TLI in the fact that independent vibrations of the gratings do not occur⁴³ since all laser pulses are reflected from the same mirror. The possible modes of the mirror vibrations are shown in figure 29: the mirror may rotate around its center or an arbitrary axis (see in figure 29 a) and b)) or shift along the surface normal (see in figure 29 c)) or parallel to the surface (see in figure 29 d)). Of course combinations of these modes are possible as well.

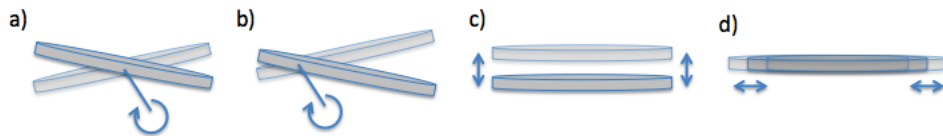


Figure 29: Possible vibrational modes of the OTIMA-TLI mirror are exaggeratedly sketched. In the low frequency regime all four cancel out.

Among the shifts the gratings may experience as a result of the mirror vibration only those are of interest which are parallel to the grating vector: shifts that change the distance between the gratings are not possible and shifts along the grating slits don't have any effect on the visibility. Tilting of the mirror also alters the alignment of the standing waves since it changes the angle between incident laser beam and the surface. It can thus in principle causes a change of the grating period. We may, however, neglect the vibration-induced change of the grating constant for the same reasons pointed out in section 6.9: the mirror would have to rotate by a few degrees in order to have a visibility reducing effect on the grating constant. Such

⁴³i.e. if a bending of the mirror surface is excluded

large displacement of the mirror would be visible with the bare eye, which we do not observe. We can thus safely exclude this possibility.

The effect of a grating shift along the grating vector can be expressed in terms of the fringe position in the plane of the third grating. This position \vec{X} as a function of the displacement Δx_i of the i -th grating reads:

$$X = \Delta x_1 - 2\Delta x_2 + \Delta x_3. \quad (71)$$

This is shown in figure 30 for the case of three equally spaced single slits. The result applies equivalently to a three *grating* setup.

Since the interference signal is often sinusoidal it is convenient to express the effect of grating displacements in term of a *phase* of the signal:

$$\Phi = \frac{2\pi}{d}X = \frac{2\pi}{d}(\Delta x_1 - 2\Delta x_2 + \Delta x_3), \quad (72)$$

where d is the grating period. The phase Φ should not be confused with the matter wave phase. In fact, the shift of the density distribution due to grating displacements is the same as in a classical Moiré device [79].

Equation (72) shows that certain grating displacements do not alter the position of the interference pattern in the plane of the third grating. A linear displacement of the mirror as shown in sketch *c*) of figure 29 has thus no effect on the experiment if it oscillates at a frequency much larger than the inverse Talbot time. This also applies for tilting around a central axis (a in figure 29): the center grating is at its original position and the phases introduced by the first and last grating cancel out. The situation does not change if the mirror tilts by an off-center axis: the final phase will be equal to zero.

The situation, however, becomes more complicated when the mirror position can no longer be taken as static on the scale of the Talbot time. In this case the fringe pattern has a random phase from shot to shot and the visibility averages out unless the phase of each shot is known. For this reason a Michelson vibrometer is implemented in the OTIMA-TLI which measures the mirror displacement. This allows to record the grating shifts Δx_i as functions of time and thus calculate Φ for each shot. The vibrometer

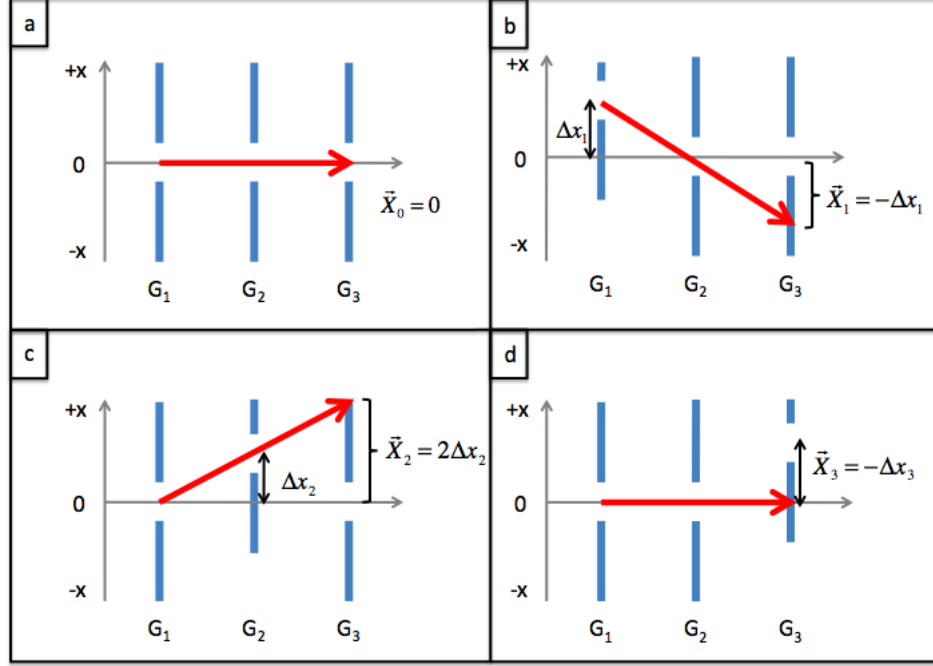


Figure 30: The influence of grating displacement in a three grating setup is shown. The red arrow indicates the particle ray trajectory. As simplification only single grating slits are considered which are displaced one at a time. In all pictures the gratings are equally spaced. The ideal case of no displacement is shown in picture *a*. X_i denotes the final position of the particle distribution in the plane of the third grating when the i -th grating is displaced. When all gratings are displaced simultaneously, the red arrow points at $X = X_1 + X_2 + X_3$.

setup is in detail described in [80]. It consists of a Michelson interferometer operated at $\lambda = 633$ nm with the OTIMA-TLI mirror closing one of the arms. The length of the other arm is adjusted with a piezo electric actuator so that the phase of the error signal remains constant. If the signal is locked to its linear slope the amplitude A is linearly related to the displacement Δx by

$$\Delta x = \frac{A}{A_{max}} \frac{\lambda}{4}. \quad (73)$$

A_{max} is the amplitude of the error signal corresponding to $\Delta x = \lambda/4$ which is the limit of the Michelson interferometers sensitivity. It is

determined by scanning the length of the reference arm over a distance exceeding $\lambda/4$ and recording the highest amplitude of the error signal during the scanning.

The vibrometer setup rests on a vibration isolation platform⁴⁴. The laser aims at the OTIMA-TLI mirror from underneath the optical table and is coupled into the vacuum chamber via a window in the optics box. The vibrometer is thus decoupled from the noisy environment to measure the mirror displacement with respect to the stable reference of the damping platform. Decoupling the measuring reference from the optical table also brings the advantage of measuring the displacement of the OTIMA-TLI mirror in the relevant reference frame of the earths gravitational field rather than the vacuum chamber.

Generally the laser vibrometer is advantageous due to the fact that it measures the motion of the mirror without being mechanically in contact with it.

6.12 Relevance of inertial forces

Although the fringe visibility in the time-domain interferometer is within the loose limits of the criteria (57) and (58) independent of the velocity selection, a velocity dependence can arise due to velocity-dependent inertial forces such as the *Coriolis* force. The Coriolis force is a fictional force that acts on particles moving in a rotating inertial system [81]. If ω is the angular frequency at which the reference frame is rotating and \vec{v} the velocity of a particle (with respect to the rotating reference frame) with the mass m , the Coriolis force on the particle reads:

$$\vec{F}_C = 2m(\vec{v} \times \vec{\omega}), \quad (74)$$

which is zero for $\vec{v} \parallel \vec{\omega}$. The Coriolis force thus does not act if the motion is parallel to the axis of rotation. For a particle moving on earth it is therefore

⁴⁴*Minus K, Inc.* BM08-25. This platform damps frequencies larger than 0.5 Hz with up to 60 dB. It operates passive without air or electricity.

convenient to express the velocity in terms of its north-south v_{NS} , east-west v_{EW} and radial component v_a parallel to the earth's gravity:

$$\vec{v} = \begin{pmatrix} v_{EW} \\ v_{NS} \\ v_a \end{pmatrix}. \quad (75)$$

The angular frequency ω depends on the latitude ϕ of the lab location. The earth rotates by 360° in approximately 24 h or 86.400 s and thus at a frequency of $\omega = 7,3 \cdot 10^{-5}$ Hz. The rotation vector for our lab reads:

$$\vec{\Omega} = \omega \begin{pmatrix} 0 \\ \cos \phi \\ \sin \phi \end{pmatrix} \quad (76)$$

and the Coriolis force on the particles therefore takes the form

$$F_C = 2m\omega \cdot \begin{pmatrix} v_a \cdot \cos \phi - v_{NS} \cdot \sin \phi \\ v_{EW} \cdot \sin \phi \\ -v_{EW} \cdot \cos \phi \end{pmatrix}. \quad (77)$$

Our lab is located on N48°13' 19,2" lat. (or $\phi=48,22^\circ$) and the bearing of the particle beam is $\alpha = 164^\circ$. In principle one has to take into account also the divergence angle (≈ 3 mrad) of the beam since this results in a "bearing spread" within the particle beam. This however is neglected in the following. First we assume particles with a mass m to propagate with a mean velocity of v_0 . The Coriolis acceleration a_C is thus:

$$a_C = \begin{pmatrix} a_C^{EW} \\ a_C^{NS} \\ a_C^a \end{pmatrix} = 2v_0\omega \cdot \begin{pmatrix} v_a \cdot \cos \phi - \cos \alpha \cdot \sin \phi \\ \sin \alpha \cdot \sin \phi \\ -\sin \alpha \cdot \cos \phi \end{pmatrix}. \quad (78)$$

We consider the acceleration parallel to the grating vector (x-axis in figure 3) and the phase shift Δs induced by this component of a_C reads:

$$\Delta s = a_C^a (T_t)^2 = -2v_0 T_t^2 \omega \sin \alpha \cos \phi. \quad (79)$$

For particles with a mass of 4000 amu and a Talbot time of $T_t = 61,5 \mu\text{s}$ this gives $\Delta s = 27,3 \text{ pm}$ which is most likely too small to be detected as a shift of the pattern. For particles with a mass of 40.000 amu the shift comes to 0,3 nm, and for a mass of 10^6 amu it is around 18 nm which is significant. If the velocity distribution of the particles were infinitely narrow Δs would simply add a constant phase to the interference pattern and not reduce the visibility. In a more realistic situation, however, the velocity selection has a certain width determined by the velocity selection. We can assume this velocity selection to allow for a maximum velocity of v_{max} and a minimum of v_{min} . The resulting signal (for simplification we calculate with the sinusoidal visibility) at the time of the third grating is thus a superposition of

$$\Delta s_{max} = (-4T_t^2 \omega \sin \alpha \cos \phi) v_{max} \quad \text{and} \quad \Delta s_{min} = (-4T_t^2 \omega \sin \alpha \cos \phi) v_{min}. \quad (80)$$

If the velocity selection prepares a velocity spread in the beam of $\Delta v/v_0 = 10\%$ with $v_0 = 4z_l h/m\lambda_{UV}^2$, the visibility reduction caused by the vertical component of the Coriolis acceleration therefore lies around 1 % for particles with a mass of around 40.000 amu. This is a negligibly small reduction of the visibility. For a particle mass of 10^6 amu the visibility is reduced by 0.1% for $\Delta v/v_0 = 10\%$. One has to keep in mind though that theoretically the lower bound for the velocity selection lies well above 10% (as pointed out in section 6.3), i.e. if the signal intensity allows for this, and experiments with a velocity spread of 30% or more are very much imaginable. In this case the visibility in an experiment with a mass of 10^6 amu particles would be reduced by approximately 20%.

Next we discuss the influence of the Coriolis acceleration in the propagation direction. This component reads:

$$a_C(v_a) = \frac{a_{NS}}{\cos \alpha} = 2\omega \frac{\cos \phi}{\cos \alpha} \cdot v_a - v_0 \cdot \sin \phi. \quad (81)$$

To illustrate the impact of this acceleration we assume that de Broglie waves which interfere with one another are maximally separated by $2d$ at

the second grating. For this reason the velocity component parallel to the gratings reads $v_a = 2d/T_t$ and

$$a_C \left(\frac{2d}{T_t} \right) = 2\omega \frac{\cos \phi}{\cos \alpha} \cdot \frac{2d}{T_t} - v_0 \cdot \sin \phi \quad (82)$$

Wavepackets that are split and reunited thus experience an acceleration along the longitudinal direction depending on the separation. This induces a pathlength difference Δs between de Broglie waves that are reunited at the third grating which reads:

$$\Delta s = \frac{1}{2}(2T_t)^2 \left| a_C \left(\frac{2d}{T_t} \right) - a_C(0) \right| = 8\omega \left| \frac{d \cdot \cos \phi}{\cos \alpha} \right| T_t \quad (83)$$

The separation caused by the Coriolis force is thus proportional to the Talbot time. For a Talbot time of $60 \mu\text{s}$ ($\hat{=} 4000 \text{ amu}$) equation (83) yields $\Delta s = 2,4 \text{ fm}$ and consequently for a Talbot time of $600 \mu\text{s}$ ($\hat{=} 40.000 \text{ amu}$) $\Delta s = 24,0 \text{ fm}$. For a particle mass of 10^6 amu , however, the shift already amounts to $\Delta s = 0,5 \text{ pm}$.

This shift can be neglected as long as it is well smaller than the longitudinal coherence length λ_{coh}^{long} , which depends on the velocity spread $\Delta v/v_m$ via:

$$\lambda_{coh}^{long} = \frac{\ln 2}{\pi} \frac{\lambda_{db}^2}{\Delta \lambda_{db}} = \frac{\ln 2}{\pi} \frac{h}{m} \frac{1}{\Delta v}, \quad (84)$$

where λ_{db} denotes the de Broglie wavelength. If we assume a velocity spread $\Delta v/v_m = 10\%$ we arrive at $\lambda_{coh}^{long} \approx 0,690 \text{ pm}$, which is independent of the mass if the mean particle velocity is assumed to be $v_m = 4z_l h/m\lambda_{VV}^2$, where h is the Planck constant and z_l the distance between two laser gratings. Even if the velocity selection is as loose as allowed by (57) and (58) and the velocity spread in the particle beam $\Delta v/v_m$ is 60% the coherence length is around $\lambda_{coh}^{long} \approx 0,011 \text{ pm}$ which is at least up to mass of 40.000 amu larger than the shift imposed by the Coriolis force.

The results of this section show that for experiments feasible in the current OTIMA-TLI configuration (mass $< 25.000 \text{ amu}$) the influence of Coriolis forces can safely be neglected. For future experiments they may need to be taken into consideration as a source of visibility reduction (influence of a_C^a)

and as a source of dephasing (influence of $a_C(v_a)$). This requires the particle beam to be aligned to point north or the velocity selection to be adapted accordingly. As stated above, these measures can eliminate the influence of the Coriolis force.

6.13 Particle considerations

In order to be suited for the OTIMA-TLI, particles have to meet certain requirements. The first and most critical property is the single-photo ionizability at 157 nm, necessitated by both the detection and the absorptive laser gratings. Besides many metals (e.g. all alkali metals, gold silver, vanadium, tantalum, niobium, mercury) also certain organic complexes fulfill this requirement (e.g. anthracene, porphyrine). Further requirements depend on the choice of the interference scanning method.

There are essentially two different methods for scanning the interference pattern: the first one is the *mass scan*, where interference is detected as a higher (or lower) transmission for masses which meet the Talbot resonance. This works particularly well with metal clusters, however clusters consisting of small mass atoms are preferable: a smaller atomic mass results in a higher peak density in the mass spectrum and thus allows to resolve modulations in the transmission curve with higher precision. Also metals without stable isotopes are handy since isotopes can cause ambiguity during the mass unfolding process (see section 6.14).

An alternative to this scanning scheme is the *time scan* which works without further modifications of the setup for sufficiently high masses. The time scan requires the particles to be gravitationally deflected by more than half the grating period in a time span much shorter than the Talbot time. If this is the case one may scan the time delay between the gratings which renders higher or lower transmission depending on how far the particles are deflected in the earths gravitational field. If instead an electrostatic field is employed (which requires to mount electrodes next to the mirror) this method becomes feasible also for smaller masses. This scheme does not need an entire mass spectrum which makes it interesting also for particles that don't form clusters

(large organic complexes, see above).

The OTIMA-TLI also works as an atom interferometer, as long as the photon absorption cross section of the atoms is not too small⁴⁵. In this special case one could even profit from a high number of stable isotopes which correspond to different Talbot times. The interference with atoms might be interesting for the alignment of the interferometer and for a proof-of-principle measurement, demonstrating the functionality of the absorptive laser gratings.

6.14 Mass spectra

In this section a closer look is taken at the mass spectra of metal clusters that are emitted from the sputtering source. Usually these mass spectra show three or four superimposed mass distributions. This is due to the fact that the flight time measured in the TOF-MS is proportional to the square root of the charge-to-mass ratio. Two-fold (three-fold etc.) charged ions thus appear in the time-of-flight spectrum at the same positions as the singly charged ions with half (a third of etc.) the mass. This can be seen in figures 31a) and 32a) which display spectra of vanadium clusters and niobium clusters respectively. The vanadium spectrum exhibits up to four-fold charged ions. Higher mass clusters are usually more likely to absorb more than one photon due to their larger absorption cross section.

The raw data initially shows the intensity as a function of the time-of-flight and obtaining a true *mass* spectrum necessitates a re-calibration of the x-axis. Usually this mass calibration requires knowledge of the atomic mass of the cluster material (which corresponds to the distance between two peaks) and at least one absolute mass corresponding to a certain time-of-flight. Both are provided as soon as the atom peak can be identified. Often however this peak does not appear in the spectrum because of the atom lacking a sufficiently large photon absorption cross section to be ionized and detected. We have circumvented this problem by implementing a mass unfold plugin to the *MOPS* software. This plugin generates a mask of peaks at positions

⁴⁵This is the case e.g. for molybdenum.

$$m(t) = At^2 + Bt + C, \quad (85)$$

and allows to manually adjust the parameters A , B and C such that the mask overlaps with the spectrum. The peak at the smallest non-zero position then gives the position of the atom peak, even if it does not appear in the spectrum. In such a way one can not only perform the mass calibration but also extract the multiply charged ions and, if desired, shift them to the position corresponding to their true mass. Usually one would expect the positions $m(t)$ to depend only quadratically and with a certain offset C on the time-of-flight via $m(t) = At^2 + C$, where A and C depend from the spectrometer settings and geometry as well as the particle charge. However, we have found that adding the proportional term allows to match the mask with the spectrum with higher precision.

The spectra of multiply charged ions are constructed with the same mass unfolding procedure. Every second (third, fourth etc.) peak of the doubly (three-fold, four-fold, etc.) charged ions overlays the singly charged peak. Multiple-charge peaks which are overlaid with single-charge peaks are reconstructed by interpolating between the two adjacent peaks. In order to obtain the spectrum consisting of purely singly charged ions the peaks of the multiply charged ions are removed. It is usually sufficient to consider only the peaks of the single-charge ions without merging the multiple-charge peaks in the spectrum. This is due to the fact that the masses relevant for the OTIMA-TLI at present are situated well within the spectrum of singly charged ions.

Figures 31b) and 32b) show the vanadium and niobium spectra after removing the peaks corresponding to multiply charged ions.

Prior to the mass unfolding the mass spectra have to be extracted from the raw signal. This is accomplished with a peak finding plugin of the *MOPS* software which monitors the live signal. The first version of this plugin functioned such that when a peak was detected at a certain time, the height of the peak in the mass spectrum at this position was increased by one count. This is how the spectrum in figure 31a) was acquired. The drawback of this

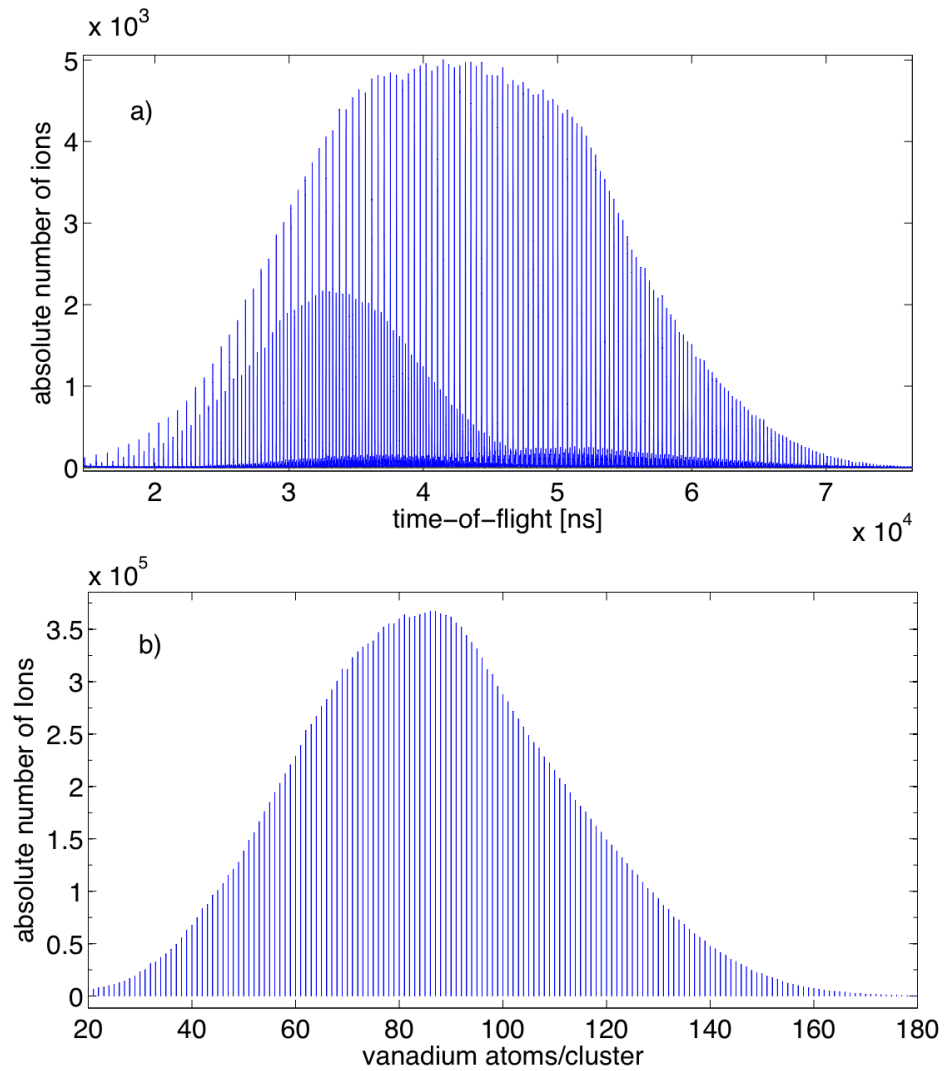


Figure 31: a) vanadium time-of-flight cluster spectrum with spectra of multiply charged ions superimposed. b) mass spectrum of a) after removal of the peaks corresponding to multiply charged ions. For this measurement we have averaged over 960.000 counts.

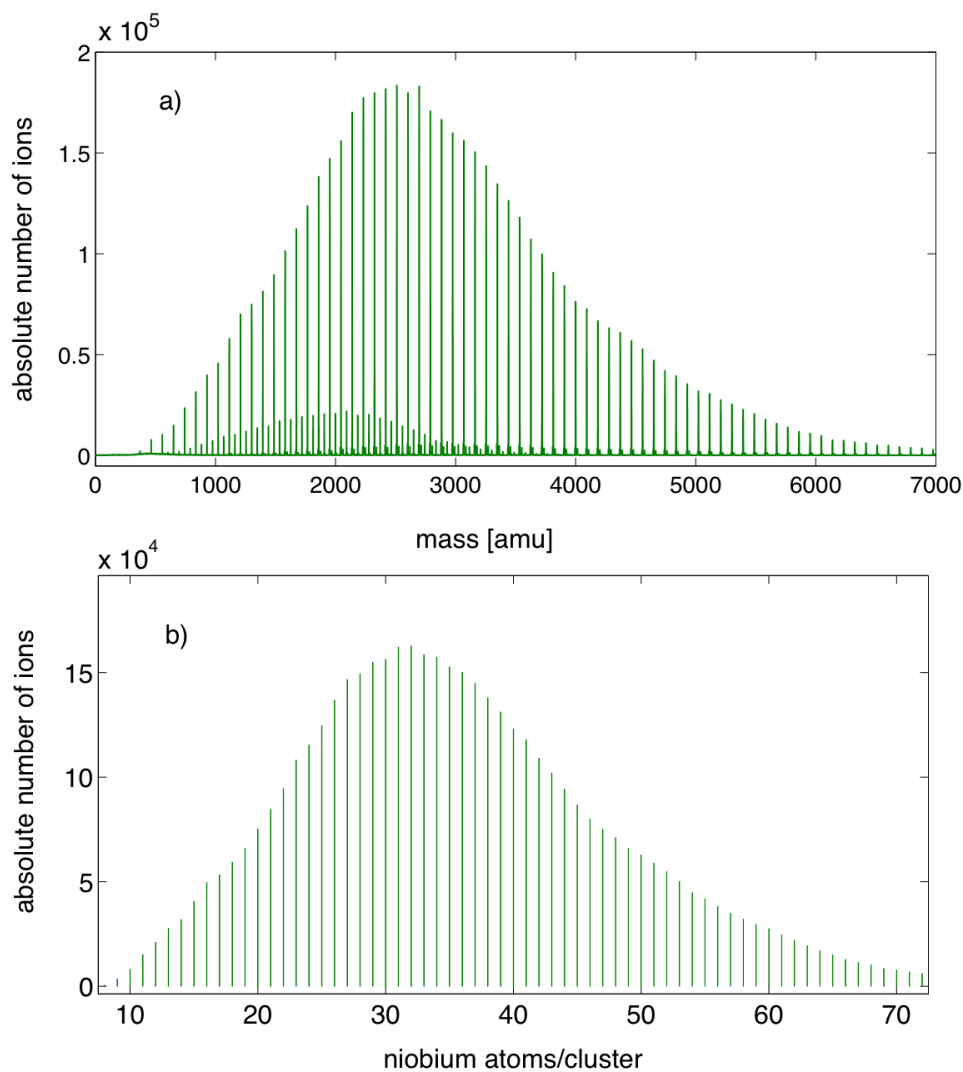


Figure 32: a) niobium mass spectrum again with spectra of multiply charged ions superimposed. b) same spectrum as in *a*) after removal of the peaks corresponding to multiply charged ions. For this measurement we have averaged over 880.000 counts. Note that the spectra are half as dense as the vanadium spectra due to the almost twice larger atomic mass of niobium (= 93 amu).

method is that it is not sensitive to simultaneously arriving ions. This caused a flattening of the tip since in this mass range the number of ions arriving simultaneously is particularly high. The peak finder was thereafter modified so that the increment added to the final spectrum depends on the number of ions, even if they arrive simultaneously. This has solved the issue, as can be seen in in figure 32a), where the flattening of the spectrum tip does not occur.

7 Outlook

7.1 Selection criteria for an alternative laser system

The molecular F_2 VUV-lasers offer several advantageous features for the OTIMA-TLI: the short wavelength reduces the length of the interferometer and the relatively high photon energy promises large single photon ionization efficiency. These advantages, however, are to be weighed against several disadvantages: the high absorption of VUV-photons by most materials constantly necessitates beam line purging, optics are costly and the coherence length is short compared to other laser systems: Even with a coherence length of around $\lambda_{coh} = 1$ cm (see section 6.8) the visibility of the standing wave is high up to a distance of $s = \lambda_{coh}/2 = 0,5$ cm from the interferometer mirror surface. Particles will thus fall out of the range of the laser gratings if their mass exceeds

$$m = \frac{4h}{\lambda_{VUV}^2} \sqrt{\frac{s}{2g}}, \quad (86)$$

where g is the gravitational acceleration. With the cryogenic buffer gas stage we hope to cool down the particles to a mean velocity of $v_m = 50$ m/s. If the distance between the gratings is 2 cm, this corresponds to a Talbot time of 0,4 ms and a mass of 25.700 amu.

In addition to the drawback of a short coherence length there is no possibility to tune the wavelength of the VUV-lasers which might be desirable for spectroscopic measurements in the OTIMA-TLI setup.

7.1 Selection criteria for an alternative laser system

From a very practical point of view one could add that the VUV-lasers are quite service intensive and suffer from a weak service infrastructure throughout Europe.

These reasons motivate the search for a substitute laser system which can replace the VUV-lasers in either the current setup of the OTIMA-TLI or a successive experiment. In this section the requirements for such a laser system are discussed and the available solutions briefly reviewed.

The first and major criterion is the wavelength. Since the Talbot time scales quadratically with the grating period a longer wavelength requires either the particle velocity to be smaller or the length of the interferometer longer. Both renders additional difficulties: the slowing of particles for obvious reasons and the lengthening of the interferometer since this not only complicates the production of an interferometer mirror but also makes the setup more susceptible for vibration-induced visibility reduction. As a compromise we could accept a wavelength up to 220 nm. For particles with 10^6 amu this would require a grating distance of 3,5 cm and a mean particle velocity of 1 m/s, which is both experimentally challenging but feasible. Working with a rather common wavelength like 213 nm would be specially pleasant due to the comercial availability of 213 nm optics and laser systems.

The longitudinal coherence length for the new laser system must be significantly better than the one of the existing system (≈ 1 cm). Especially if future experiments will focus on trapped molecules it is desirable to have at least a coherence length of 10 cm. The transversal coherence length does not have to exceed the specifications of the current laser system. A longer transversal coherence would only be necessary if future modifications of the setup would complicate the alignment of the standing waves and reaching the alignment precision of the current setup could not be guaranteed.

The current laser system has the advantage of providing a beam shape and dimension that is ideal for the OTIMA-TLI: the beams are wide in the particle beam direction and sufficiently homogenous perpendicular to it. These criteria should be fulfilled by the new system as well. A Gaussian beam profile would suit the purpose as long as the intensity is constant over the width of the collimated particle beam.

These criteria exclude a cw laser system from the list of possible solutions: the required power per pulse is simply too high to be reached by existing continuous ultraviolet lasers.

The laser system must thus be pulsed and capable of generating three pulses with a delay tunable from 50 μ s to 50 ms. The length of the pulses may range from few to 10 ns, while the desired repetition rate of this sequence ultimately depends on the intensity of the implemented particle source. The ideal repetition rate ought to be as high as possible and not significantly smaller than 20 Hz. As far as run-time stability of the laser system is concerned, the requirements again depend crucially on the particle source. With the current magnetron sputter source measurements are likely to last over several days. The laser emission would thus have to be stable in wavelength, pulse timing, pointing and power over the entire measuring period, although the power stability is negotiable if it can be actively controlled. A jitter in the pulse timing can be accepted as long as it does not exceed a few nanoseconds.

Currently the options are: three Nd:YAG lasers with a common seed laser frequency up-converted to a wavelength 213 nm. This would be a nice solution due to the long coherence length, however it is not clear whether such a system is capable of meeting the power stability criterion while maintaining high pulse powers. Alternatively the same Nd:YAG lasers could be used as pumps for a single frequency doubled dye laser. Such a system would bring a certain amount of wavelength tunability but it is not clear if it can provide sufficient pulse power. Short wavelengths could also be reached with three line narrowed ArF excimer lasers (193 nm). It is, however, not clear how well the wavelengths of the three lasers would be matched, considering that the line narrowing in each laser would be prepared with solid state etalons and thus strongly dependent on manufacturing precision of these elements.

7.2 Towards interferometry

Currently the goal of the OTIMA-TLI is to observe first interference of clusters in a mass range from 3000 to 4000 amu. The favorable method for detecting the interference pattern is the *mass scan* where the laser power of

all three gratings remains constant during the measurement. Evidence for the interference is then found in a reduced or enhanced transmission for masses fulfilling the Talbot-Lau resonance condition. This is simulated in figure 33 a) which shows the expected transmission of niobium clusters through the interferometer. The grating pulse delays are set to $T_t = 57,3 \mu\text{s}$ which corresponds to a mass of 3700 amu. The curve shows higher transmission for the 40-atom cluster with an underlying exponential decay. This is due to the fact that the probability for a particle to be transmitted by one of the laser gratings depends exponentially on $n^j(x)$, the mean number of photons absorbed in a grating at the position x (see section 5.4). In $n^j(x)$ enter parameters of the laser beam and the photon absorption cross section which we assume to increase linearly with the cluster mass.

The result of the experiment is shown in panel b) of figure 33. The transmission curve results from dividing the signal obtained without the laser gratings by the signal obtained with the laser gratings. Since the intensity of the signal is much higher when the gratings are switched off it is not necessary to record without the gratings for the same time as with the gratings. We take this into account by measuring without the gratings only for 1/5th of the total measurement time. The overall measurement time was around 30 hours and for the curve shown in 33 b) we have averaged over nearly $3,7 \cdot 10^6$ frames.

Still, the curve does not show the desired evidence for interference. There is a slight “bump in the transmission of Nb_{40} clusters which could be interpreted as a first sign of interference contrast. However, further measurements will be necessary to confirm this speculation.

7.3 Buffer gas cooling stage

For future experiments in the OTIMA-TLI the particles emitted directly by the cluster source will be too fast. Additional cooling of the cluster beam will be necessary. For this the *buffer gas* technique is promising, reason being its rather simple approach and applicability to a wide range of particles [82] [83] [84] [85]. A buffer gas cooler consists of a cell filled with a *buffer gas*

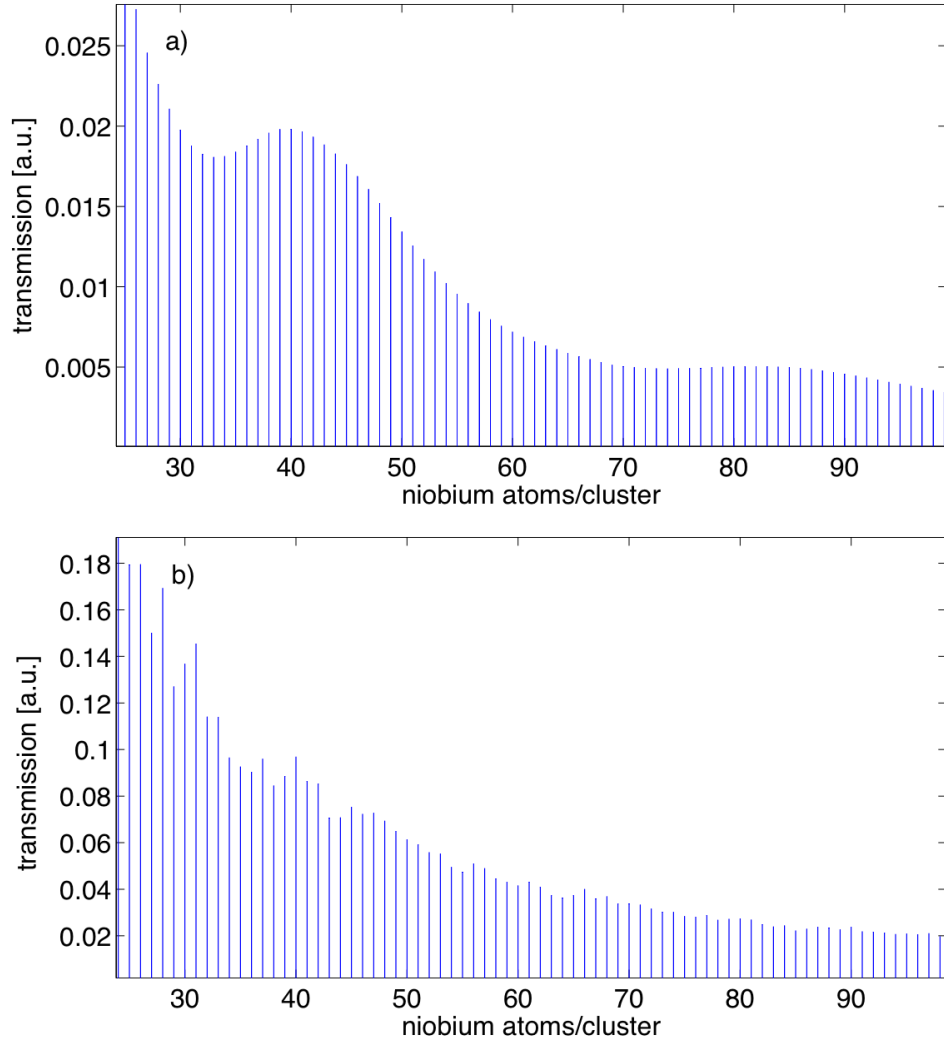


Figure 33: Simulated (panel *a*) and measured (panel *b*) transmission through the laser gratings as a function of the cluster number. The grating delays in experiment and simulation are set to $T_t = 57,3 \mu\text{s}$ which corresponds to a mass of 3700 amu.

which is usually helium or neon⁴⁶. The cell walls are cooled to cryogenic temperatures and the buffer gas thermalizes with the cold walls of the cell after a short period of time. When a beam of particles is introduced to the cell, the particles will interact with the cold buffer gas via elastic collisions. This works efficiently as soon as the mean free path of the particles in the gas is much smaller than the dimensions of the cell. However, if the density of the buffer gas is too high, the particles will cool down too rapidly and stick to the cold cell walls. There are two competing processes that determine the effective velocity of clusters leaving the cooling stage: within the buffer gas cell the clusters will thermalize with the buffer gas which means that they adopt the kinetic energy of the gas particles. Due to their larger mass, however, they will propagate at lower speeds. This method works for a variety of particles, provided they have a sufficiently large elastic scattering cross section. This is naturally the case for large metal clusters. To illustrate this we consider a neon buffer gas (atomic mass $m_{bg} = 20$ amu) at $T_{bg} = 20$ K and 40.000 amu gold clusters. The mean thermal velocity within the buffer gas is $v_{bg} = \sqrt{2kT_{bg}/m_{bg}} = 129$ m/s, where k is the Boltzmann constant. With increasing number of cluster-neon collisions the cluster temperature T_{cl} will approach T_{bg} , so that eventually $T_{cl} \approx T_{bg}$. This gives a cluster velocity of $v_{cl} = \sqrt{2kT_{bg}/m_{cl}} = 2,9$ m/s. If the particles do not leave the buffer gas cell, because e.g. the buffer gas cell accommodates an ion trap [82], one can in fact benefit from this very low velocity. If, however, the cluster beam passes through the buffer gas cell, the particles will be carried in the stream of buffer gas and accelerated to a certain degree. The amount of this acceleration depends on the aerodynamic situation at the cell opening: if this is large enough so that a thermal beam of buffer gas is emitted, the cluster velocity will be close to v_{bg} . This is relatively easy to achieve with an opening large enough so that a supersonic expansion does not occur. Since v_{bg} is already significantly slower than the velocity of clusters directly emitted by the sputter source (≈ 400 m/s), integrating a buffer gas cell is definitely worth the effort. The cluster velocity may even be lower due to the relatively

⁴⁶Argon would be favorable due to its large mass (≈ 40 amu). Even so it cannot be used as a 4 K-buffer gas since it becomes liquid at temperatures below 80 K.

large cluster mass and the resulting inertia⁴⁷. Also there is always a certain velocity distribution which gives the freedom to select slower propagating parts of the particle cloud. We estimate therefore that the effective forward cluster velocity $v_{f,eff}$ will be around

$$v_{f,eff} = \frac{v_{cl} + v_{bg}}{2} \approx 70 \frac{\text{m}}{\text{s}}. \quad (87)$$

The cluster velocity thus depends strongly on the buffer gas temperature as well as the buffer gas particle density. Both are governed by the dimensions and geometry of the cooling cell, as will be shown in the following calculations.

If the translational temperature of the clusters leaving the source is T_i and the buffer gas is thermalized to the cell wall temperature of T_{bg} then a cluster needs to undergo

$$N = -\frac{(m_{cl} + m_{bg})^2}{2m_{cl}m_{bg}} \cdot \ln \left[\frac{T - T_{bg}}{T_i} \right] \quad (88)$$

elastic collisions in order to be cooled down to the temperature T [85]. Here the cluster mass has been denoted with m_{cl} and the mass of a buffer gas particle with m_{bg} . Equation (88) follows from the fact that during an elastic collision both the energy and the momentum are conserved.

The effective number of elastic scattering processes depends on the dimensions of the cell as well as the mean free path Λ and reads:

$$N_{eff} = \frac{L}{\Lambda} = L n_{bg} \sigma_{eff}, \quad (89)$$

where L is the length of the buffer gas cell in particle beam direction, n_{bg} the number density of helium particles and σ_{eff} the effective scattering cross section. The scattering itself is mainly due to the van der Waals interaction between polarizable particles [86] [55]. Therefore the effective scattering cross section σ_{eff} depends only on the velocities of the scatterers (v_{cl} and v_{bg}) and the van der Waals parameter C_6 :

⁴⁷This effect occurs also in the aggregation tube of the sputter source: the cluster velocity here is around 400 m/s and thus much lower than the mean velocity of the carrier gas \bar{v}_{cg} at LN₂ temperature ($\bar{v}_{cg}=560$).

$$\sigma_{eff}(v_{cl}) = \frac{C_6^{2/5} v_{cl}^{3/5}}{\hbar^{2/5} v_{bg}} (8,4946 + 1,6989 \frac{v_{bg}^2}{v_{cl}^2}). \quad (90)$$

This expression results from an approximation for $v_{bg} \ll v_{cl}$. We assume for the following that the buffer gas particle velocity is constantly $v_{bg} = \sqrt{2kT_{bg}/m_{bg}}$ and that the velocity of the clusters is the mean value of the cluster velocity before and after the buffer gas cell. This takes into account that the cluster velocity is reduced with every collision. The van der Waals parameter follows from the *Slater-Kirkwood* expression [55] and reads:

$$C_6 = \frac{3}{2} \frac{e\hbar}{\sqrt{4\pi\epsilon_0 m_e}} \frac{\alpha_{cl}(0)\alpha_{bg}(0)}{\sqrt{\alpha_{cl}(0)/N_{cl}} + \sqrt{\alpha_{bg}(0)/N_{bg}}}. \quad (91)$$

It depends on the number of valence electrons of the buffer gas atoms N_{bg} and the scattered clusters N_{cl} , respectively, as well as from the static dipole polarizabilities $\alpha_{bg}(0)$ and $\alpha_{cl}(0)$.

In an experiment we would use neon as a buffer gas ($N_{bg} = 8$) which has a static dipole polarizability of $\alpha_{bg}(0) = 0,369 \text{ \AA}^3$ [87]. For the clusters the static polarizability and the number of valence electrons have to be approximated, since exact values are difficult to find in the literature. We therefore assume the polarizability of Au_{135} to be

$$\alpha_{cl}(0) = R^3 = \frac{3m}{4\pi\rho}, \quad (92)$$

which is the classic polarizability of an ideal metal sphere with radius R , mass m and mass density ρ . For $m = 40.000 \text{ amu}$ and $\rho = 19,3 \text{ g/cm}^3$ this gives a polarizability per atom of $\alpha_{cl}(0) = 6,0 \text{ \AA}^3$. We can further use the characteristics of an ideal metal by assuming that every atom in the cluster provides its valence electrons, thus neglecting potential shielding effects of inner laying atoms. A gold atom has one valence electron which yields in this approximation $N_{cl} = 135$. Inserting these values into (91) yields $C_6 = 3,022 \cdot 10^{-76} \text{ Jm}^6$, and with $v_{cl} = 230 \text{ m/s}$ and $v_{bg} = 130 \text{ m/s}$ we arrive at an elastic scattering cross section of $\sigma_{eff}(v_{cl}) = 4,38 \cdot 10^{-17} \text{ m}^2$.

In order to cool down the clusters to a temperature 10% above the buffer gas temperature $T_{bg} = 20 \text{ K}$ and under the assumption of an initial temperature

of $T_i = 77$ K (LN₂ temperature) we have to ensure that the clusters undergo $N_{eff} = 2700$ collisions during their passage through the buffer gas (according to (88)). If the length of the buffer gas cell is $L = 6$ cm, the buffer gas density n_{bg} must, following (89), not be smaller than

$$n_{bg} = \frac{N_{eff}}{L\sigma_{eff}(v_{cl})} \approx 8,75 \cdot 10^{20} \frac{1}{m^3}. \quad (93)$$

We can transform this into a pressure p_{bg} via the ideal gas equation $p = n_{bg}kT_{bg}$ and arrive at $p_{bg} = 0,24 \cdot 10^{-3}$ mbar. This can easily be handled by the turbo molecular pumps on the OTIMA-TLI source chamber.

These calculations contain many approximations. Nevertheless, they show that buffer gas cooling of the cluster beam can be achieved. Statements on how well the method works ultimately will have to await first experimental tests. It is clear, however, that the setup will benefit from as many adjustable parameters as possible since these will allow to find the ideal working regime more easily.

7.4 The Even-Lavie valve as a source for the OTIMA-TLI

The magnetron sputter source offers several advantages for our experiment: it produces continuous spectra over a wide range of cluster masses while offering reproducibility of the cluster beam characteristics. However, since it is a *cw* source it is not ideally suited for the pulsed setup of the OTIMA-TLI, a fact that manifests itself in a low signal. Still the experiment can profit from this source since the measurement time is in principle not limited. At a later stage of the experiment measurement times of several days will thus not be a fundamental problem. At this stage, however, a proof-of-principle measurement has yet to be completed and final adjustments may be necessary to observe interference phenomena for the first time. Therefore low brilliance of the particle source is particularly problematic: the time for troubleshooting will depend crucially on the time it takes to record an interference pattern. This motivates the temporary implementation of an

alternative, brighter, source.

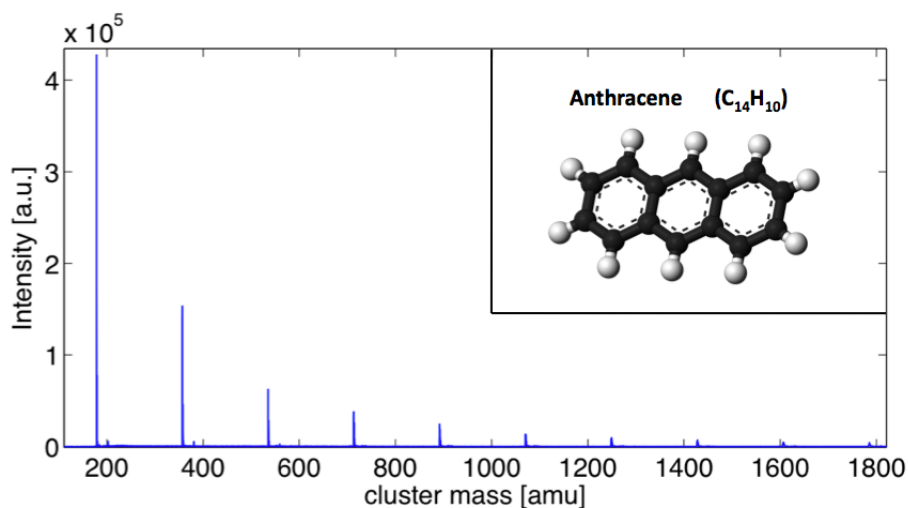


Figure 34: Mass spectrum of anthracene clusters. The spectrum was obtained with the Even-Lavie valve implemented in the OTIMA-TLI setup. (Inset in the upper right corner taken from [88])

The present source of our choice is the *Even-Lavie valve* (EL valve) [89] [90]. This is a pulsed high pressure nozzle which generates supersonic jets of molecules. The nozzle itself consists of a small magnetic hammer which, when at rest, closes the orifice of a small oven chamber. The nozzle opens when the hammer is removed from the orifice periodically by a pulsed magnetic field. Miniaturization of all components allows to operate the nozzle at up to 1 kHz and high pressures inside the oven (up to 100 bar). For the formation of clusters and molecules a flow of carrier gas (Ar, He, Ne) through the oven is maintained. The mean speed of the particles then depends on the mean velocity of the carrier gas particles. During the expansion the molecules pass the energy captured in their internal degrees of freedom (vibrational and rotational states) to the carrier gas particles and cool down in this way. If sufficient cooling is achieved the particles will form clusters.

For a first test the EL-valve has been loaded with anthracene ($C_{14}H_{10}$) and implemented in the OTIMA-TLI setup. Anthracene is a molecule consisting

of 3 benzene rings (see inlet in figure 34) with a mass of 178 amu. It is known to have an ionization potential of around 7,4 eV [91] and to form clusters under conditions comparable to the ones provided in the EL-valve [92].

With the EL-valve operated at 4 bar pressure and 225 °C with an argon seed gas we observe high intensity peaks of clusters consisting of up to 5 anthracene molecules. Such a mass spectrum is shown in figure 34, where we have averaged over 10.000 frames. During measurement we have detected a total of $4 \cdot 10^5$ anthracene monomers which makes nearly 43 per frame. The much smaller peak of the pentamer still counts 2,5 ions per frame. This is a very intense cluster signal compared to the one obtained with the sputtering source, where we have detected *at most* 0,02 niobium clusters per frame (this corresponds to the highest peak of the spectrum in figure 32).

Further we have measured the velocity distribution by scanning the detection delay in $10 \mu\text{s}$ steps from 0,825 ms to 1,325 ms and averaging for each detection delay over 2000 frames. The result is shown in figure 35 in which the velocity distributions of the first five anthracene clusters are displayed. It shows that the most probable velocity in the cluster beam lies around 700 m/s. If we aim at interferometry with the anthracene trimer, which weighs 356 amu, we find that we can accept a velocity of 3600 m/s in the first Talbot order and a spacing between the laser gratings of 2 cm. If, however, we go into the 5th Talbot order, i.e. to path separations of the order of 400 nm, we are satisfied with a velocity of 722 m/s.

This shows that OTIMA-interferometry with anthracene clusters is feasible as far as signal intensity and velocity is concerned. Although the mass peaks are rather sparse it should be possible to visualize the interference pattern as a modulation in the transmission curve (*mass scan*).

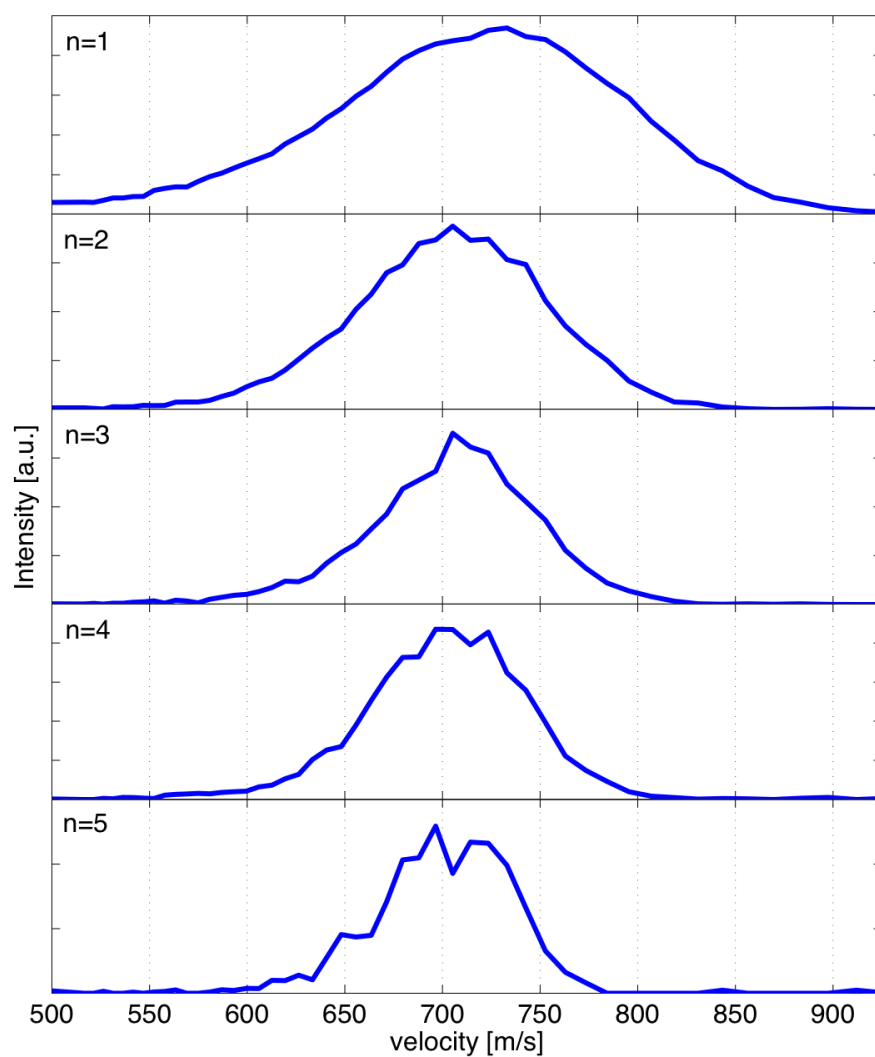


Figure 35: Velocity distributions of the smallest 5 anthracene clusters. The y-axes are not in scale. For true signal intensities see figure 34.

References

- [1] E. Schrödinger. Die gegenwärtige Situation in der Quantenmechanik. *Naturwissenschaften*, 23:823–828, 1935.
- [2] J. F. Clauser. *Experimental Metaphysics*. Kluwer: Academic Press, 1997.
- [3] A. D. O’Connell, M. Hofheinz, M. Ansmann, Radoslaw C. Bialczak, M. Lenander, Erik Lucero, M. Neeley, D. Sank, H. Wang, M. Weides, J. Wenner, John M. Martinis, and A. N. Cleland. Quantum ground state and single-phonon control of a mechanical resonator. *Nature*, 464:697–703, 2010.
- [4] M. H. Anderson, J. R. Ensher, M. R. Matthews, C. E. Wieman, and E. A. Cornell. Observation of Bose-Einstein condensation in a dilute atomic vapor. *Science*, 269(5221):198–201, 1995.
- [5] S. Gerlich, S. Eibenberger, M. Tomandl, S. Nimmrichter, K. Hornberger, P. J. Fagan, J. Tüxen, M. Mayor, and M. Arndt. Quantum interference of large organic molecules. *Nature Communications*, 2, 2011.
- [6] L. de Broglie. Waves and quanta. *Nature*, 112, 1923.
- [7] C. Davisson and L. H. Germer. Diffraction of electrons by a crystal of nickel. *Phys. Rev.*, 30:705–740, Dec 1927.
- [8] G.P. Thomson and A. Reid. Diffraction of cathode rays by a thin film. *Nature*, 119, 1927.
- [9] I. Estermann and O. Stern. Beugung von Molekularstrahlen. *Z. Phys.*, 61:95–125, 1930.
- [10] E. Fermi and L. Marshall. Interference phenomena of slow neutrons. *Phys. Rev.*, 71:666–677, 1947.
- [11] H. Rauch, W. Treimer, and U. Bonse. Test of a single crystal neutron interferometer. *Physics Letters A*, 47:369–371, 1974.

REFERENCES

- [12] J. A. Leavitt and F. A. Bills. Single-slit diffraction pattern of a thermal atomic potassium beam. *American Journal of Physics*, 37(9):905–912, 1969.
- [13] D. W. Keith, M. L. Schattenburg, Henry I. Smith, and D. E. Pritchard. Diffraction of atoms by a transmission grating. *Phys. Rev. Lett.*, 61:1580–1583, 1988.
- [14] M. Arndt, O. Nairz, J. Vos-Andreae, C. Keller, G. van der Zouw, and A. Zeilinger. Wave-particle duality of C₆₀ molecules. *Nature*, 401:680–682, 1999.
- [15] B. Brezger, L. Hackermüller, S. Uttenthaler, J. Petschinka, M. Arndt, and A. Zeilinger. Matter-wave interferometer for large molecules. *Phys. Rev. Lett.*, 88:100404, 2002.
- [16] S. Gerlich, L. Hackermüller, K. Hornberger, A. Stibor, H. Ulbricht, M. Gring, F. Goldfarb, T. Savas, M. Müri, M. Mayor, and M. Arndt. A Kapitza–Dirac–Talbot–Lau interferometer for highly polarizable molecules. *Nature Physics*, 3:711–715, 2007.
- [17] H. F. Talbot. Facts relating to optical science. *Philos. Mag.*, 9(401), 1836.
- [18] A.W. Lohmann and D.E. Silva. An interferometer based on the Talbot effects. *Optics Communications*, 2(9):413 – 415, 1971.
- [19] A.W. Lohmann and D.E. Silva. A Talbot interferometer with circular gratings. *Optics Communications*, 4(5):326 – 328, 1972.
- [20] E. Lau. Beugungserscheinungen an Doppelrastern. *Annalen der Physik*, 437(7-8):417–423, 1948.
- [21] B. E. A. Saleh and M. C. Teich. *Fundamentals of Photonics*. Wiley Series in Pure and Applied Optics, 2007.

-
- [22] M. S. Chapman, C. R. Ekstrom, T. D. Hammond, R. A. Rubenstein, J. Schmiedmayer, S. Wehinger, and D. E. Pritchard. Optics and interferometry with Na₂ molecules. *Phys. Rev. Lett.*, 74:4783–4786, 1995.
- [23] M. Marksteiner, P. Haslinger, H. Ulbricht, M. Sclafani, H. Oberhofer, C. Dellago, and M. Arndt. Gas-phase formation of large neutral alkaline-earth metal tryptophan complexes. *Journal of the American Society for Mass Spectrometry*, 19:1021 – 1026, 2008.
- [24] M. Marksteiner, P. Haslinger, M. Sclafani, H. Ulbricht, and M. Arndt. UV and VUV ionization of organic molecules, clusters, and complexes. *The Journal of Physical Chemistry A*, 113:9952–9957, 2009.
- [25] J. F. Clauser and S. Li. “Heisenberg microscope” decoherence atom interferometry. *Phys. Rev. A*, 50:2430–2433, 1994.
- [26] L. Hackermüller, S. Uttenthaler, K. Hornberger, E. Reiger, B. Brezger, A. Zeilinger, and M. Arndt. Wave nature of biomolecules and fluorofullerenes. *Phys. Rev. Lett.*, 91(9):090408, 2003.
- [27] P. L. Kapitza and P. A. M. Dirac. The reflection of electrons from standing light waves. *Mathematical Proceedings of the Cambridge Philosophical Society*, 29(02):297–300, 1933.
- [28] D. L. Freimund, K. Aflatooni, and H. Batelaan. Observation of the Kapitza-Dirac effects. *Nature*, 413:142–143, 2001.
- [29] P. H. Bucksbaum, D. W. Schumacher, and M. Bashkansky. High-intensity Kapitza-Dirac effect. *Phys. Rev. Lett.*, 61:1182–1185, 1988.
- [30] S. Altshuler, L. M. Frantz, and R. Braunstein. Reflection of atoms from standing light waves. *Phys. Rev. Lett.*, 17:231–232, 1966.
- [31] P. E. Moskowitz, P. L. Gould, S. R. Atlas, and D. E. Pritchard. Diffraction of an atomic beam by standing-wave radiation. *Phys. Rev. Lett.*, 51(5):370–373, 1983.

REFERENCES

- [32] P. E. Moskowitz, P. L. Gould, and D. E. Pritchard. Deflection of atoms by standing-wave radiation. *J. Opt. Soc. Am. B*, 2:1784–1790, 1985.
- [33] E. M. Rasel, M. K. Oberthaler, H. Batelaan, J. Schmiedmayer, and A. Zeilinger. Atom wave interferometry with diffraction gratings of light. *Phys. Rev. Lett.*, 75:2633–2637, 1995.
- [34] O. Nairz, B. Brezger, M. Arndt, and A. Zeilinger. Diffraction of complex molecules by structures made of light. *Phys. Rev. Lett.*, 87, 2001.
- [35] J. Tuxen, S. Gerlich, S. Eibenberger, M. Arndt, and M. Mayor. Quantum interference distinguishes between constitutional isomers. *Chem. Commun.*, 46:4145–4147, 2010.
- [36] M. Gring, S. Gerlich, S. Eibenberger, S. Nimmrichter, T. Berrada, M. Arndt, H. Ulbricht, K. Hornberger, M. Müri, M. Mayor, M. Böckmann, and N. L. Doltsinis. Influence of conformational molecular dynamics on matter wave interferometry. *Phys. Rev. A*, 81:031604, 2010.
- [37] L. Hackermüller, L. Iler, K. Hornberger, S. Gerlich, M. Gring, H. Ulbricht, and M. Arndt. Optical polarizabilities of large molecules measured in near-field interferometry. *Applied Physics B: Lasers and Optics*, 89:469–473, 2007.
- [38] S. Gerlich, M. Gring, H. Ulbricht, K. Hornberger, J. Tüxen, M. Mayor, and M. Arndt. Matter-wave metrology as a complementary tool for mass spectrometry. *Angewandte Chemie International Edition*, 47:6195–6198, 2008.
- [39] S. B. Cahn, A. Kumarakrishnan, U. Shim, T. Sleator, P. R. Berman, and B. Dubetsky. Time-domain de Broglie wave interferometry. *Phys. Rev. Lett.*, 79:784–787, 1997.
- [40] F. Ruschewitz, J. L. Peng, H. Hinderthür, N. Schaffrath, K. Sengstock, and W. Ertmer. Sub-kilohertz optical spectroscopy with a time domain atom interferometer. *Phys. Rev. Lett.*, 80:3173–3176, 1998.

-
- [41] H. Hinderthür, F. Ruschewitz, H.-J. Lohe, S. Lechte, K. Sengstock, and W. Ertmer. Time-domain high-finesse atom interferometry. *Phys. Rev. A*, 59:2216–2219, 1999.
- [42] A. Turlapov, A. Tonyushkin, and T. Sleator. Talbot-Lau effect for atomic de Broglie waves manipulated with light. *Phys. Rev. A*, 71:043612, 2005.
- [43] W. D. Knight, Walt A. De Heer, Winston A. Saunders, Keith Clemenger, M. Y. Chou, and Marvin L. Cohen. Alkali metal clusters and the jellium model. *Chemical Physics Letters*, 134(1):1 – 5, 1987.
- [44] T. P. Martin, T. Bergmann, H. Ghlich, and T. Lange. Observation of electronic shells and shells of atoms in large na clusters. *Chemical Physics Letters*, 172(3-4):209 – 213, 1990.
- [45] I. Rabin, C. Jackschath, and W. Schulze. Shell effects in singly and multiply charged silver and gold clusters. *Zeitschrift für Physik D Atoms, Molecules and Clusters*, 19:153–155, 1991.
- [46] I. Katakuse, T. Ichihara, Y. Fujita, T. Matsuo, T. Sakurai, and H. Matsuda. Mass distributions of negative cluster ions of copper, silver, and gold. *International Journal of Mass Spectrometry and Ion Processes*, 74(1):33 – 41, 1986.
- [47] D.L. Feldheim and C.A. Foss, editors. *Metal nanoparticles*. Marcel Dekker, Inc., 2002.
- [48] W. D. Knight, Keith Clemenger, Walt A. de Heer, Winston A. Saunders, M. Y. Chou, and Marvin L. Cohen. Electronic shell structure and abundances of sodium clusters. *Phys. Rev. Lett.*, 52:2141–2143, 1984.
- [49] S. Nimmrichter, K. Hornberger, H. Ulbricht, and M. Arndt. Absolute absorption spectroscopy based on molecule interferometry. *Phys. Rev. A*, 78:063607, 2008.
- [50] Walt A. de Heer. The physics of simple metal clusters: experimental aspects and simple models. *Rev. Mod. Phys.*, 65:611–676, Jul 1993.

REFERENCES

- [51] G. Mie. Beitrge zur Optik trüber Medien, speziell kolloidaler Metallösungen. *Annalen der Physik*, 330:377–445, 1908.
- [52] U. Kreibig and M. Vollmer. *Optical properties of metal clusters*. Springer Berlin / Heidelberg, 1995.
- [53] S. Nimmrichter, P. Haslinger, K Hornberger, and M. Arndt. Concept of an ionizing time-domain matter-wave interferometer. *New Journal of Physics*, 13:075002, 2011.
- [54] S. Nimmrichter and K. Hornberger. Theory of near-field matter-wave interference beyond the eikonal approximation. *Phys. Rev. A*, 78:023612, 2008.
- [55] K. Hornberger, J. E. Sipe, and M. Arndt. Theory of decoherence in a matter wave Talbot-Lau interferometer. *Phys. Rev. A*, 70:053608, 2004.
- [56] K. Hornberger, S. Gerlich, H. Ulbricht, L. Hackermüller, S Nimmrichter, I. V. Goldt, O. Boltalina, and M. Arndt. Theory and experimental verification of Kapitza–Dirac–Talbot–Lau interferometry. *New Journal of Physics*, 11(4):043032, 2009.
- [57] Stefan Nimmrichter. Matter wave Talbot-Lau interferometry beyond the eikonal approximation. Master’s thesis, Technische Universität München, 2007.
- [58] R. Schäfer and J. A. Becker. Electronic properties of isolated GaNAsM clusters: photoionization-, photodissociation- and photoluminescence quantum yields. *Zeitschrift für Physik D Atoms, Molecules and Clusters*, 40:490–492, 1997.
- [59] T. Juffmann, S. Truppe, P. Geyer, A. G. Major, S. Deachapunya, H. Ulbricht, and M. Arndt. Wave and particle in molecular interference lithography. *Phys. Rev. Lett.*, 103:263601, 2009.
- [60] H. Haberland, M. Mall, M. Moseler, Y. Qiang, T. Reiners, and Y. Thurner. Filling of micron sized contact holes with copper by

-
- energetic cluster impact. *Journal of Vacuum Science Technology A: Vacuum, Surfaces, and Films*, 12:2925–2930, 1994.
- [61] F. Frank, W. Schulze, B. Tesche, J. Urban, and B. Winter. Formation of metal clusters and molecules by means of the gas aggregation technique and characterisation of size distribution. *Surface Science*, 156(Part 1):90–99, 1985.
- [62] R. Campargue. Progress in overexpanded supersonic jets and skimmed molecular beams in free-jet zones of silence. *The Journal of Physical Chemistry*, 88(20):4466–4474, 1984.
- [63] W. C. Wiley and I. H. McLaren. Time-of-flight mass spectrometer with improved resolution. *Review of Scientific Instruments*, 26:1150–1157, 1955.
- [64] J.A. McClay and A.S.L. McIntyre. 157 nm optical lithography: the accomplishments and the challenges. *Solid State Technology*, 42:57–68, 1999.
- [65] D. Basting and G. Marowsky. *Excimer Laser Technology*. Springer-Verlag, 2005.
- [66] J. Marshall, S.L. Trokel, S. Rothery, and R.R. Krueger. Long-term healing of the central cornea after photorefractive keratectomy using an excimer laser. *Ophthalmology*, 95(10), 1988.
- [67] S.M.Hooker and C.E. Webb. Progress in vacuum ultraviolet lasers. *Prog. Quant. Electr.*, 18:227–274, 1994.
- [68] M. Kakehata, T. Uematsu, F. Kannari, and M. Obara. Efficiency characterization of vacuum ultraviolet molecular fluorine (F_2) laser (157 nm) excited by an intense electric discharge. *Journal of Quantum Electronics*, 27(2), 1991.
- [69] C.J. Sansonetti, J. Reader, and K. Vogler. Precision measurement of wavelengths emitted by a molecular fluorine laser at 157 nm precision

REFERENCES

- measurement of wavelengths emitted by a molecular fluorine laser at 157 nm. *Applied Optics*, 40(12), 2001.
- [70] G. Soumagne, S. Nagai, N. Hisanaga, S. Nanzai, Y. Ochiishi, A. Ohbu, J. Fujimoto, and H. Mizoguchi. Long-run-time performance characteristics of a line-selected 2-kHz F2laser for optical microlithography. *Proc. SPIE*, 4346:1137–1144, 2001.
- [71] Nadine Dörre. Design and development of an optical matter wave interferometer. Master’s thesis, University of Vienna, 2010.
- [72] R. R. Kunz, V. Liberman, and D. K. Downs. Experimentation and modeling of organic photocontamination on lithographic optics. *Journal of Vacuum Science & Technology B*, 18(3):1306–1313, 2000.
- [73] A. K. Bates, M. Rothschild, T. M. Bloomstein, T. H. Fedynyshyn, R. R. Kunz, V. Liberman, and M. Switkes. Review of technology for 157-nm lithography. *IBM Journal of Research and Development*, 45:605–614, 2001.
- [74] G.W. Bradberry and J.M. Vaughan. Measurement of narrow linewidth with a Fabry–Perot interferometer of limited resolution. *opt. comm.*, 20(2), 1977.
- [75] T. Takakura, K. Iga, and T. Tako. Linewidth measurement of a single longitudinal mode AlGaAs laser with a Fabry-Perot interferometer. *Japanese Journal of Applied Physics*, 19, 1980.
- [76] H. Ludvigsen, M. Tossavainen, and M. Kaivola. Laser linewidth measurements using self-homodyne detection with short delay. *Optics Communications*, 155(1-3):180 – 186, 1998.
- [77] Ex50 datasheet, downloaded from <http://www.gamlaser.com/ex50.htm>; September 6th 2011.
- [78] A. Stibor, K. Hornberger, L. Hackermueller, A. Zeilinger, and M. Arndt. Talbot-Lau interferometry with fullerenes: Sensitivity to inertial forces and vibrational dephasing. *Laser Physics*, 15:10–17, 2005.

-
- [79] Markus K. Oberthaler, Stefan Bernet, Ernst M. Rasel, Jörg Schmiedmayer, and Anton Zeilinger. Inertial sensing with classical atomic beams. *Phys. Rev. A*, 54:3165–3176, Oct 1996.
- [80] Jonas Rodewald. Vibration detection on an all-optical talbot-lau molecular interferometer. University of Vienna, Bachelor’s thesis, 2010.
- [81] Wolfgang Demtröder. *Experimentalphysik 1*. Springer Berlin / Heidelberg, 2006.
- [82] J. M. Doyle, B. Friedrich, J. Kim, and D. Patterson. Buffer-gas loading of atoms and molecules into a magnetic trap. *Phys. Rev. A*, 52:R2515–R2518, 1995.
- [83] D. Egorov, T. Lahaye, W Schöllkopf, B. Friedrich, and J. M. Doyle. Buffer-gas cooling of atomic and molecular beams. *Phys. Rev. A*, 66:043401, 2002.
- [84] D. Patterson, E. Tsikata, and J. M. Doyle. Cooling and collisions of large gas phase molecules. *Phys. Chem. Chem. Phys.*, 12:9736–9741, 2010.
- [85] H. Lu, J. Rasmussen, M. J. Wright, D. Patterson, and J. M. Doyle. A cold and slow molecular beam. *Phys. Chem. Chem. Phys.*, pages –, 2011.
- [86] K. Hornberger, S. Uttenthaler, B. Brezger, L. Hackermüller, M. Arndt, and A. Zeilinger. Collisional decoherence observed in matter wave interferometry. *Phys. Rev. Lett.*, 90:160401, 2003.
- [87] H. P. Saha. *Ab initio* calculation of frequency-dependent atomic dipole polarizability. *Phys. Rev. A*, 47:2865–2870, Apr 1993.
- [88] figure taken from <http://en.wikipedia.org/wiki/anthracene>; september 15th 2011.

REFERENCES

- [89] U. Even, J. Jortner, D. Noy, N. Lavie, and C. Cossart-Magos. Cooling of large molecules below 1 K and He clusters formation. *J. Phys. Chem.*, 112:8068–8071, 2000.
- [90] K. Luria, W. Christen, and U. Even. Generation and propagation of intense supersonic beams. *The Journal of Physical Chemistry A*, 115(25):7362–7367, 2011.
- [91] J. G. Angus and G. C. Morris. Ionization potential of the anthracene molecule from Rydberg absorption bands. *Journal of Molecular Spectroscopy*, 21(1-4):310 – 324, 1966.
- [92] F. Piuzzi, I. Dimicoli, M. Mons, P. Milli, V. Brenner, Q. Zhao, B. Soep, and A. Tramer. Spectroscopy, dynamics and structures of jet formed anthracene clusters. *Chemical Physics*, 275(1-3):123 – 147, 2002.

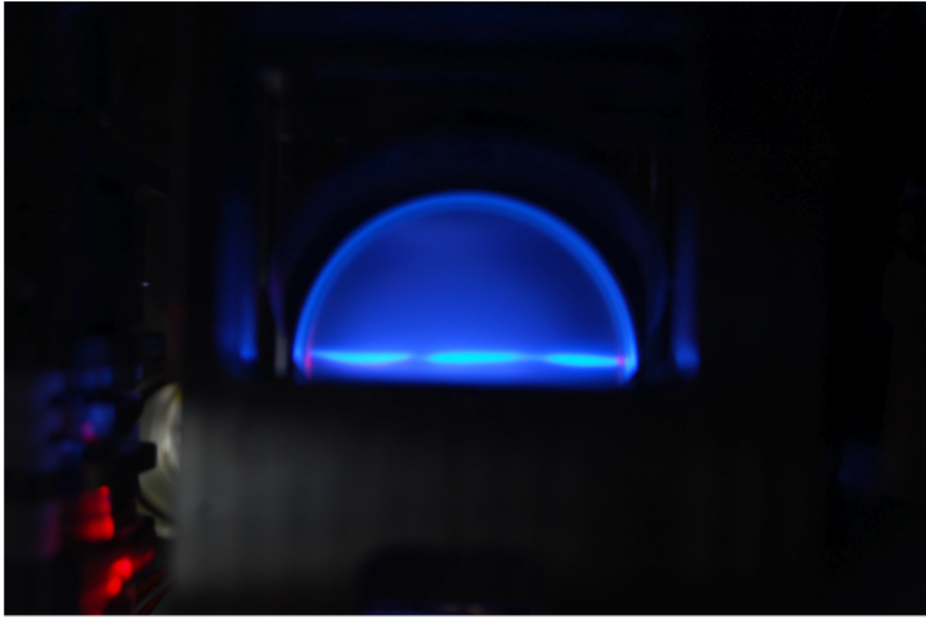


Figure 36: Fluorescent images of the three grating laser spots on the back side of the interferometer mirror. The picture was taken through a window in the main chamber.

8 Acknowledgments

I would like to express my gratitude to Professor Markus Arndt for his support throughout my studies in Vienna and for giving me the opportunity to work on this exciting experiment! Also I would like to thank my friends Nadine Dörre, Philipp Haslinger, Stefan Nimmrichter and Philipp Geyer, who I have enjoyed working with over the past two years and who have always patiently answered my questions and encouraged me while writing this thesis! I am especially grateful to Stefan and Nadine for proofreading this work and making helpful suggestions. And thanks to all the other guys and girls from the Quantumnano group: it has been good times and I'm looking forward to working with you in the years to come!

9 Curriculum Vitae

Personal information

Name	Jonas Hinrich Rodewald
Date of birth	06.05.1987
Place of birth	Freiburg i. Br., Germany
Parents	Dr. Ariane and Prof. Dr. Hans-Reimer Rodewald
Citizenship	German
Languages	German (native), English (fluently), French (colloquially)

Educational history

8/1993 - 7/1997	Theodor Primarschule Basel, Switzerland
8/1997 - 8/1999	Hebel Gymnasium Lörrach, Germany
8/1999 - 6/2006	Humboldt Gymnasium Ulm
6/2006	Abitur, Humboldt Gymnasium Ulm
9/2006 - 9/2010	Studies of physics at the Christian Albrechts University of Kiel
7/2008	Pre-Diploma in physics, University of Kiel
9/2009 - 9/2010	ERASMUS scholarship for physics studies at the University of Vienna, Austria
9/2010	Bachelor thesis in the group of Prof. Dr. Markus Arndt
9/2010	Bachelor of science degree from the University of Vienna
9/2010 -	Master studies of physics at the University of Vienna
9/2011	Master thesis in the group of Prof. Dr. Markus Arndt